COMENIUS UNIVERSITY IN BRATISLAVA

FACULTY OF MATHEMATICS, PHYSICS AND INFORMATICS

In-beam gamma-ray spectroscopy of ^{187}Au at the AFRODITE array

Academic Dissertation

for the Degree of

Doctor of Philosophy

2020

Mgr. Róbert Urban

COMENIUS UNIVERSITY IN BRATISLAVA

FACULTY OF MATHEMATICS, PHYSICS AND INFORMATICS

In-beam gamma-ray spectroscopy of ^{187}Au at the AFRODITE array

Academic Dissertation

for the Degree of

Doctor of Philosophy

Subject:	Nuclear and subnuclear Physics
Branch of study:	4.1.5 Nuclear and subnuclear Physics
Institute:	Institute of Physics, Slovak Academy of Sciences
Department:	Department of Physics
Supervisor:	Mgr. Martin Venhart, PhD.

Bratislava 2020

Mgr. Róbert Urban

Comenius University in Bratislava
Faculty of Mathematics, Physics and Informatics

THESIS ASSIGNMENT

Name and Surname:	Mgr. Róbert Urban
Study programme:	Nuclear and Subnuclear Physics (Single degree study, Ph.D. III. deg., full time form)
Field of Study:	Physics
Type of Thesis:	Dissertation thesis
Language of Thesis:	English
Secondary language:	Slovak

Title: In-beam gamma-ray spectroscopy of 187Au at the AFRODITE array

Annotation: The 187Au isotope is an example of the nucleus that exhibits the shape coexistence. Excited states were populated via 181Ta(12C,6n)187Au reaction and studied by means of the in-beam gamma-ray spectroscopy. The experiment was performed at iThemba LABS (Cape Town, South Africa) and employed the AFRODITE array without channel selector. The goal of the thesis is to search for deformed configurations based on coupling of odd proton with known excited 0+ state in the 188Hg core. Such structures were identified in a comprehensive study of beta decay of 187Hg, performed at the UNISOR facility in 1990's. However, the expected rotational band was not observed yet. Large statistics was produced and the above structures may or may not be populated and observed. Complex data analysis will be needed and both a positive or a negative result will have an impact on the understanding of the structure of odd-Au isotopes.

Tutor:	Mgr. Martin Venhart, PhD.
Department:	FMFI.KJFB - Department of Nuclear Physics and Biophysics
Head of department:	prof. RNDr. Stanislav Tokár, DrSc.
Assigned:	06.08.2014
Approved:	06.08.2014 RNDr. Štefan Olejník, DrSc. Guarantor of Study Programme

.....
Student

.....
Tutor

13096292

Univerzita Komenského v Bratislave
Fakulta matematiky, fyziky a informatiky

ZADANIE ZÁVEREČNEJ PRÁCE

Meno a priezvisko študenta: Mgr. Róbert Urban
Študijný program: jadrová a subjadrová fyzika (Jednoodborové štúdium, doktorandské III. st., denná forma)
Študijný odbor: fyzika
Typ záverečnej práce: dizertačná
Jazyk záverečnej práce: anglický
Sekundárny jazyk: slovenský

Názov: In-beam gamma-ray spectroscopy of 187Au at the AFRODITE array
In-beam gamma spektroskopia izotopu 187Au na detektore AFRODITE

Anotácia: Izotop 187Au je príklad jadra, ktoré vykazuje tvarovú koexistenciu. Excitované stavy boli získané cez 181Ta(12C,6n)187Au reakciu a študované pomocou metodiky in-beam gama spektroskopie. Experiment sa uskutočnil v iThemba LABS (Kapské Mesto, Južná Afrika) použitím sféry AFRODITE, bez selektora kanálov. Cieľom práce je hľadanie deformovaných konfigurácii založených na väzbe nepárneho protónu so známym excitovaným 0+ stavom v jadre 188Hg. Takéto štruktúry boli identifikované v komplexnej štúdii beta rozpadu 187Hg, vykonanej v zariadení UNISOR v 90. rokoch. Napriek tomu, očakávaný rotačný pás ešte nebol pozorovaný. Bola vyprodukovaná vysoká štatistika a spomínané štruktúry môžu, ale nemusia byť populované a pozorované. Bude potrebná komplexná analýza dát a pozitívny či negatívny výsledok bude mať dopad na chápanie štruktúry nepárnych izotopov zlata.

Školiteľ: Mgr. Martin Venhart, PhD.
Katedra: FMFI.KJFB - Katedra jadrovej fyziky a biofyziky
Vedúci katedry: prof. RNDr. Stanislav Tokár, DrSc.

Dátum zadania: 06.08.2014

Dátum schválenia: 06.08.2014

RNDr. Štefan Olejník, DrSc.
garant študijného programu

.....
študent

.....
školiteľ

Declaration of Authorship

I declare that the present work, titled “In-beam gamma-ray spectroscopy of ^{187}Au at the AFRODITE array”, was written by me, using the listed sources.

……..

Acknowledgements

I would like to thank my supervisor, Martin Venhart, for his patience, support and guidance during the process of making this thesis. For his invaluable advice and expertise, that helped me better understand the topic of nuclear structure.

I would also like to thank my colleagues, Matúš Sedlák and Matúš Balogh for their help with ROOT and C++, and Andrej Herzáň for his help with RadWare.

Finally, I would like to thank my family and friends for their support, and my future wife Anička, for always being there for me and never doubting me.

Abstrakt

Experiment PR235 bol uskutočnený v iThemba LABS za účelom študovania izotopu ^{187}Au pomocou in-beam gama spektroskopie. Na meranie gama žiarenia v terčovej pozícii bola použitá sféra detektorov AFRODITE. V experimente bola použitá kombinácia HPGe Clover a LEPS detektorov. Hlavným cieľom bolo študovať jadrovú štruktúru daného izotopu, ktorý vykazuje *tvarovú koexistenciu*. Analýza dát bola vykonaná na Fyzikálnom ústave, použitím vlastne vyvinutého softvéru a pomocou RadWare.

Rozpadová schéma ^{187}Au bola zostrojená z experimentálnych dát, obsahujúc prechody a rotačné pásy súvisiace s konfiguráciami *intruder stavov*. Intenzity prechodov boli získané pomocou RadWare výpočtov. Rozpadové schémy kontaminujúcich izotopov, prítomných v našich dátach, boli taktiež zostrojené.

Nové štruktúry pásov, súvisiace s *intruder stavmi*, ktoré boli predpovedané v PTRM výpočtoch a na základe parabolického trendu v systematike nepárnych izotopov zlata, neboli pozorované. Záverom je, že tieto konfigurácie musia mať odlišné štruktúry, ktoré budú musieť byť pozorované pomocou inej experimentálnej metódy. Naše analyzované dáta nepotvrdzujú nové prechody v ^{187}Au, ktoré boli publikované počas písania tejto práce.

Kľúčové slová: ^{187}Au, gama spektroskopia, jadrová štruktúra, tvarová koexistencia, jadrová deformácia

Abstract

The experiment PR235 was carried out at iThemba LABS to study the ^{187}Au isotope with in-beam gamma-ray spectroscopy. It employed the AFRODITE array for measurement of the outgoing gamma-rays in the target position. A combination of HPGe Clover and LEPS detectors was used in the experiment. The aim was to study nuclear structure of the isotope, known to exhibit *shape coexistence*. Data analysis was performed at the Department of Physics, using our own developed software and RadWare.

The level scheme of ^{187}Au was constructed from the experimental data, containing transitions and rotational bands associated with *intruder state* configurations. Intensities of transitions were obtained from RadWare calculations. Level schemes of contaminating isotopes, present in our data, were also constructed.

New band structures, associated with *intruder states*, that were predicted by PTRM calculations and the parabolic tendency in odd mass gold systematics, were not observed. Concluding that these configurations must have different structures, that have to be observed by a different experimental approach. Our analysed data does not confirm new transitions in ^{187}Au, that were published during the process of writing this work.

Keywords: ^{187}Au, gamma-ray spectroscopy, nuclear structure, shape coexistence, nuclei deformation

Table of Contents

List of Figures

List of Tables

List of Abbreviations

AFRODITE	AFRican Omnipurpose Detector for Innovative Techniques and Experiments
BGO	Bismuth Germanium Oxide ($Bi_4Ge_3O_{12}$)
DAQ	Data Acquisition System
DCO	Directional Correlation form Oriented states
DGF	Digital Gamma Finder
FWHM	Full Width at Half Maximum
HI	Heavy Ion
HPGe	High Purity Germanium
LEPS	Low Energy Photon Spectrometer
MIDAS	Multi Instance Data Acquisition System
mp-nh	many-particle many-hole
P/T	Peak-to-Total ratio
PTRM	Particle plus Triaxial Rotor Model
RDT	Recoil Decay Tagging
SPC	Solid-Pole injector Cyclotron
SRIM	The Stopping and Range of Ions in Matter
SSC	Separated-Sector-Cyclotron

Introduction

Experimental studies of nuclear structure in exotic isotopes continue to play an important role in today's nuclear physics. One of the key questions in basic research of nuclear structure is the mechanism behind nuclear deformation. Contrary to the general perception that the atomic nucleus is a sphere, most nuclei are deformed and therefore display different types of shapes. Despite the fact that nuclear deformation was discovered by Bohr, Mottelson and Rainwater in 1953 [1], the underlying physics mechanism remains unclear to this day. For greater insight into the problematics of nuclear deformation, experimental data need to be obtained by systematic studies of suitable nuclei. Odd mass nuclei can give us information on both single particle and collective states in nuclei, such as deformation (axial, triaxial) and rotation, because of the presence of the odd. Neutron deficient odd mass Au isotopes are known to exhibit the *shape coexistence* phenomenon [2], where one nucleus has states with different deformations. Two types of excitations leading up to those states are known to be present in odd mass Au isotopes at low excitation energy [3]. Proton holes that couple to even-even Hg core and proton particles that couple to even-even Pt core, resulting in distinct groups of states. The proton-particle states are known as *intruder states*, since they intrude across the 82 closed shell. Their energies are dictated not only by single particle energies, but also by massive correlation energies resulting from changing of the shell occupancies. Both Hg and Pt even-even cores are known to have coexisting 0^+ states at low excitation energies, therefore at least four different types of configurations can be. Indeed, such configurations were observed in the ^{187}Hg → ^{187}Au beta-decay study [4], performed at the UNISOR facility in Oak Ridge National Laboratory (Tennessee, United States). Both gamma-rays and conversion electrons were simultaneously detected. Pairs of $11/2^-$ and $3/2^+$ states, connected with E0 transitions (model-independent fingerprints of the shape coexistence) were observed. However, rotational bands, expected to be built on these configurations were never observed in previous studies of ^{187}Au [4 - 7].

The subject of the present work is the study of the odd mass isotope ^{187}Au, aimed to expand the existing level scheme and observe the expected rotational bands connected to the previously established *intruder states*. For this purpose, the experiment PR235 was performed at iThemba LABS facility (Cape Town, South Africa), which employed the AFORDITE array for in-beam gamma-ray spectroscopy of ^{187}Au. The

data analysis was carried out at the Slovak Academy of Sciences, using our own developed software and the RadWare software package [8, 9] for construction of the level scheme of the isotope. Complications surfaced in the data analysis as contaminations from other isotopes have been observed. From then on, these contaminations played a significant role in the analysis, having an effect on the final results. Level schemes of the identified contaminations have also been constructed. Band structures associated with the *intruder state* configurations were not observed, meaning that they have a different structure for the ^{187}Au isotope. The data from the experiment was compared with a new study of ^{187}Au that came out during the analysis.

1 Nuclear structure

1.1 Nuclear models

The nucleus is a many-body quantum system formed by individual particles called nucleons (protons and neutrons). The nucleons are bound together inside of a nucleus by attractive short-ranged forces, which are the result of the strong interaction. The study of nuclear structure is therefore aimed at the understanding of the mechanism and the behaviour of these forces. The limitations in exact calculations of many-body quantum systems are one of the main reasons why a unified theory of the nucleus presently does not exist. As a result of this, devices called nuclear models are used instead. Nuclear models are simplifications of the sought nuclear theory. Based on experimentally observed properties in nuclei and analogies with phenomena described in other fields of physics (e.g. spin-orbit coupling in atomic physics), nuclear models helped to predict physical properties of the nuclei. Many such constructed models exist, with each focusing on different properties of nuclei. A brief introduction to the most important nuclear models regarding nuclear deformation is given below.

1.1.1 The liquid-drop model

A collective model originating from the analogy with a drop of liquid, namely the saturation of the nuclear force. In a drop of liquid, the mass is distributed uniformly and the average distance between two molecules is about equal to the value where the potential interaction energy is at a minimum [10]. The same approach in a nucleus implies that nucleons are also scattered uniformly in a distance where the nuclear force is at its minimum (≈ 0.7 fm [10]). The Liquid-drop model intended to interpret and understand the behaviour of the nuclear binding energy per nucleon curve (see Fig 1.1), which was already known from experimental observation. The curve exhibits two main patterns in binding energy. An increasing tendency from the lightest nuclei up to approximately the nucleon number of 60 (^{62}Ni has the highest mean binding energy), and then a decreasing of the binding energies in the heavier nuclei [11].

The liquid-drop model was successful in describing and approximately quantifying the binding energy *B* of nuclei with the semi-empirical mass formula, first formulated by Weizsäcker in 1935 [12], therefore also called the Weizsäcker formula:

$$B\,(A,Z) = a_V A - a_S A^{2/3} - a_C Z(Z-1)A^{-1/3} - a_A \frac{(A-2Z)^2}{A} \pm \delta \quad (1.1)$$

The first term is the volume term, which is proportional to the volume of the nucleus. The volume of a sphere (the approximated shape of the nucleus) is proportional to R^3, where *R* is the radius of the nucleus. With the radius *R* being proportional to $A^{1/3}$, the resulting volume term is proportional to the number of nucleons *A*. It represents the saturation of the nuclear force in a given volume [10]. The second term is the surface term, which is proportional to the surface of the nucleus. Nucleons closer to the surface will have lower binding energies. The surface of a sphere is proportional to R^2, the resulting surface term is proportional to $A^{2/3}$. The third term is the coulomb term, which expresses the coulomb repulsion between protons, it is proportional to $Z\cdot(Z-1)\cdot R^{-1}$. The first three terms (volume, surface and coulomb) derive from collective properties resulting from the approximation with a charged liquid drop, while the remaining two (asymmetry and pairing) represent more the properties of individual nucleons. The fourth term is the asymmetry term, which derives from the Pauli exclusion principle. The most stable distribution of protons and neutrons in the nucleus for the asymmetry term of the mass formula is $Z = N = A/2$, meaning all the lowest possible orbitals are occupied. In nuclei where $Z \neq N$, the energy needed to lift nucleons to higher orbitals must be taken into consideration. This is expressed as the average energy between two adjacent orbitals, which is proportional to A^{-1} [10]. Therefore, the concluding asymmetry term is proportional to $(A - 2\cdot Z)^2\cdot A^{-1}$. The fifth term is the pairing term, which represents the effect of the spin-coupling of the nucleons. The pairing term has three values, $+\delta$ for doubly even nuclei, *0* for even odd (or vice versa) nuclei and $-\delta$ for doubly odd nuclei.

The last two terms in the Weizsäcker formula are not derived from the liquid-drop model but originate in a single particle approach rather than a collective one. Besides the binding energy, the liquid-drop model helped to describe other phenomena like heavy nuclei fission and alpha decay. However, it fails to describe other observed nuclear phenomena, mainly the existence of Z and N configurations that lead to higher

binding energies and therefore to extra stabilities in nuclei, the existence of magic numbers (Z or N = 2, 8, 20, 28, 50, 82 and 126).

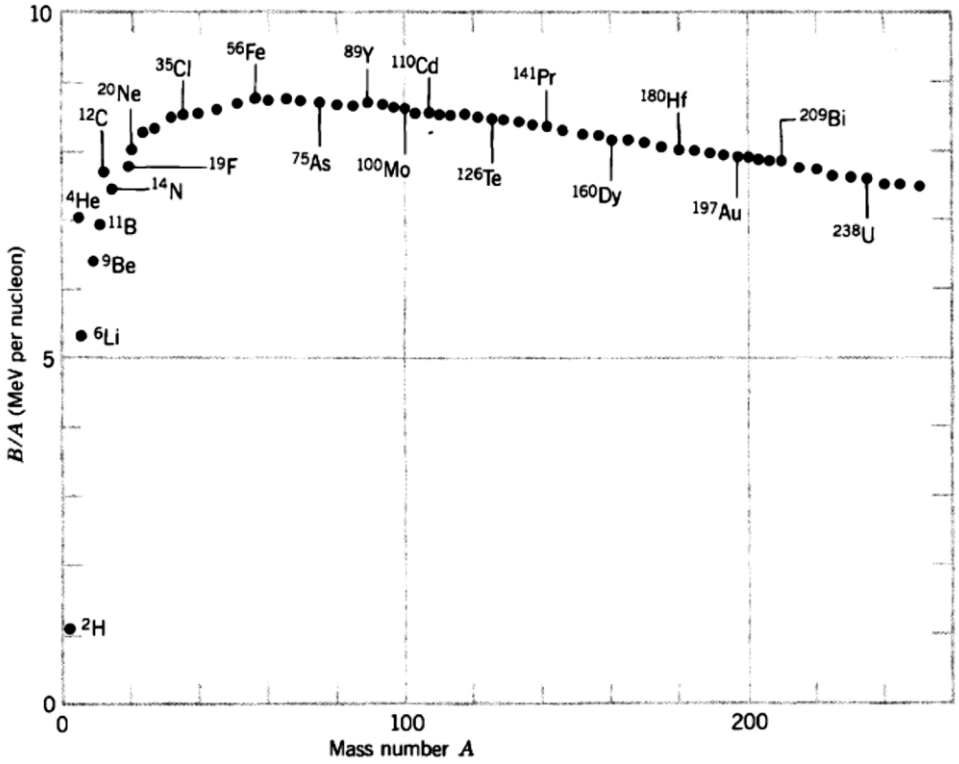

Figure 1.1: Binding energy per nucleon as a function of the Mass (nucleon) number A, taken from [13].

1.1.2 The nuclear shell model

Many experimental observations suggested that a shell structure must exist in nuclei, with the shells closing at the indicated magic numbers. Most commonly, it is the difference in the experimentally measured binding energies and calculations using the Weizsäcker formula, where magic number configurations have higher binding energies. This leads directly to a higher abundance of these nuclei in the environment. Energies of the first excited states are also considerably higher in magic nuclei.

Atomic ionizing potential as a function of the proton number shows similar behaviour around certain electron configurations. This phenomenon was successfully explained with the introduction of electron shells. The analogy with the ionizing potential in chemistry indicates the existence of a shell structure in nuclei. Nuclei with magic numbers have showed higher separation energies for protons and neutrons. For most nuclei, the separation energy is $S_p \approx S_n \approx 8$ MeV, while at magic nuclei, the values

reach their maximum. The nuclear shell model was developed by Mayer [14] and independently by Haxel, Jensen and Suess [15] based on these experimental observations.

In the nuclear shell model, the collective approach from the liquid drop model is replaced by an independent-particle approach. Nucleons act as independent particles whose motion is governed by a central potential *V(r)*, which is generated by all the other remaining nucleons (via two-body nucleon interactions). The simplest approximation used to describe this generated central potential is by using a spherically symmetric potential like the finite square well (1.2) or the harmonic oscillator potential (1.3):

$$V(r) = \begin{cases} -V_0 & if\ r < R \\ 0 & if\ r > R \end{cases} \tag{1.2}$$

$$V(r) = \begin{cases} -V_0\left[1 - \dfrac{r^2}{R^2}\right] & if\ r < R \\ 0 & if\ r > R \end{cases} \tag{1.3}$$

A more realistic potential that is often used is the Woods-Saxon potential:

$$V(r) = \frac{-V_0}{1 + e^{\left(\frac{r-R}{a}\right)}} \tag{1.4}$$

where *R* is the nuclear radius and *a* is the surface thickness. Calculations using the harmonic oscillator or Woods-Saxon potential gave results of closed shells which correspond to the first three magic numbers *2*, *8* and *20*. There were however deviations from higher observed magic numbers. The key to a successful formulation of closed shells was the addition of a strong spin-orbit coupling to the potential, which was suggested by Mayer and by Haxel, Jensen and Suess [14, 15]. Similarly, the idea originated from the analogy with atomic physics, where spin-orbit coupling was also introduced in atomic shell electrons.

Spin-orbit coupling is the interaction between the motion of the particle in a potential and the spin of the particle. In the shell model, the spin-orbit interaction introduces the total angular momentum quantum number of the particle $j = l + s$, where l is the orbital quantum number and s is the spin quantum number of the nucleon. The projection of the total angular momentum in the spin-orbit coupling is thus acquired as $m_j = m_l \pm ½$ (the projection of the spin quantum number of a nucleon is either + ½ or - ½). This dependency splits the orbitals of the harmonic oscillator and closed shells with

the correct magic numbers are observed (see Fig. 1.2). In the outcome, the orbital with the higher total angular momentum projection has the lower energy. The higher the orbital quantum number, the bigger the scale of the splitting of the orbitals. This explains the agreement with the lower magic numbers in the harmonic oscillator and Woods-Saxon potential without the spin-orbit coupling.

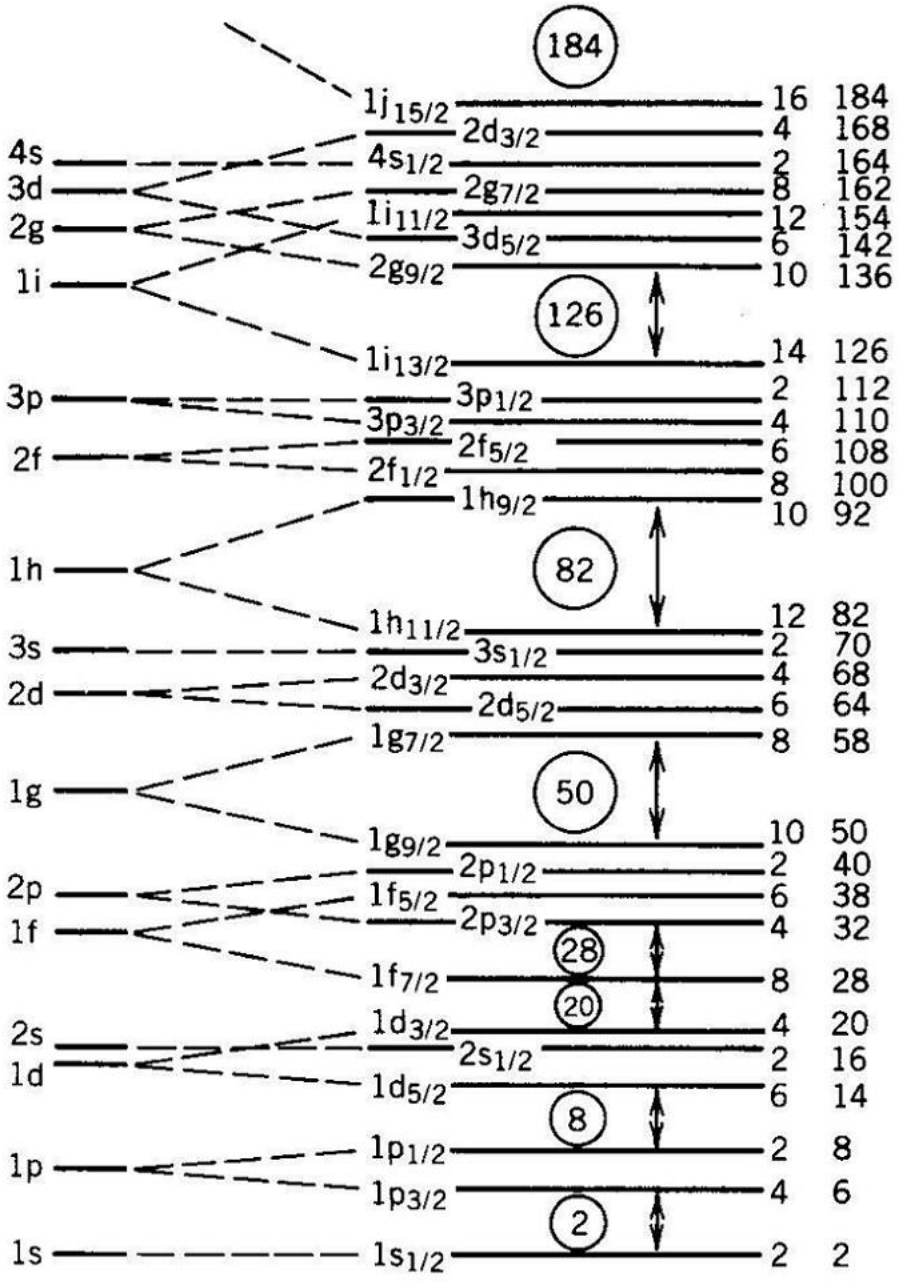

Figure 1.2: Closed shells obtained with the addition of the spin-orbit term to the harmonic oscillator. The splitting of the orbitals is more significant with higher orbital quantum number, taken from [13].

1.1.3 Deformed shell model

The nuclear shell model was successful in the explanation of experimentally observed phenomena connected with proton and neutron magic numbers by applying an isotropic potential in combination with the spin-orbit coupling. The properties of nuclei with doubly-closed shells (nuclei with both proton and neutron magic numbers) plus some extra nucleons were described very well, but far outside these closed shells nuclei have shown large deformations from the spherical shape. These extra nucleons deform the average nucleon potential field by collective mutual polarization [1]. In 1955 S. G. Nilsson used a deformed harmonic oscillator potential to describe the nuclear field which created the deformed shell model – Nilsson model [16].

The graphical representation of the Nilsson model is the *Nilsson Diagram*, where theoretical energy levels of the deformed harmonic oscillator (or any different potential used) are plotted versus ε_2, which is the axially symmetric quadrupole deformation parameter (see equation 1.9). Fig. 1.3 shows an example of the *Nilsson Diagram*. Every orbital in the Nilsson model is described by a set of asymptotic quantum numbers Ω^{π} [N, n_z, Λ] (see Fig. 1.4). The quantum number Ω is the projection of the single-particle angular momentum j on the symmetry axis. $J = j + R$, where J is the total angular momentum of the valence nucleon coupled to the deformed core and R is the angular momentum of the core. π is the parity of the Nilsson orbit, where $\pi = (-1)^N$. N is the quantum number of the oscillator shell, n_z is the number of oscillator quanta along the symmetry axis z and Λ is the projection of the angular momentum of the coupled nucleon on the symmetry axis.

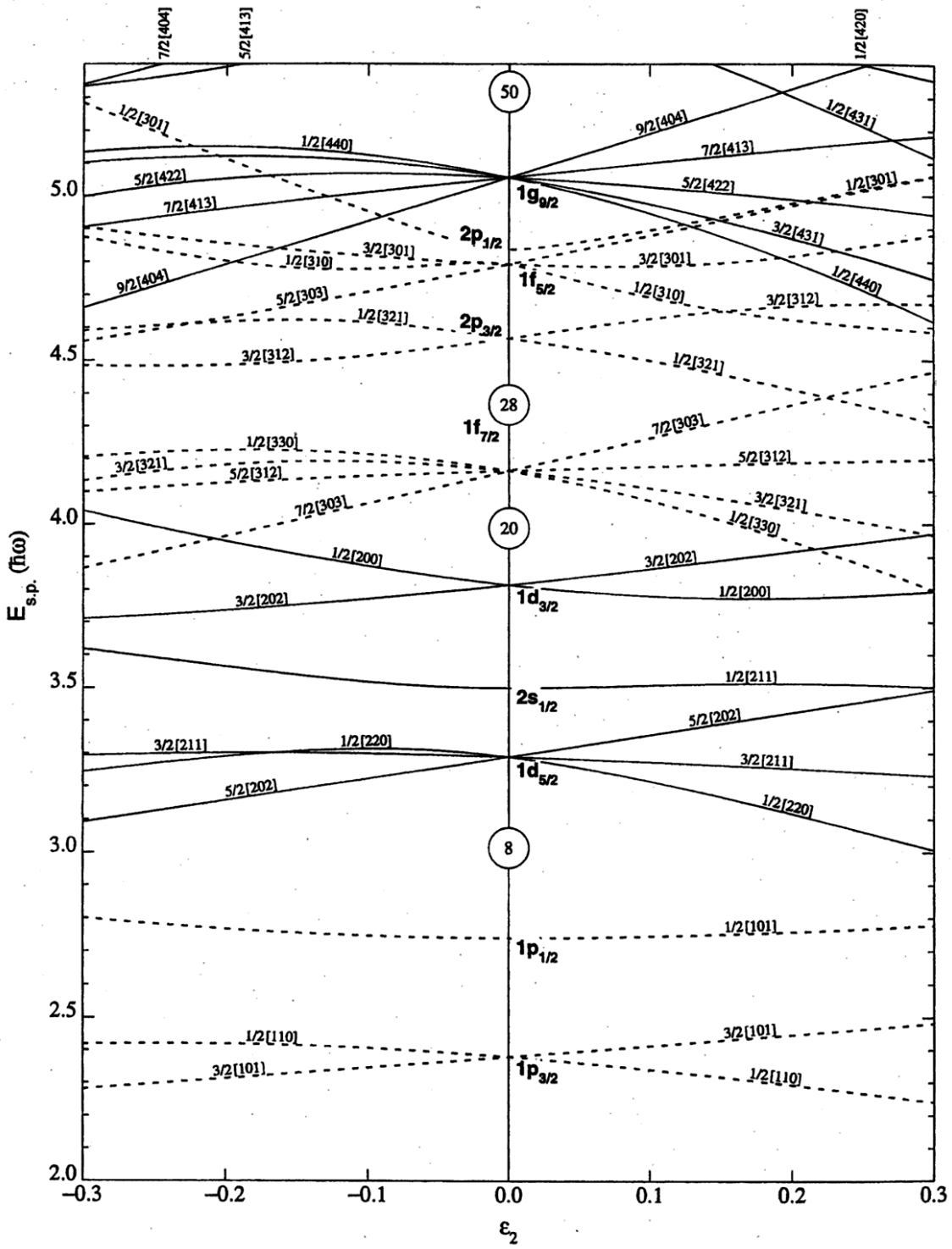

Figure 1.3: Example of a Nilsson diagram. Theoretical energy levels plotted versus the ε_2 parameter, taken from [17].

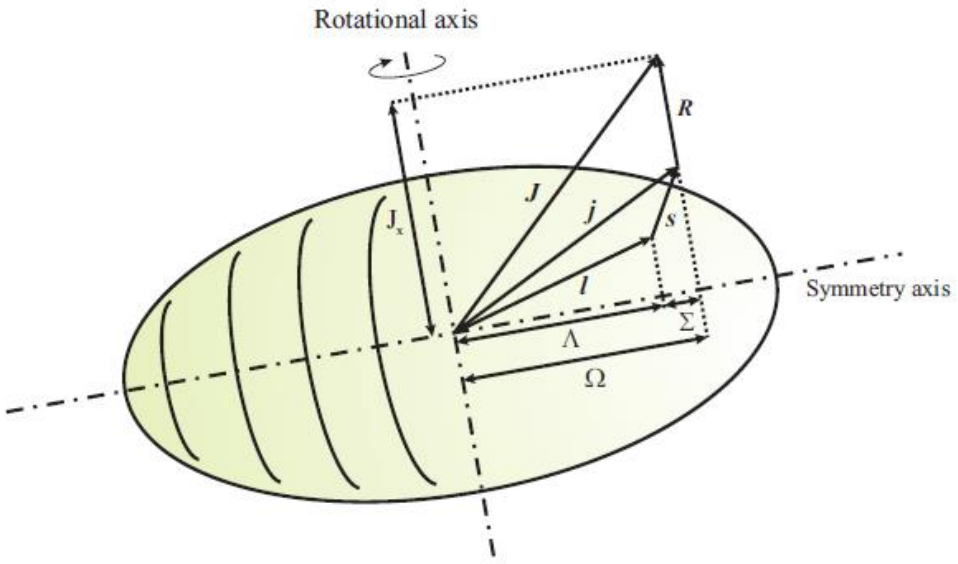

Figure 1.4: Graphical representation of the Nilsson model quantum numbers, taken from [18].

1.2 Nuclear deformation

The general assumption for nuclei is that their shape is a spherical one, but in reality, only few of them are spherical and the majority of the existing nuclei have a deformed shape. The ground states of doubly even nuclei exhibit a spherical shape. The nearer to the closed shells and the subsequent magic numbers, the higher the probability of a spherical shaped nuclei. The radius R of a deformed nucleus is not constant in all directions (x, y and z axes) and can also change in time due to the vibration or rotation. The different shapes of deformed nuclei far outside the closed shells can be described by spherical harmonics as functions of the polar angle θ and the azimuthal angle φ:

$$R(\theta,\varphi) = R_0\left[1 + \sum_{\lambda=0}^{\infty}\sum_{\mu=-\lambda}^{\lambda}\alpha_{\lambda\mu}Y_{\lambda\mu}(\theta,\varphi)\right] \tag{1.5}$$

where R_0 is the radius of a spherical nucleus and $\alpha_{\lambda\mu}$ are amplitudes of spherical harmonics $Y_{\lambda\mu}(\theta,\varphi)$. λ describes the multipolarity of the deformation (λ = 2 for quadrupole deformation, λ = 3 for octupole deformation, λ = 4 for hexadecapole deformation etc.). Dipole deformation (λ = 1) does not occur in nuclei. With the volume conservation law of the nucleus in effect, the nucleus only shifts its centre of mass without a change of the shape. Therefore, it is not considered to be a deformation of the

nucleus. The most common type of deformation in nuclei is the quadrupole deformation. The shape of the deformation is an ellipsoid, which has three conjointly perpendicular semi-axes: *a*, *b* and *c* (see Fig 1.5). The mathematical description of the ellipsoidal surface is:

$$\left(\frac{x}{a}\right)^2 + \left(\frac{y}{b}\right)^2 + \left(\frac{z}{c}\right)^2 = 1 \tag{1.6}$$

where *x*, *y* and *z* are the matching axes for the ellipsoidal semi-axes *a*, *b* and *c*. Case $a = b = c$ is a spherical shape, therefore not a part of the quadrupole deformation. For $a = b \neq c$ (or any other permutation), where two semi-axes are equal, a so called axially symmetric quadrupole deformation occurs. A graphical representation of these cases is shown in Fig. 1.6. For this kind of quadrupole deformation, there are only two possible types of deformed shapes, oblate and prolate spheroids (see Fig 1.7). In the oblate type, the two equal semi-axes are longer than the third axis. For example, $a = b > c$. The opposite case stands for the prolate type. In some nuclei, both types of quadrupole deformation can occur at the same time in a so-called *shape coexistence* (see chapter 1.2.2). For axially symmetric deformations with *z* as the axis of symmetry, only five variables $\alpha_{2\mu}$ are left (for μ = -2, -1, 0, 1, 2) in equation 1.5. Furthermore, only two independent variables (see equations 1.7 and 1.8) are left with the transformation from laboratory into the body-fixed axis system [10]:

$$\alpha_{20} = \beta_2 \cos\gamma \tag{1.7}$$

$$\alpha_{22} = \frac{\sqrt{2}}{2}\beta_2 \sin\gamma \tag{1.8}$$

where β_2 and γ are Hill-Wheeler deformation parameters. β_2 is the quadrupole deformation parameter, positive or negative value represent the prolate and oblate quadrupole deformation (see Fig. 1.7). γ defines the axial symmetry in the deformed nucleus. $\gamma = 0°$, 120° and 240° stands for prolate spheroids and $\gamma = 60°$, 180° and 300° stands for oblate spheroids (see Fig. 1.6). Anything in between those angles results in a triaxial quadrupole deformation, where $a \neq b \neq c$. For axially symmetric quadrupole deformation, the parameter β_2 can be expressed with the quadrupole deformation parameter ε_2 (Nilsson deformation parameter):

$$\beta_2 = \sqrt{\frac{\pi}{5}}\left(\frac{4}{3}\varepsilon_2 + \frac{4}{9}\varepsilon_2^2 + \frac{4}{27}\varepsilon_2^3 + \cdots\right) \tag{1.9}$$

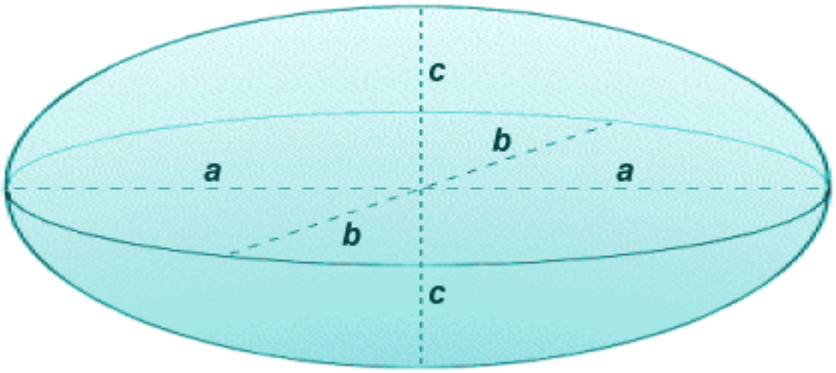

Figure 1.5: Shape and semi-axes of an ellipsoid, taken from [19].

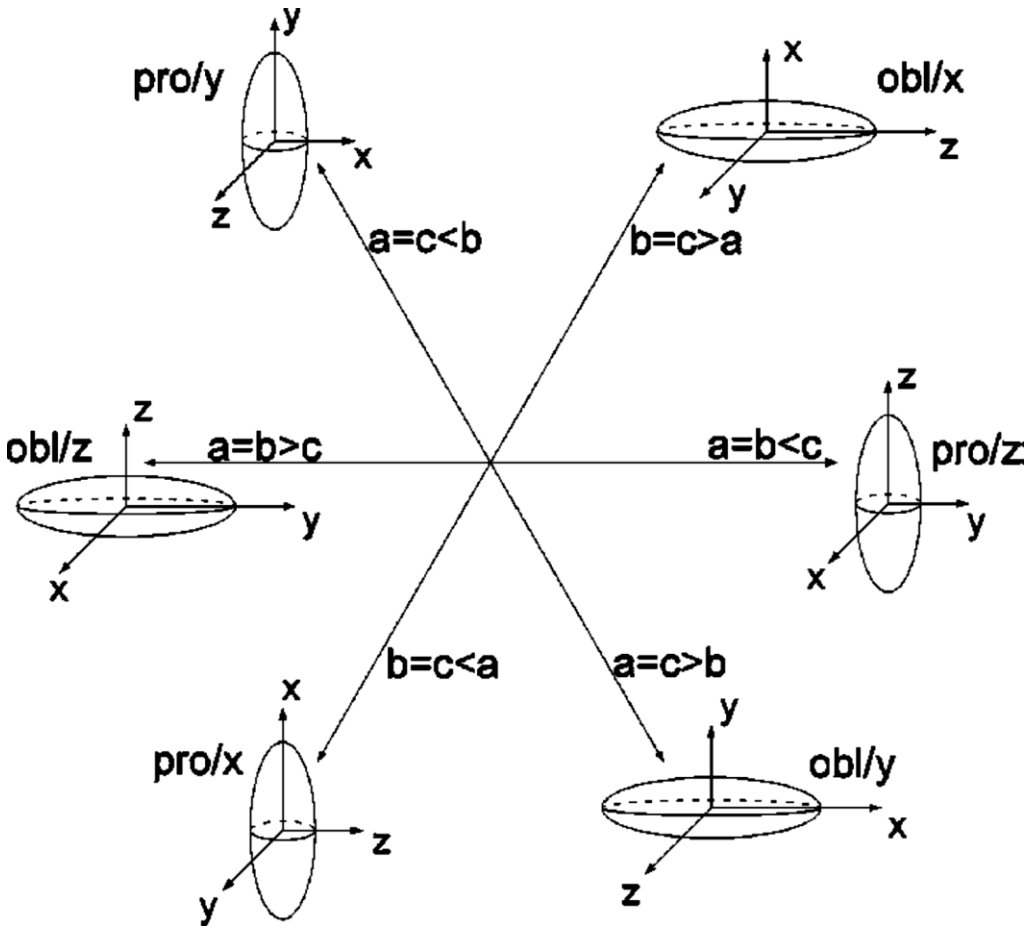

Figure 1.6: Oblate and prolate spheroids obtained in the quadrupole deformation. The centre represents a spherical shape, drawn axes the axially symmetric deformed shapes. In between the axes are triaxial quadrupole deformations. Taken from [20].

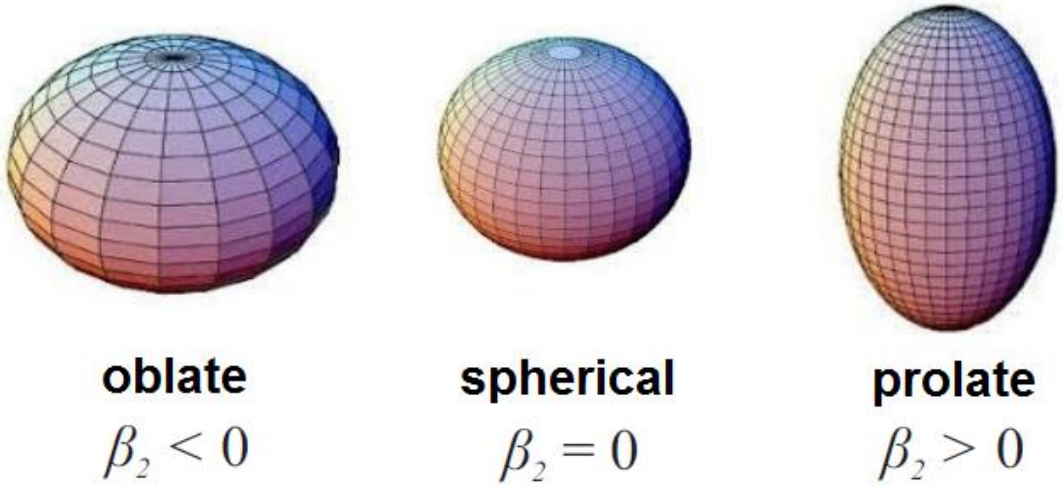

Figure 1.7: Shapes of nuclei with quadrupole deformation.

1.2.1 Rotation and vibration

In the shell model or the deformed shell model, nucleons are viewed as particles occupying the single-particle states in a given potential. Nuclear properties in this approach are determined by a single nucleon or a small volume of valent nucleons. These properties are called single-particle properties. Nuclei also exhibit collective motions of many nucleons at once, properties determined by this motion are called collective properties. Most common examples of collective motions are nuclear vibrations and nuclear rotations.

Equation 1.5 quantifies the shape deformation of the nuclei surface. For very small deformation, the sizes of the amplitudes $\alpha_{\lambda\mu}$ in time are limited by a restoring force (can be calculated from the liquid drop model), which pushes the nucleus back to the initial shape. These continuing sequences of small deformations on the surface of nuclei are called nuclear vibrations. The order of the vibration is given by the multipolarity λ.

In a deformed object, two sets of reference frames can be recognized, the laboratory frame and the intrinsic frame. Orientation of both frames in respect to each other is given by Euler angles.

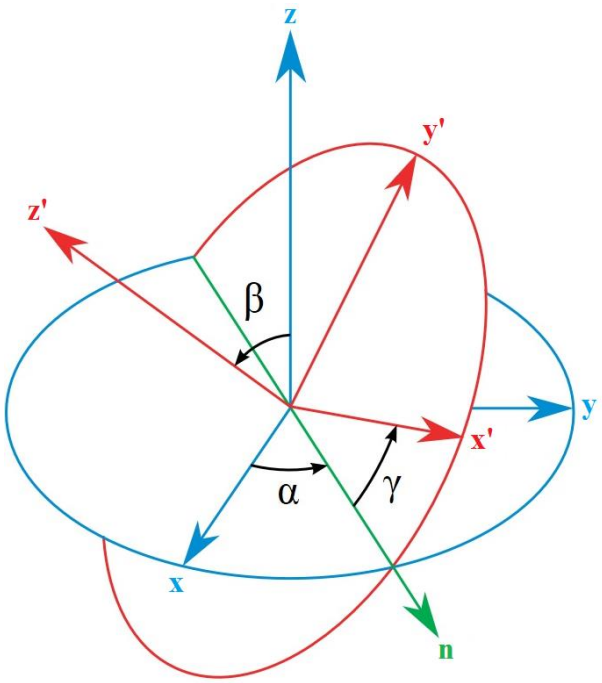

Figure 1.8: Euler angles α, β and γ describing the orientation between the laboratory (red - x', y', z') and intrinsic (blue - x, y, z) frame. n is a line perpendicular to both the z and z' axis.

α - angle between the *x* axis and *n*.

β - angle between the *z* and *z'* axis.

γ - angle between *n* and the *x* axis.

Where *n* is a line perpendicular to both *z* and *z'* axis. *x*, *y* and *z* correspond to the intrinsic frame. *x', y'* and *z'* to the laboratory frame. Because of this, deformed nuclei exhibit a collective motion around an axis called *rotation* and the corresponding axis is the rotational axis. Rotation around the symmetry axis does not change the energy and therefore does not generate excited states, it only changes the phase of the wave function. Excited states originate from the rotation around the rotational axis perpendicular to the symmetry axis. In quantum mechanics, this apparatus is called a quadrupole axial rotor. The quadrupole axial rotor generates excited states with energies:

$$E_{rot} = \frac{\hbar^2}{2\mathcal{J}} J(J+1) \tag{1.10}$$

where $\mathcal{J}$ is the moment of inertia around the rotational axis and *J* is the total angular momentum (see Fig. 1.4). Rotation of the quadrupole axial rotor by 180° around the rotational axis leads to the same state of the rotor, therefore only even *J* are allowed for the excited states.

J	0	2	4	6	8	10
E_{rot}	0	$3\hbar^2/\mathcal{J}$	$10\hbar^2/\mathcal{J}$	$21\hbar^2/\mathcal{J}$	$36\hbar^2/\mathcal{J}$	$55\hbar^2/\mathcal{J}$

Table 1.1: Energies of the excited states for the first six total angular momenta allowed for doubly even nuclei.

This condition applies only to doubly even nuclei, in even odd or odd even nuclei, both the collective motion and the single-particle parameters contribute to the total angular momentum *J*. For an axially symmetric quadrupole deformed shape, the Nilsson quantum number Ω is used to determine the single-particle contribution. The excited states energies are now different:

$$E_{rot} = \frac{\hbar^2}{2\mathcal{J}} J(J+1) - \frac{\hbar^2}{2\mathcal{J}} \Omega(\Omega+1) \qquad (1.11)$$

This approach with a single-particle (quasiparticle) state coupled to an even-even core is described via the particle plus triaxial rotor model (PTRM) [21]. With the contribution of the single-particle, both odd and even total angular momenta are allowed. *Rotational bands*, which are structures of excited states with integrally increasing angular momentum, are constructed upon those single-particle states. The lowest energy state in a rotational band is called the band head. All states in a rotational band have the same parity. The energies of the excited states can be calculated using equation 1.11. For even-even nuclei, where $\Omega = 0$, the equation is reduced to the previous equation 1.10 and the band head state has an angular momentum of *0*. In odd even and even odd nuclei the angular momentum of the band head is determined by Ω. Rotational bands can be constructed on both the ground state of the deformed nucleus or on excited single-particle states. Rotation only occurs in deformed nuclei, therefore in a spherical nucleus, only vibration is possible.

1.2.2 Shape coexistence and intruder states

Rotational bands constructed on low lying excited states correspond to the deformation of the given nucleus. At low excitation energies, the most common is the quadrupole deformation. Excited states from one rotational band are related to either the prolate or oblate deformation. In PTRM, the nucleus is usually constructed from more different single-particle states and even-even cores. This means, that nuclei can have several rotational bands that are constructed on different low energy excited single-particle states. Each of these bands can be associated with a different type of quadrupole deformation in nuclei. This phenomenon is called *shape coexistence*. An example of shape coexistence is the first excited state in the doubly magic nucleus ^{16}O with a spin 0^+ and energy 6.06 MeV (see Fig. 1.9), where the phenomenon was postulated for the first time. The interpretation of this observed state was the rearranging of four particles from occupied orbitals into empty orbitals from the shell above ($1d_{5/2}$, $2s_{1/2}$, $1d_{3/2}$) [22]. This configuration has a strong binding energy and leads to a highly deformed shape that coexists with the spherical ground state of the same spin and parity.

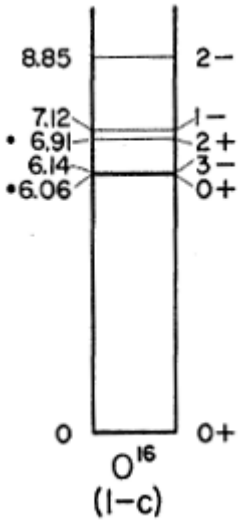

Figure 1.9: Low energy levels in ^{16}O. Dots beside the energies indicate deformed states. The lowest excited state is the intruder state 0^+ with the energy 6.06 MeV. Because of a doubly magic nucleus, the first excited state has a very large energy. Taken from [22].

The doubly magic ^{16}O has eight protons and neutrons, which fully occupy the first the first three nuclear shells in the shell model (see Fig. 1.2). The configuration of the nucleons for the excited 0^+ state consists of three states that are above the closed

shell. Particle states that cross the closed shells are called *intruder states*. They can be expressed as many-particle many-hole (*mp-nh*) proton or neutron excitations, depending on either protons or neutrons that are moving in the shell configuration. Even though the postulation of shape coexistence had its origins in light nuclei, heavier nuclei exhibit this phenomenon more extensive. Mostly the neutron deficient nuclei near the closed 82 proton shell [2]. For example, Pb nuclei with the magic number Z = 82 have fully occupied orbitals for protons. Expressed via *mp-nh*, the ground state for these nuclei is *0p-0h*, that means no hole states are below the closed shell and no particle states are above the closed shell [23]. The intruder state excitation *2p-2h* has two protons across the closed shell, which denotes two particle states above and two hole states below the closed shell. The next excitation would be *4p-4h*. Intruder state configurations span across many nuclei of one element. Fig. 1.10 shows the systematics of intruder proton configurations in neutron deficient odd mass Au isotopes [24]. As can be seen, sometimes the intruder state configuration can have the lowest energy.

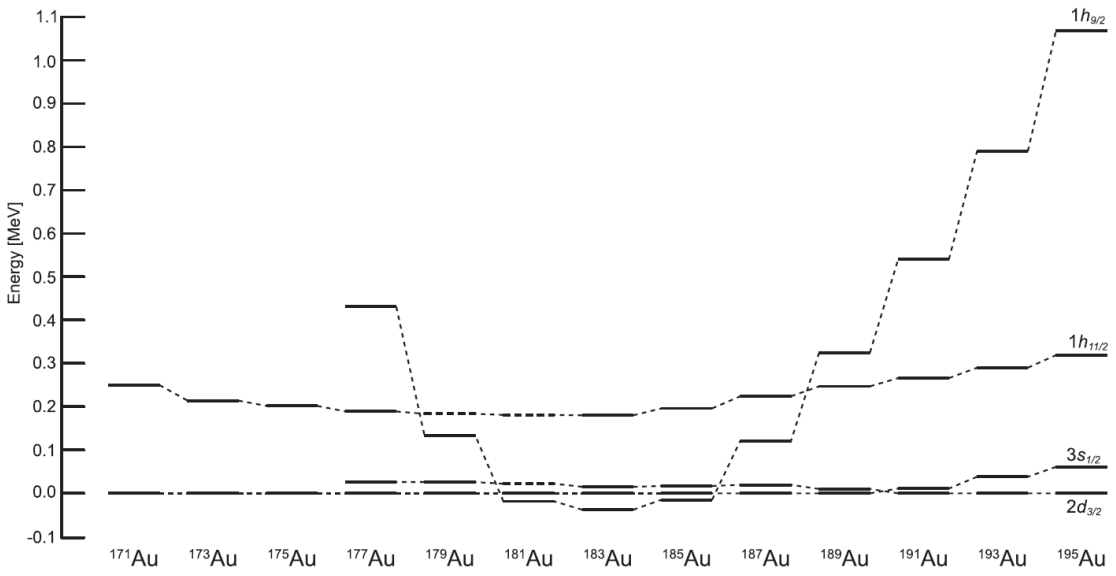

Figure 1.10: Systematics of proton intruder configurations *3s1/2*, *2d3/2*, *1h9/2* and *1h11/2* in neutron deficient odd mass Au isotopes, taken from [24].

Intruder states are frequently associated with shape coexistence. They usually have the same spin and parity as the ground state (for example see Fig 1.9). Transition between such two states occurs via electric monopole (*E0*) transition. If the spin of the nuclear states is *0*, the transition proceeds only via *internal conversion* (the excitation energy of the nucleon is transmitted directly to a bound electron). In the case of an *E0*

transition, the nucleus changes its shape. Evidence shows that *E0* transitions occur widely in association with shape coexistence [25, 26]. *E0* transitions and to some extend intruder configurations found in nuclei can be used as an indication of shape coexistence.

2 Experimental techniques and equipment

2.1 The fusion-evaporation reaction

Nuclear spectroscopy often investigates nuclei which are located at the edge of the nuclei chart and are therefore very unstable. These nuclei are produced in various nuclear reactions. A very common method for production of neutron deficient nuclei is via heavy ion (HI) reactions called fusion-evaporation reactions. In this technique, an ion beam consisting of stable nuclei hits a target that is also made of stable nuclei. The fusion of the two isotopes takes place if the energy of the ion beam is sufficient enough to overcome the repulsive Coulomb barrier that is between them. The barrier height can be expressed as [13]:

$$B_C = \frac{e^2}{4\pi\varepsilon_0}\frac{Z_a Z_X}{R_a + R_X} \tag{2.1}$$

where *R* is the radius, *Z* is the proton number and *a*, *X* stand for projectile and target, respectively. The isotopes of the projectile and the target are specifically chosen to acquire the desired nucleus in the process. Lighter nuclei have lower *N/Z* ratios as heavy nuclei, therefore in the HI fusion-reaction neutron deficient nuclei are commonly produced. This fusion creates a so-called *compound nucleus*, which is unstable and usually highly excited, having high angular momentum and energy (see Fig 2.1). The highly excited (hot) nuclei decay by emitting particles (proton, neutron, α particle etc.) that take away large amounts of energy and very little angular momentum. This evaporation of particles continues until the particle evaporation threshold is reached, then the de-excitation carries on by β decay or by gamma-ray emission. In regions of high density of levels, the decay follows with the emission of statistical gamma-rays (evaporation) until the *Yrast line* is reached. High density of levels means high number of gamma-rays emitted simultaneously, which is only observable as a continuum. The *Yrast line* is the area with the maximum possible angular momentum for a set excitation energy (or the minimum possible excitation energy for a set angular momentum). Near the *Yrast line*, the level density is low (at the line the level density is *0*), which results in the yrast cascade of well-separated gamma-ray transitions [27]. This cascade decays

towards the ground state of the nucleus. The gamma-rays are emitted within 10^{-9} s after the reaction and can be measured only by means of in-beam gamma-ray spectroscopy.

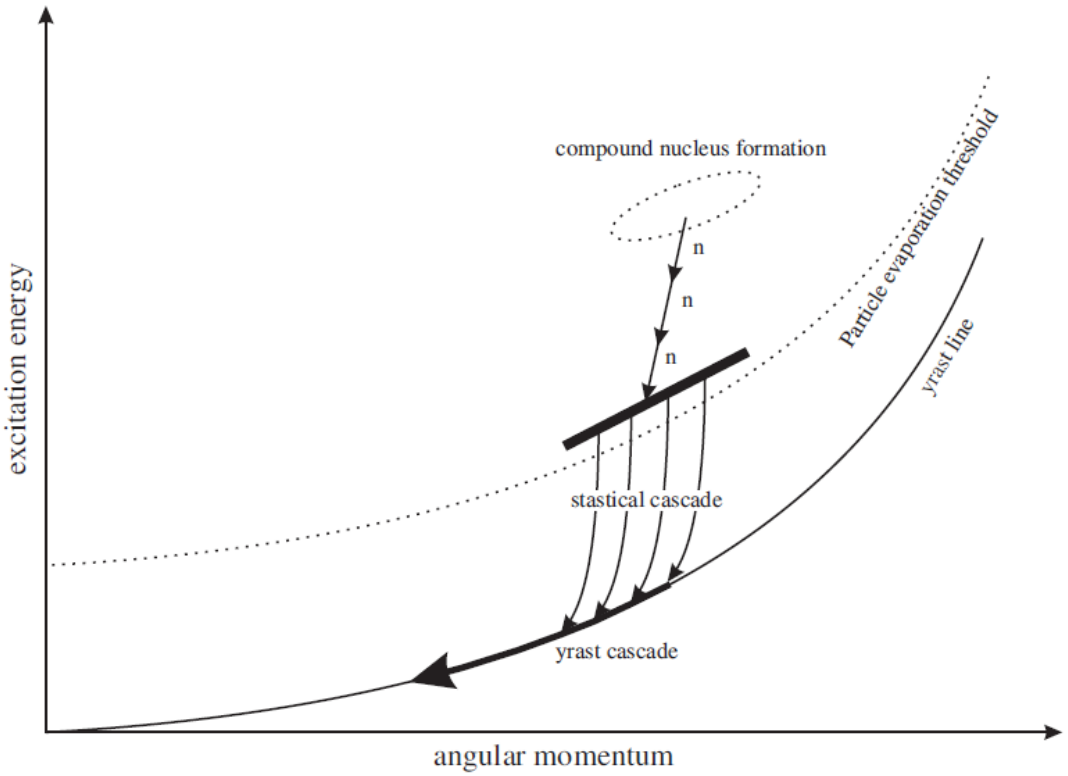

Figure 2.1: Schematic representation of the compound nucleus decay processes, taken from [18].

2.1.1 In-beam Gamma-ray spectroscopy

Studied nuclei produced in HI fusion evaporation reactions are generally measured with In-beam Gamma-ray spectroscopy. It is a method of measuring the emitted gamma-rays directly in the target position. Gamma-rays in these types of experiments have usually a very high multiplicity and their full measurement requires a large number of gamma-ray detectors positioned at different angles. The most advanced are gamma-ray detector arrays which cover up to 4π. A frequent problem with in-beam experiments is the background that arises from the fission of the projectile target fusion product. The recoil decay tagging technique (RDT) is often employed to distinguish gamma-rays from the desired nuclei [28]. The fusion-evaporation residues (recoils) from the reactions are separated behind the target position, usually by electric and magnetic fields, and implanted in a segmented focal plane detector. The charged recoils then proceed to decay via alpha particles, gamma-rays, protons etc. The decay modes

and particle energies are unique to the desired recoiled isotope. Identifying the events from these decay modes provides the opportunity to remove the unwanted in-beam gamma-rays from the output data, in both on-line and off-line analysis. Another problem is the Doppler effect. The gamma emitting fusion-evaporation residues from the target are moving with a fraction of the speed of light in respect to the detectors. This causes a Doppler shift of the measured energy in detectors positioned at certain angles. The Doppler shift in the measured data can be calculated and corrected with the equation:

$$E'_\gamma = E_\gamma \left(1 + \frac{v}{c}\cos\theta\right) \tag{2.2}$$

where E_γ' is the measured (shifted) energy, E_γ is the correct energy of the emitted gamma-ray, v is the velocity of the recoil, c is the speed of light and θ is the angle of the detector position in respect to the beam direction. It is apparent from the equation, that at 90° the Doppler shift does not occur.

2.2 Angular distribution

The compound nucleus created in the HI fusion-evaporation reaction has an angular momentum that is strongly aligned in respect to the beam direction. This alignment originates in the large angular momentum of the projectile ions. As mentioned in chapter 2.1, the decay of this highly excited nucleus lowers the angular momentum only slightly with the majority being taken away by the subsequently emitted yrast cascade gamma-rays. Because of the strong alignment of the compound nucleus, the angular distribution of the emitted gamma-rays exhibits strong anisotropies [29]. This is widely used in nuclear spectroscopy, as measurements of these anisotropies in angular distribution provide information on the multipolarity of the emitted gamma-rays. The angular distribution of emitted gamma-rays is described as [29]:

$$W(\theta) = \frac{I_\gamma(\theta)}{I_\gamma(tot)} = 1 + a_2 P_2(\cos\theta) + a_4 P_4(\cos\theta) \tag{2.3}$$

$$P_2(\cos\theta) = \frac{1}{2}[3\,(\cos\theta)^2 - 1a] \tag{2.4}$$

$$P_4(\cos\theta) = \frac{1}{8}[35\,(\cos\theta)^4 - 30\,(\cos\theta)^2 + 3] \tag{2.5}$$

where $I_\gamma(\theta)$ is the intensity of emitted radiation at angle θ and $I_\gamma(tot)$ is the total intensity. Coefficients a_2 and a_4 are used to determine the linear polarization and the multipole order of the radiation.

2.2.1 Directional correlations from oriented states

Measurements of the angular distribution of gamma-rays show uncertainties when mixed multiple transitions from the source nucleus are emitted [30]. To resolve these uncertainties, measurements of angular correlations are carried out. Two gamma-ray transitions, γ_1 and γ_2, that are in coincidence and emitted in a cascade, are taken. Two detectors at angles θ_1 and θ_2 in respect to the beam direction are at the angle Φ between each other. The intensity of γ_1 detected by the detector at the angle θ_1 in coincidence with γ_2 detected by the detector at the angle θ_2 is given by the angular correlation function $W(\theta_1, \theta_2, \Phi)$ [31]. The opposite case, $W(\theta_2, \theta_1, \Phi)$, is where the intensity of γ_2 is detected at angle θ_1 in coincidence with γ_1 detected at angle θ_2. The ratio of these two correlation functions is used to determine the multipole nature of the detected transitions. This method is known as Directional Correlation form Oriented states (DCO) [31]:

$$R_{DCO} = \frac{W(\theta_1, \theta_2, \Phi)}{W(\theta_2, \theta_1, \Phi)} \tag{2.6}$$

The DCO ratio has an experimental expression, where correlation functions are directly replaced with intensities of gamma-rays gated at the corresponding transitions, divided by the detector efficiency at the corresponding angle [31]:

$$R_{DCO} = \frac{I_{\theta_1}^{\gamma_2}\left(Gate_{\theta_2}^{\gamma_1}\right)}{I_{\theta_2}^{\gamma_2}\left(Gate_{\theta_1}^{\gamma_1}\right)} \tag{2.7}$$

2.2.2 Linear polarization

Polarization measurements are very useful in determining uncertainties during the construction of level schemes of nuclei from acquired experimental data. Unambiguous multipole assignment allows to determine spin and parities of nuclear states. Linear polarization of the detected gamma-rays is the quantity of the direction of their electric field (E). The gamma-ray linear polarization, $P(\theta)$, can be expressed as [32, 33]:

$$P(\theta) = \frac{I_0(\theta, \xi = 0°) - I_{90}(\theta, \xi = 90°)}{I_0(\theta, \xi = 0°) + I_{90}(\theta, \xi = 90°)} \quad (2.8)$$

where $I_0(\theta, \xi)$ is the intensity of the radiation with its electric vector creating a $\xi = 0°$ angle with the plane containing the particle beam (reaction plane) and analogously $I_{90}(\theta, \xi)$ creating a $\xi = 90°$ angle with the reaction plane. The angle θ is the direction of the detector in respect to the beam line.

A device experimentally measuring the linear polarization is called a Compton polarimeter. Basically, it consists of one component used as a scatterer for gamma-rays and at least one component used for the detection of Compton scattered gamma-rays. An ideal polarimeter would contain one scatterer in the centre and four detectors around with a spacing of 90°. All five components in this design lie perpendicularly to the incident gamma-ray [33]. Several different types of detectors were used as Compton polarimeters throughout history. From Geiger counters, scintillators and semiconductor detectors up to HPGe detectors with good energy resolution but lower photopeak efficiency. Large volume crystals are needed to increase photopeak efficiency which on the other hand leads to difficulties with Doppler broadening and worse time characteristics. Clover detectors with segmented crystals address these problems (see chapter 2.3.2). Their most important advantage is a high sensitivity to linear polarization because there is a high probability that a Compton scattered gamma-ray in one crystal will be detected in an adjacent crystal of the same Clover.

Events in a Clover detector can be scattered vertically or horizontally, the scattering anisotropy can be expressed as:

$$A(\theta) = \frac{N_\perp - N_\parallel}{N_\perp + N_\parallel} \quad (2.9)$$

where $N_\perp$ is the number of events scattered horizontally and $N_\parallel$ is the number of events scattered vertically depending on the incident gamma-ray. The scattering anisotropy is proportional to the linear polarization:

$$P(\theta) = \frac{A(\theta)}{Q(E\gamma)} \quad (2.10)$$

where $Q(E_\gamma)$ is the polarization sensitivity of a detector. Linear polarization equations for different types of transitions (M1, E1, etc.) can be expressed with angular

distribution coefficients a_2 and a_4 [34]. For a Clover detector used as a Compton polarimeter, the equations are simplified for the angle $\theta = 90°$:

$$P(90°)^{M1,E1} = \pm \frac{3a_2}{2 - a_2} \tag{2.11}$$

$$P(90°)^{M2,E2} = \pm \frac{12a_2 + 5a_4}{4a_2 - 3a_4 - 8} \tag{2.12}$$

Angular distribution coefficients can be found in [35], Tab. 2.1 shows the signs of the coefficients and linear polarization for the different types of transitions.

Type	a_2	a_4	$P(90°)$
E1	< 0	0	> 0
M1	< 0	0	< 0
E2	> 0	< 0	> 0
M2	> 0	< 0	< 0

Table 2.1: Sings of the a_2, a_4 coefficients and linear polarization $P(\theta)$ for different types of transitions.

2.3 iThemba LABS

Chapters 2.3 - 2.5 are based upon [36 - 38].

The iThemba Laboratory for Accelerator-Based Sciences (LABS) is located in South Africa and consists of two facilities situated in provinces of Gauteng and Western Cape. These facilities provide particle beams used for basic and advanced research, radiotherapy and to produce radioactive isotopes for nuclear medicine. The latter one, located near Cape Town, operates two large accelerators. A 6 MV Van de Graaff accelerator is used mostly for solid state physics. The second one is the K = 200 MeV Separated – Sector – Cyclotron (SSC) accelerator, shown in Fig.2.2. The cyclotron K-value is the kinetic energy for protons that can be reached. Two solid – pole injector cyclotrons (SPC) extend the range of application of the SSC accelerator. The SSC in combination with K = 8 SPC1 delivers proton beams of energies up to 66 MeV and is

used for neutron therapy and production of radioisotopes. The SPC1 pre-accelerates the protons to the energy of 3.14 MeV. The K = 11 SPC2 is used for pre-acceleration of low intensity beams of both light and heavy ions as well as polarized protons. These beams are available during weekends for nuclear research.

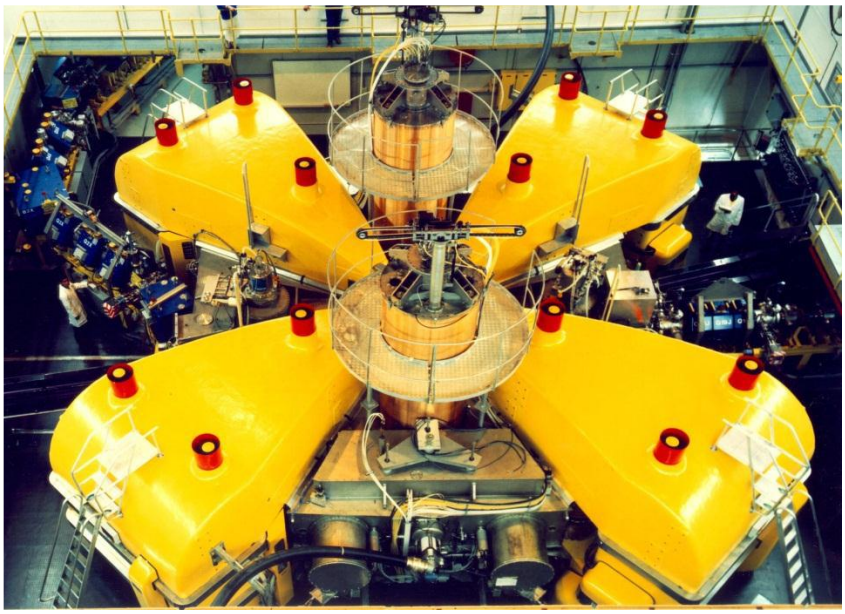

Figure 2.2: Separated – Sector – Cyclotron at iThemba LABS, taken from [39].

2.3.1 The AFRODITE Array

AFRODITE (AFRican Omnipurpose Detector for Innovative Techniques and Experiments) is a 4π gamma-ray detector array at iThemba LABS. It has the ability to detect both high and low energy gamma-rays with satisfactory detection efficiency. This is due to the combination of two types of germanium detectors. HPGe Clover detectors with BGO suppression shields for higher energy photons and segmented HPGe LEPS detectors for low energy photons. The aluminium array frame of AFRODITE has a rhombicuboctahedron shape with a total of 18 openings. Two opposite openings accommodate the beam pipe. One opening perpendicular to the beam pipe is used for the target positioning system, which leaves 15 openings where the detectors can be mounted. There are 3 angle positions in respect to the beam direction, at 45°, 90° and 135° degrees (see Fig 2.3). The target chamber is located at the centre of the array frame (see Fig 2.4). A hydraulically movable target ladder inside the target chamber controls the position of the target [37]. The target ladder usually consists of three slots. The top slot contains the beam position monitor, the middle slot is empty, and the bottom slot

contains the target foil. The distance between the target foil and the front of the detectors is 17 cm [40].

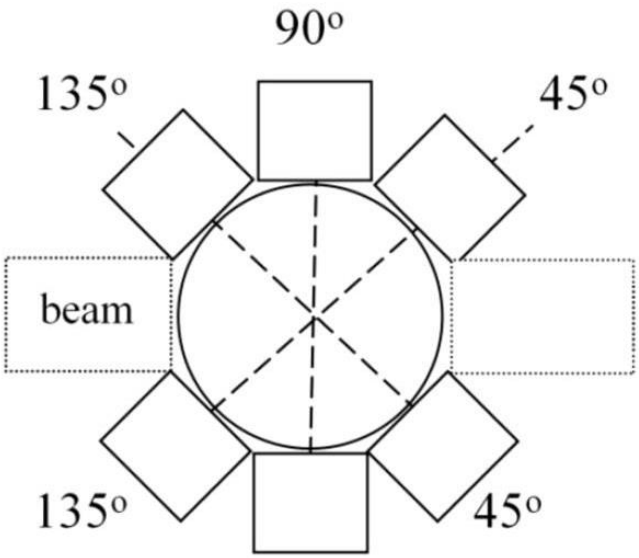

Figure 2.3: Graphical representation of the angle positions of AFRODITE detectors in respect to the beam direction.

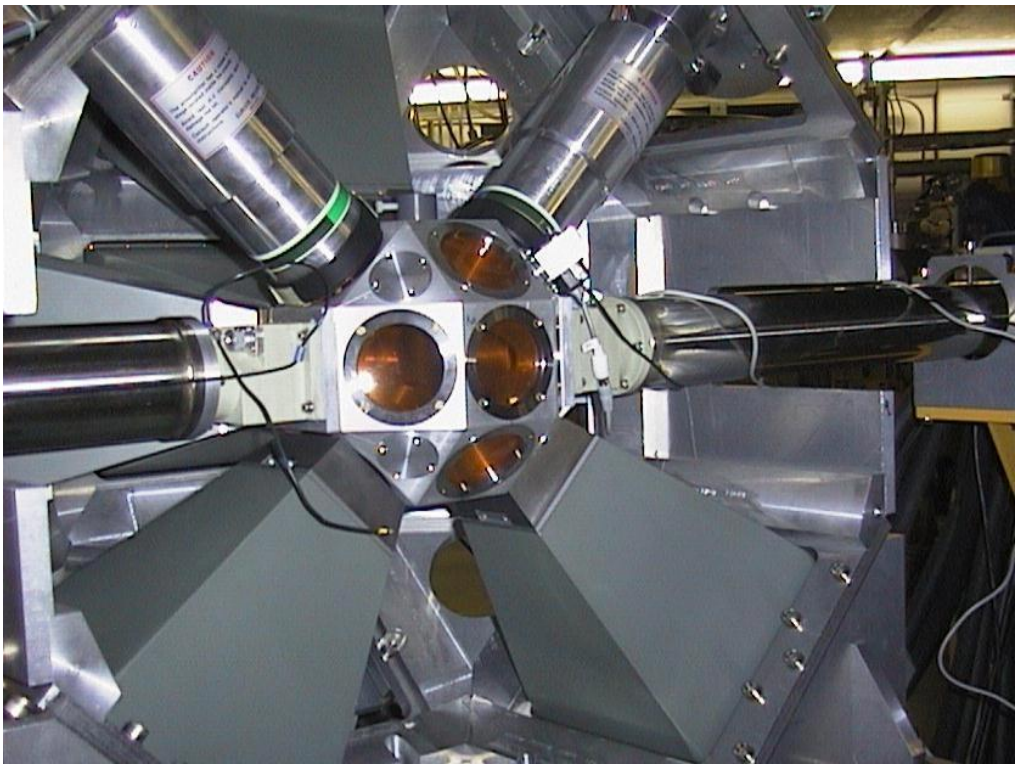

Figure 2.4: Target chamber of the AFRODITE array, taken from [41].

2.3.2 Detectors of the AFRODITE array

Clover detectors contain four separate n-type coaxial HPGe (High Purity Germanium) crystals arranged in a four-leaf Clover, which are placed in one cryostat 0.2 mm apart from one another. Each crystal (called element of Clover detector) has its own preamplifier and acquires signals separately [42]. The energy resolution, represented by FWHM (Full Width at Half Maximum), is about 2.1 keV at 1.33 MeV and 1 keV at 122 keV. The photopeak efficiency for a single crystal is about 21 % measured relative to 7.62 cm x 7.62 cm NaI(Tl) detector positioned 25 cm from the source [42]. The coaxial crystals have 70 mm in length and 50 mm in diameter, one side of the crystal has a tapering which leaves a total volume of around 470 cm^3 for the whole Clover detector [43]. In the AFRODITE array a single Clover detector covers 1.34 % of 4π, which means all the Clovers cover almost 11 % of 4π under normal configurations (8 Clovers). Large volume crystals have a large Doppler broadening effect and worse timing characteristics due to the longer time needed to completely collect the produced electron-hole pairs. The advantage of a Clover detector is the granularity, which decreases these negative effects of large volume detectors. To supress the Compton background in the gamma-ray spectra, each Clover detector is surrounded by a Compton suppression shield made of bismuth germanium oxide $Bi_4Ge_3O_{12}$ (BGO). This scintillator is used for the detection of gamma-rays that escaped from the Clover detector due to Compton scattering. Signals from Clover elements that are in coincidence with the BGO detectors are rejected by the acquisition system. This technique is called Escape-Suppression principle and it increases the Peak-to-total ratio (P/T) from 0.30 to 0.55 for the ^{60}Co 1332 keV transition [44]. In front of the suppression shields are 3 cm thick tungsten collimators with a 35 mm by 35 mm window for the gamma-rays [40]. Fig. 2.5 shows a comparison between unsuppressed and BGO suppressed spectrum measured with a Clover detector.

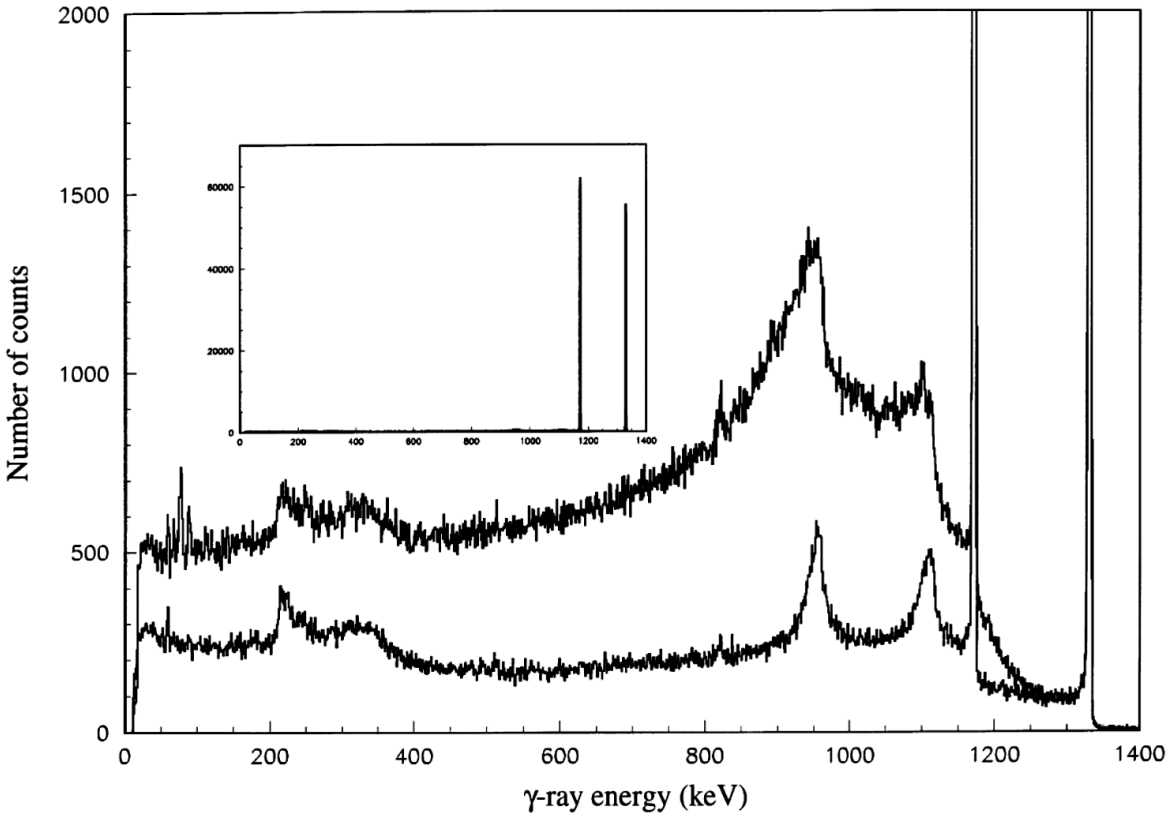

Figure 2.5: Difference between BGO suppressed and unsuppressed spectrum measured with a Clover detector, source ^{60}Co, taken from [44].

Furthermore, the Compton part of the spectrum can be decreased using the *add-back* technique. If during the process of Compton scattering two or more signals of this same event are registered in adjacent Clover crystals, we can later sum up the signals in the offline analysis and thus reconstruct the gamma-ray energy. Coincidence measurements between elements of a Clover detector is used to identify these signals.

LEPS (Low Energy Photon Spectrometer) are detectors made of a single p-type HPGe crystal. The planar detector with 60 mm diameter and 10 mm thickness is electrically segmented into four quadrants. Signals from each quadrant are processed individually, making the LEPS operating similarly as Clover detectors. A single LEPS detector covers 1.57 % of 4π, which means under normal configuration (8 LEPS) all the LEPS cover 12.5 % of 4π. The LEPS detectors are better for detection of low energy gamma-rays as they have high detection efficiency between 30 and 300 keV. The energy resolution varies for different models, for ^{55}Fe (5.9 keV) from 165 to 360 eV and for ^{57}Co (122 keV) from 480 to 585 eV [45].

2.4 Experiment PR235

The experiment PR235 was carried out at iThemba LABS employing the AFRODITE array. The aim of the experiment was the study of shape-coexistence in the odd-mass isotope ^{187}Au. The isotope was produced in two different HI fusion-evaporation reactions using beams delivered by the SSC accelerator.

Au with a proton number 79 is located in the vicinity of the 82 proton closed shell (see Fig 1.2). By means of the PTRM, where an odd quasiparticle is coupled to a triaxial rotating even-even core, odd mass Au isotopes can be expressed by coupling $_{80}$Hg cores with hole states from below the 82 closed proton shell ($s_{1/2}$, $d_{3/2}$, $h_{11/2}$) or by coupling $_{78}$Pt cores with particle states (protons in this case) from beyond the 82 closed proton shell ($h_{9/2}$, $f_{7/2}$, $i_{13/2}$). These particle states that cross the closed shell are called *intruder states*. It was shown that both types of excitations occur in the same isotope resulting in distinct group of states.

Unique parity proton-hole $h_{11/2}$ configurations in ^{187}Au have been experimentally observed in the studies of beta-decay ^{187}Hg $\rightarrow$ ^{187}Au [4, 5]. Particularly a pair of $h_{11/2}$ states connected by a transition with a strong E0 component are of interest (see Fig. 2.6). The interpretation is the coupling of the $h_{11/2}$ proton hole with two coexisting 0^+ states (ground state and one intruder state) in the ^{188}Hg core. The rotational band on the intruder $h_{11/2}$ was not identified. Finding this band is one of the main goals of the experiment PR235.

Positive parity band-heads $1/2^+$ and $3/2^+$ with quasi-rotational bands on them are found in Au isotopes. They correspond to coupling of $s_{1/2}$ and $d_{3/2}$ proton-hole states with even-even Hg cores. Additional positive parity states that decay via transitions with increased E0 components were observed above 500 keV in the beta-decay study of ^{187}Au (see Fig 2.7). Rotational bands above those configurations were not identified. This is possible with in-beam gamma-ray spectroscopy. Observing these rotational bands would determine if these states are strongly deformed intruders. Fig. 2.8 shows the level scheme of ^{187}Au, including rotational bands, constructed from existing in-beam measured in the ^{172}Yb(^{19}F,4n)^{187}Au reaction [6]. The same reaction was used in another in-beam experiment [7] to study the ^{187}Au isotope and a similar level scheme was composed. With the experiment PR235 using recent experimental equipment and possibilities, we intend to identify new rotational bands, expand the existing and if

possible, to assign rotational bands to proton-hole configuration observed in the beta-decay of ^{187}Hg.

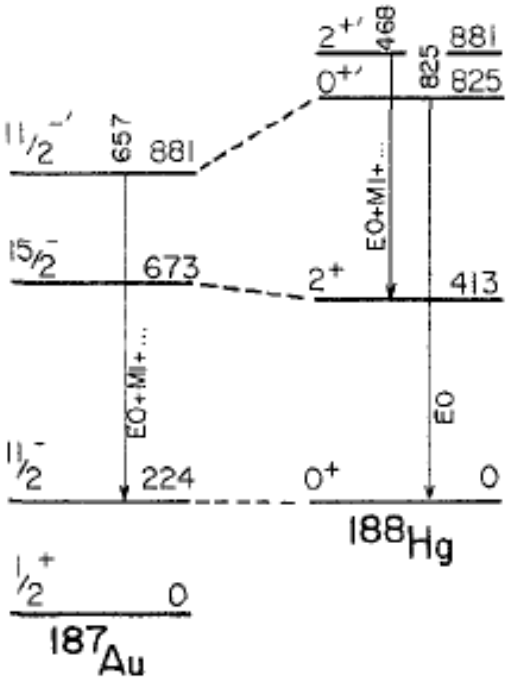

Figure 2.6: Unique parity proton-hole $h_{11/2}$ configurations in ^{187}Au, taken from [5].

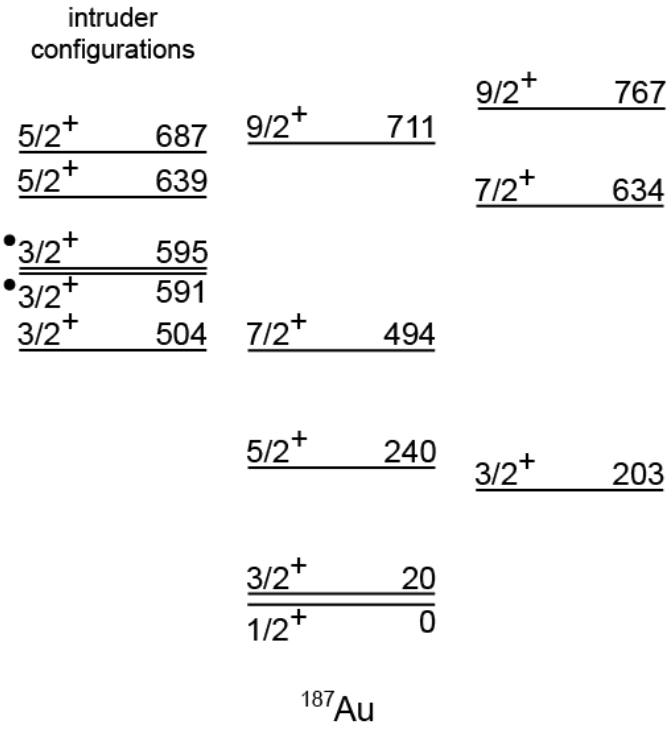

Figure 2.7: Positive parity states connected to the $s_{1/2}$ and $d_{3/2}$ proton-hole states. Circles indicate states that decay via E0 transitions.

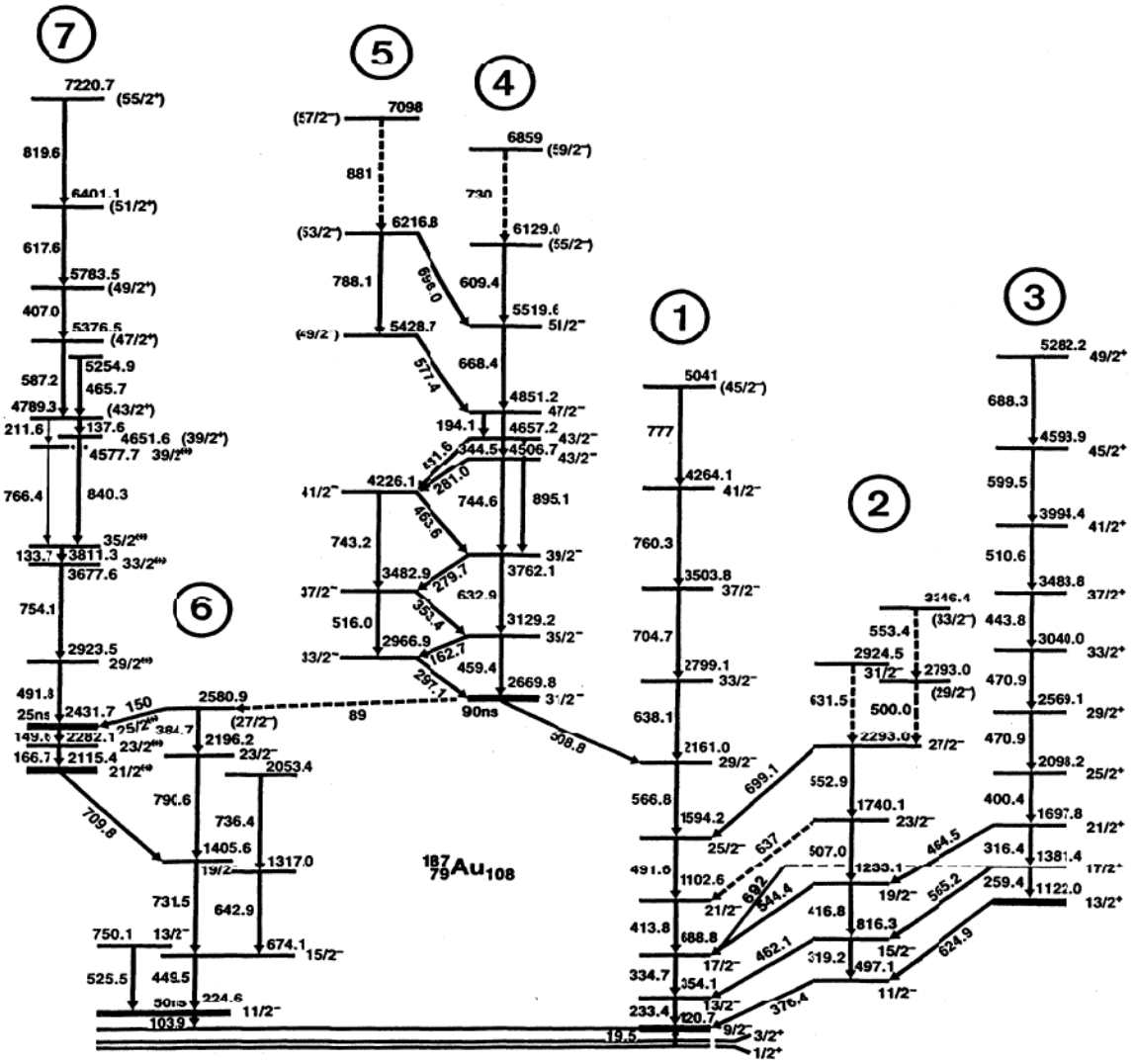

Figure 2.8: Decay scheme of ^{187}Au based on ^{172}Yb(^{19}F,4n) reaction, taken from [6].

2.4.1 Details of the experiment

While the beams at iThemba LABS are delivered to the users for 24 hours per day and seven days a week, for nuclear research the beam is available from 18h00 on Friday to 05h00 on Monday. The experiment marked PR235 had beam times reserved for three consecutive weekends in November 2014 (7. 11. – 24. 11.). The ^{187}Au isotope was produced in two different HI fusion-evaporation reactions using ion beams accelerated with the SPC2 and SSC accelerators and heavy nuclei targets positioned in the target chamber of the AFRODITE array. The reactions were ^{175}Lu(^{16}O,4n)^{187}Au

with the beam energy 77 MeV and ^{181}Ta(^{12}C,6n)^{187}Au with the beam energy 89 MeV. Detailed parameters of the experiment are listed in Tab. 2.2. The used 4n and 6n reaction channels were determined to be the most dominant by calculation using the HIVAP statistical-evaporation model [46]. Most dominant contaminations (due to channels with charged-particle evaporation) were calculated to be lower by a factor 3 and the fission channel was under 10 %, therefore it was decided that recoil-decay tagging was not necessary for in-beam gamma-ray spectroscopy of ^{187}Au produced in those two reactions under given circumstances.

	1st week	**2nd week**	**3rd week**
Date	7. 11. - 10. 11.	14. 11. - 17. 11.	21. 11. – 24. 11.
Beam	^{16}O	^{12}C	^{12}C
Beam energy	77 MeV	89 MeV	89 MeV
Target	^{175}Lu	^{181}Ta	^{181}Ta
Target thickness	4 mg·cm^2	1.1 mg·cm^2	1.1 mg·cm^2

Table 2.2: The details of ^{187}Au production in the experiment PR235.

For the experiment PR235, AFRODITE was equipped with 14 detectors marked with numbers from 1 to 16 representing their position in the array, positions 5 and 7 were empty. Positions 1 – 4 were at 135° and all contained Clover detectors, positions 13 – 16 were at 45° and contained LEPS detectors and positions 6, 8 – 12 were at 90° and contained 2 LEPS (positions 8, 9) and 4 Clover (positions 6, 10 – 12) detectors (see Fig 3.2 for angle positions). This means a total of 8 Clover and 6 LEPS detectors were used for the experiment. Individual crystals of the Clover detectors were marked with letters and colours: a – Black, b – Blue, c – Green and d – Red. When in position, the centre of the detector was precisely at the given angle (45°, 90° or 135°), while the angles of the crystals were shifted by ± 5°. Every Clover detector was positioned in the same direction so that Black and Blue crystals were at 85° and 130° degrees and Green and Red crystals were at 95° and 140° degrees, respectively. BGO suppression shields were equipped to all 8 Clover detectors, Tab. 2.3 shows the values of the Compton background suppression for each crystal (3 values were not listed in the experiment log).

Clover detector number	array position	Clover crystals			
		a	b	c	d
C1	3	16.0 %	15.0 %	15.0 %	15.0 %
C2	6	16.0 %	16.0 %	16.0 %	16.0 %
C3	10	18.0 %	19.0 %	-	17.6 %
C4	12	20.9 %	20.0 %	23.0 %	21.9 %
C5	1	20.7 %	19.5 %	22.1 %	20.9 %
C6	4	-	14.0 %	-	14.0 %
C7	2	22.0 %	21.9 %	21.1 %	22.7 %
C8	11	14.0 %	14.0 %	15.0 %	13.7 %

Table 2.3: Compton background suppression for each Clover crystal

2.5 Data acquisition and analysis

2.5.1 Data acquisition system for AFRODITE

The data acquisition (DAQ) system for the experiment PR235 was based on Digital Gamma Finder (DGF) Pixie-16 modules developed by XIA LLC [47, 48]. Each module accepts signals directly from preamplifiers of the germanium crystals and the BGO shields. The modules are connected to the DAQ system via fast PXI bus. The incoming analog signals are amplified and subsequently digitized with 12-bit precision. All events are time-stamped with an internal 100 MHz clock. The Pixie-16 modules allow to collect the complete traces of signals, however this option is not suitable for in-beam gamma-ray spectroscopy due to high counting rate of germanium detectors (the speed of the PXI wouldn't be sufficient for such a mode). The digitalized data is transported into the controller PC, where the events are reconstructed by the Event builder of the Multi Instance Data Acquisition System (MIDAS) developed at STFC Daresbury Laboratory [49]. The Event builder allows to prefilter the data. For the experiment PR235, only events when two or more germanium crystals generated coincidence signals were written down. The energies and signals from the BGO shields were not written but signals in coincidence with the BGO shields were directly discarded. The measured data was then written on the disk in the EUROGAM data format [50].

2.5.2 Data Analysis

The analysis of the data from the experiment was carried out solely at the Institute of Physics, Slovak Academy of Sciences in Bratislava. During the three weekends of the experiment, more than 5.5 TB of data were obtained and recorded on a disc. It was written in a tree data structure consisting of three values. In this data structure, every event is categorized by its channel (number of the detector crystal where the event was registered), raw energy (uncalibrated energy of the registered event) and a time-stamp from the internal clock, which determines the time when the event was registered during the experiment. The first step in the analysis was the development of our own analytical software for reading raw data. The composed program was written in C++ utilizing the ROOT data analysis framework [51].

The program reads the tree structured raw data and allows us to reconstruct gamma-ray singles for every detector as well as to create coincidence spectra for various detector and peak configurations (e.g. coincidence with a single gamma line). The gate interval for coincidences can be changed to any required value. Plotting the subtraction of time-stamp values for the events registered consecutively in time in all the Clover crystals, we get Fig. 2.9. This Figure shows that most coincidence events are registered within approximately 20 ns after the incident gamma-ray. After analysing this spectrum, we decided to set the gates for prompt coincidence at 0 – 20 ns and for random coincidence at 60 – 80 ns. The coincidence spectra in the program were created from events in prompt coincidence with each other while the events with random coincidence were subtracted as background. The same behaviour in coincidence time was observed for LEPS detectors, therefore the same gate intervals were chosen.

Standard sources listed in Tab 2.4 were used for the calibration of the detectors used in the experiment. Data from the calibration measurements were run through the program and the acquired spectra were analysed. Fitted peak positions in the raw energy spectra were calibrated with a quadratic function. Calibration was performed on each Clover element and LEPS segment separately.

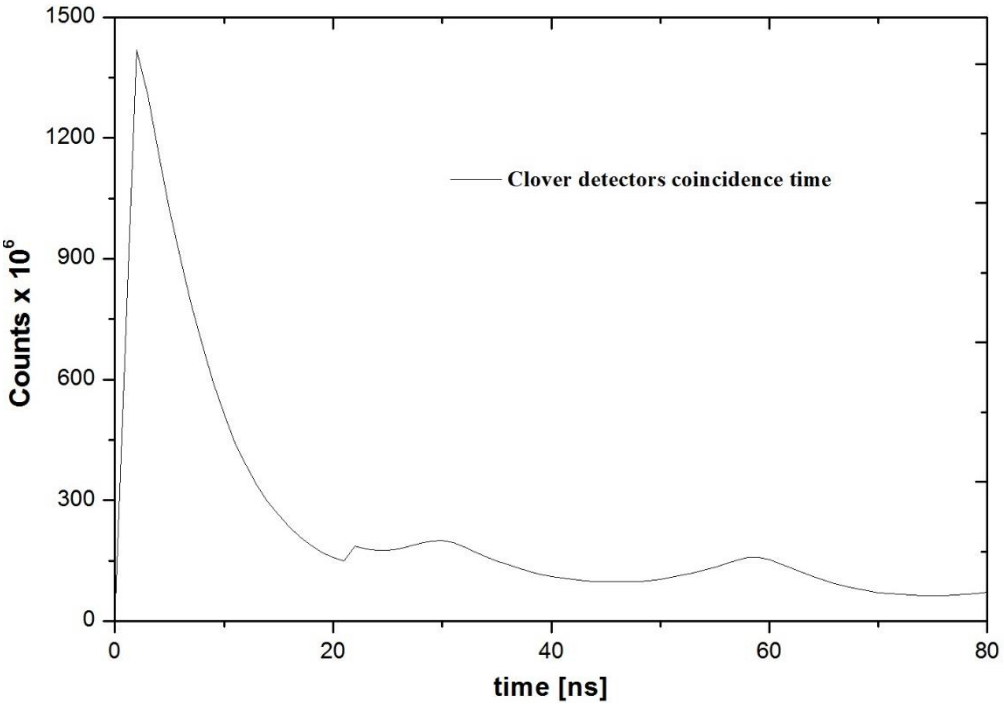

Figure 2.9: Coincidence times for Clover detectors.

Detector	Source	Gamma Lines [keV]
Clover	^{241}Am (1Q848, 457.3 kBq, 1.4.1984)	59.5
	^{60}Co (B7-533, 375.6 kBq, 1.6.2004)	1173.2, 1332.5
	^{133}Ba (1R797, 396.6 kBq, 1.4.1984)	81.0, 276.4 302.9, 356.0 383.9
	^{137}Cs (2S027, 375.9 kBq, 1.4.1984)	661.7
	^{152}Eu (B7-535, 363.6 kBq, 1.6.2004)	121.8, 244.7 344.3, 444.0 779.0, 964.1 1112.1, 1408.0
LEPS	^{241}Am (1Q848, 457.3 kBq, 1.4.1984)	59.5
	^{133}Ba (1R797, 396.6 kBq, 1.4.1984)	53.2, 81.0 276.4, 302.9 356.0, 383.9

Table 2.4: List of calibration sources and gamma-lines used in the experiment PR235.

The employed analytical program has the option to correct the data and the output spectra (if necessary) for the Doppler effect. In these types of experiments, the Doppler effect occurs because the recoils, given enough energy from the beam in the reaction, escape the target and still emit gamma-rays while in motion. Using SRIM (the Stopping and Range of Ions in Matter) software package [52, 53], we calculated the recoil (created in the middle of the target) energy at approximately 2.23 MeV in the moment of leaving the target, which equals $v/c = 5 \cdot 10^{-3}$.

Another feature of the program is the addition of add-back calculations for both Clover and LEPS detectors. The principle of this technique is described in 2.3.2. For the calculations, the same gate interval as for the prompt coincidence was chosen (0 – 20 ns). The incorporation of the add-back technique led to a considerable decrease in the Compton part of the spectra. The differences for both Clover and LEPS detectors for our experimental data are shown in Figures 2.10 and 2.11.

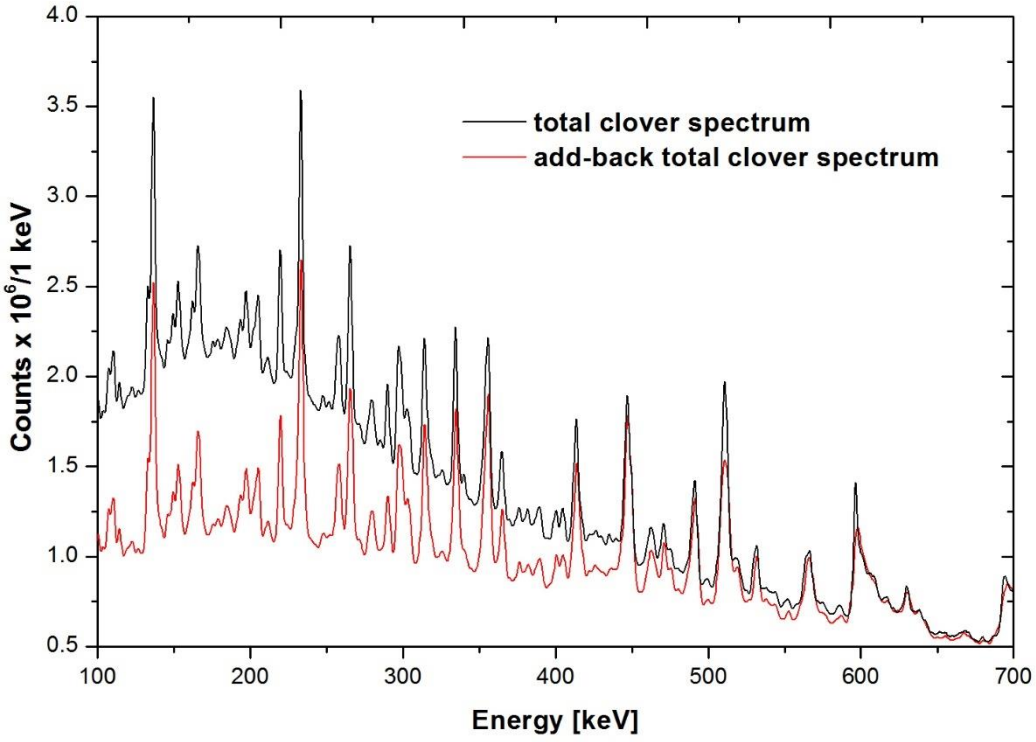

Figure 2.10: Decrease in the Compton part of the spectra for all Clover detectors using the add-back technique calculations.

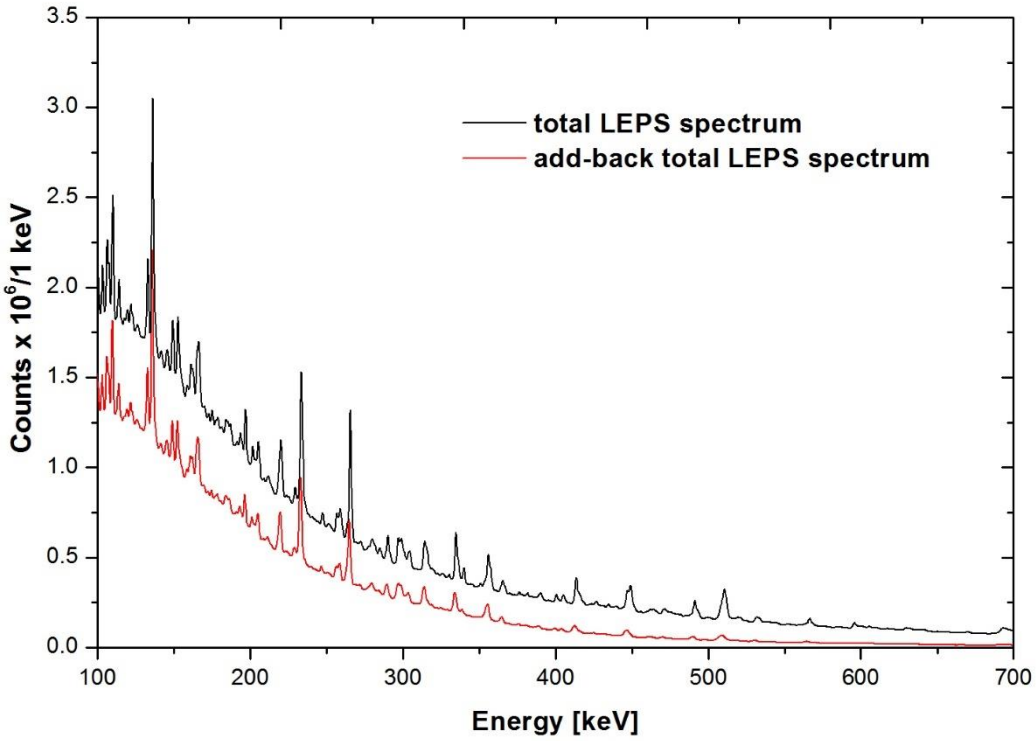

Figure 2.11: Decrease in the Compton part of the spectra for all LEPS detectors using the add-back technique calculations.

The output file of our program after sorting the data contains several one- and two-dimensional spectra. The two-dimensional spectra, so called γ-γ matrixes, where the main results of the programs analysis. They were constructed from coincidence events from selected detectors. A singe γ-γ matrix contains all the coincidences of the selected detectors. After that, the main data analysis was performed using the RadWare software package [8, 9]. The γ-γ matrixes were extracted from the output file and analysed with ESCL8R, an interactive program for easy and fast graphical inspections of γ-γ data [8]. The matrix for the program must be symmetrised, meaning the energy axes are identical. ESCL8R requires efficiency calibrations, energy calibrations and 2D background subtraction for the studied data. Efficiency calibrations are obtained from EFFIT, energy calibrations from ENCAL, and the 2D background subtraction is performed in GF3, all RadWare package programs. The 2D background was created from *x* and *y* axis projections of the matrix, using SLICE. The background subtraction algorithm is described in [9]. In ESCL8R, during analysis of the gamma-rays, a proposed level scheme is constructed and can be stored for further usage. For transitions assigned in the level scheme, ESCL8R can perform calculations of intensities, internal

conversion coefficients, transition and level energies. The requirement for reliable calculated coefficients is the accurate assignment of transitions in the level scheme. Simultaneously, these calculations can reveal mistakes in the proposed level scheme. In our data analysis, detector calibrations were performed before early, not in RadWare, therefore ENCAL was not used. The efficiency calibration was performed using EFFIT, where the function of the efficiency is defined as:

$$\text{eff} = e^{\left\{\left[\left(A+B*x+C*x^2\right)^{-G}+\left(D+E*y+F*y^2\right)^{-G}\right]^{-\frac{1}{G}}\right\}} \qquad (2.13)$$

Parameters *A* - *G* are obtained by fitting the efficiency calibration curve, *A* - *C* define the efficiency at lower energies, *D* - *F* at higher energies. x = log(E_γ/100 keV) and y = log(E_γ/1000 keV). Fig. 2.12 shows the efficiency calibration curve from the program and Tab. 2.5 lists the values of the parameters.

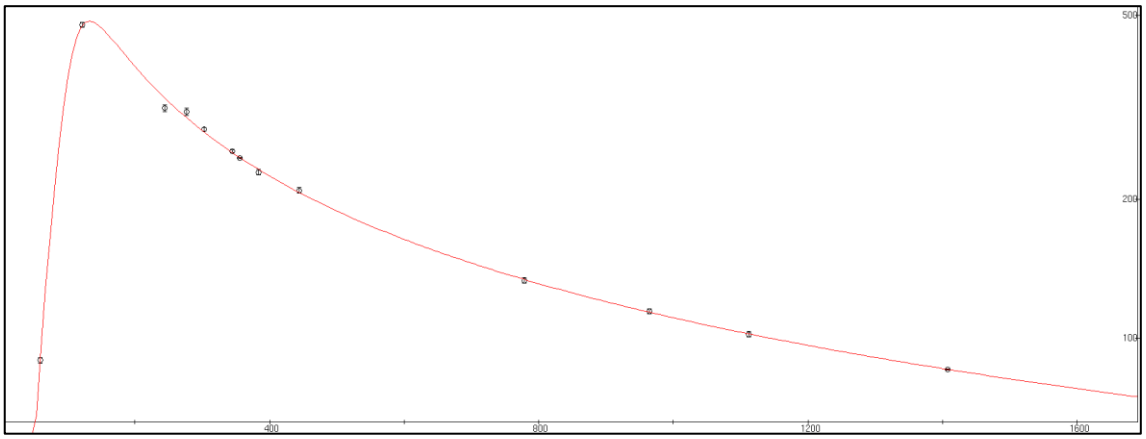

Figure 2.12: Efficiency curve fit for the AFRODITE detectors in the experiment PR235.

	A	**B**	**C**	**D**	**E**	**F**	**G**
Ring 1	5.2	1.5	0	4.655	-0.899	0.007	15

Table 2.5: Efficiency equation parameters obtained by EFFIT for AFRODITE detectors.

Similar to the γ-γ matrixes, triple coincidence structures, called γ-γ-γ cubes can be constructed in RadWare. The requirements for this are at least three detectors and a high data statistic, since only events registered at the same time in three and more detectors are suitable. In a γ-γ-γ cube, spectra that are in coincidence with two

transitions at once can be generated and analysed. Since our experimental data has high statistics, alongside γ-γ matrixes, we also constructed a γ-γ-γ cube from the Clover data. The main program for the examination and analysis of the cube is called LEVIT8R. As with the matrix, several other programs are used to modify the data for the final program, including EFFIT, ENCAL, INCUB8R for the construction of the cube and PRO3D for two-dimensional projections. LEVIT8R works similarly as ESCL8R. A level scheme is constructed from the spectra, but the transition intensities and the count rates are much lower. We used the Clover γ-γ-γ cube to confirm or reject the transitions observed in ESCL8R.

While written primarily for the analysis of the data from the experiment PR235, the program in co-operation with RadWare can reconstruct and analyse any kind of gamma-ray spectroscopy data recorded in a similar data structure.

3 Experimental results and discussion

The present work contains results of a spectroscopic study of the neutron-deficient isotope ^{187}Au. By using several nuclear spectroscopic methods, we obtained knowledge about this isotope and constructed a level scheme based on the newly analysed data and the previous studies of ^{187}Au [6, 7]. The experiment was carried out at iThemba LABS, employing fusion-evaporation reactions to produce the isotope, and in-beam gamma-ray spectroscopy for measurement of the outgoing gamma-rays, which contain valuable information on the produced isotope. The subsequent analysis utilized the ROOT data analysis framework and the RadWare software package. Directional correlations from oriented states and linear polarization methods were used to determine and assign spin and parity to the states of the deduced level scheme. The analysis of the data run into a serious (and unfortunately unsolvable) problem, the contaminations from other isotopes produced in the reaction were very significant, as opposed to the prediction for the experiment. The data analysis of the experiment was carried out offline, therefore the presence of the contaminations was discovered well after the actual experiment. Several attempts were made to remove (e.g. gating on characteristic gold X-rays) or to lower the contaminations (shorter coincidence times, using γ-γ-γ cubes) in the data. They could not be removed, but some of the applied methods were partially successful. These circumstances contributed to the fact that no new transition was assigned to the level scheme, since we could not in good conscience decide whether the observed transition originates from the studied isotope or from a contamination. However, the band structures of the *intruder state* configuration were clearly not present in our data, even with the presence of contaminations. Concluding that they must have a different structure than predicted.

3.1 Results for ^{187}Au

The ^{187}Au isotope nucleus consists of 79 protons and 108 neutrons, it has a half-life of 8.3 minutes. The ground state of the isotope is $1/2^+$ [54], corresponding to the $3s_{1/2}$ orbital (see Fig. 1.2). It decays by electron capture (~100%) to ^{187}Pt and a very small percentage (0.003%) by alpha decay to ^{183}Ir. There are also isomeric states identified in the previous studies of ^{187}Au. Most notably the intruder $9/2^-$ state at 120.3 keV, with a half-life of 2.3 seconds [56], other isomeric states have half-lives in the order of nanoseconds [6].

The level scheme of ^{187}Au, deduced from the experimental data is shown in Figures 3.1 and 3.2. It is composed from 9 bands, that were labelled with numbers (no significant order), and some other "non-band" transitions. The level scheme was constructed in RadWare and contains transition energies, level energies, spins and parities of the states and intensities of transitions. The transition intensities in the level scheme are displayed as the thickness of the arrows, the thicker the arrow, the higher the intensity of the transition. The blank part of the arrows (e.g. $13/2^- \rightarrow 9/2^-$ transition in *Band 1*) represents the percentage of the transition that decays via conversion electrons. The placement of the individual transitions into the level scheme was based on γ-γ and γ-γ-γ coincidences that were constructed from the data. Most of the transitions were assigned based on coincidence gates, where gated spectra directly showed the transitions in coincidence. The lower spin transitions have higher intensities, moving the coincidence gate up to higher transitions that are in coincidence shows us better in what order the low intensity transitions are in the same band or structure. The final order of the transitions in the scheme was mainly determined by their intensity and energy (higher spin transitions have usually higher transition energy). The intensities in the level scheme must also take into account the feeding of the transitions from above.

Tab. 3.1 shows all the transitions from the present data that were assigned to the ^{187}Au level scheme. The table contains transition energies E_γ, relative intensities I_γ (normalized with transition 413.79 keV from *Band 1*), initial level energies E_i, internal conversion coefficients α and initial and final level spins I_i^π, I_f^π. All the values and their respective errors (when listed) were obtained from RadWare.

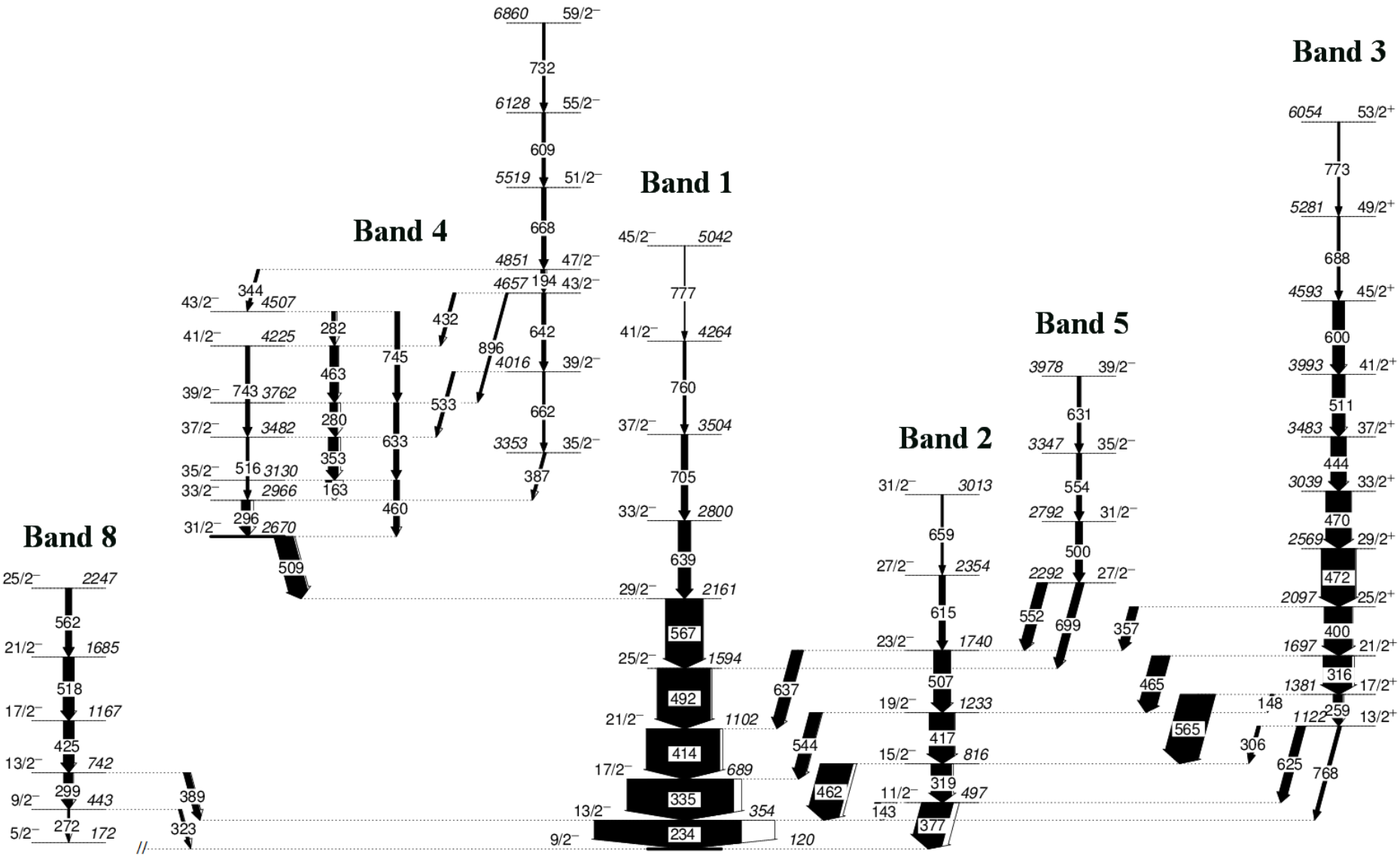

Figure 3.1: Level scheme of ^{187}Au, deduced from our experimental data.

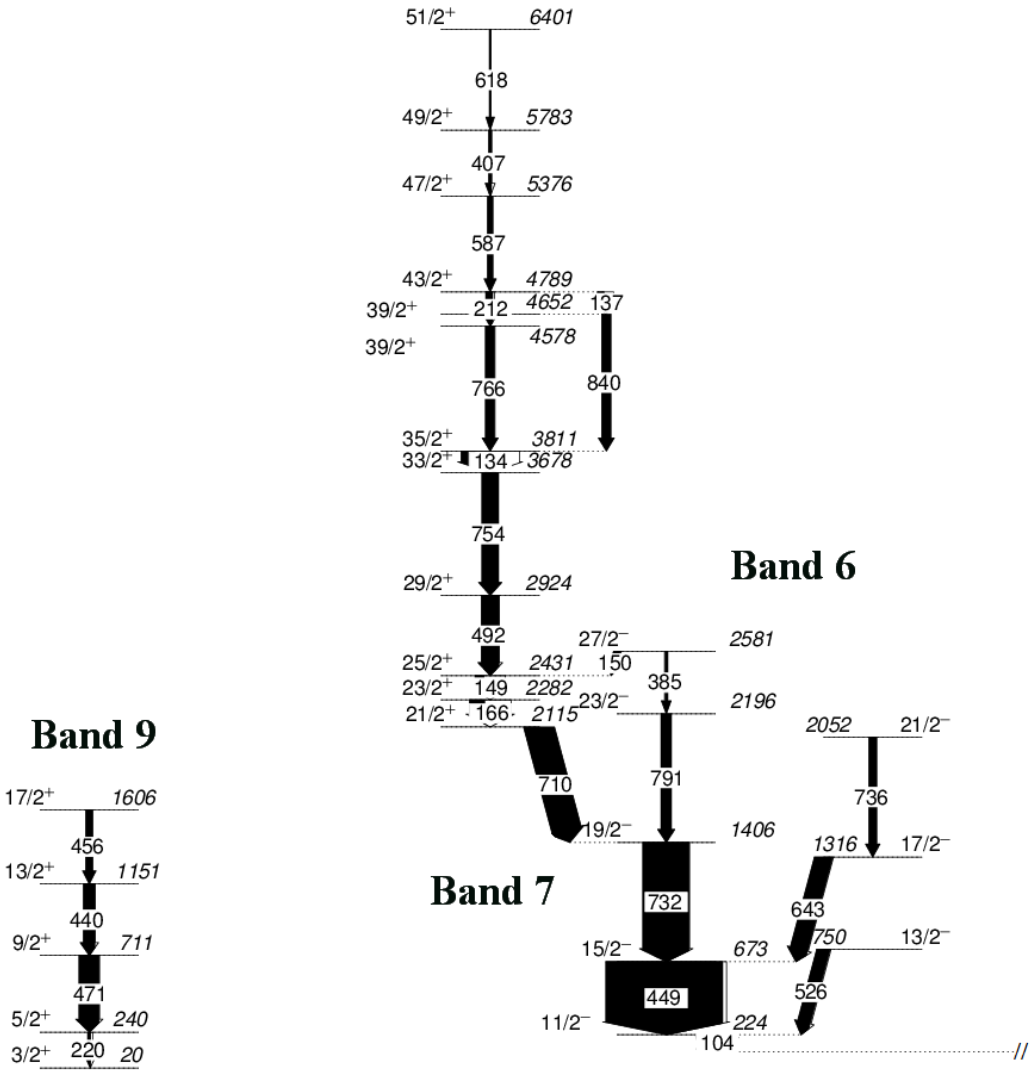

Figure 3.2: Level scheme of ^{187}Au, deduced from our experimental data - continued

E_γ [keV]	I_γ [%]	E_i [keV]	α	I_i^π	I_f^π
Band 1					
233.68(3)	188(8)	354.0	2.3E-01	$13/2^-$	$9/2^-$
334.67(3)	140(6)	688.7	7.5E-02	$17/2^-$	$13/2^-$
413.79(4)	100(4)	1102.5	4.2E-02	$21/2^-$	$17/2^-$
491.66(4)	73(3)	1594.0	2.7E-02	$25/2^-$	$21/2^-$
566.96(4)	51(2)	2161.0	1.9E-02	$29/2^-$	$25/2^-$
638.65(8)	17(1)	2799.6	1.5E-02	$33/2^-$	$29/2^-$
704.55(14)	9(1)	3504.2	1.2E-02	$37/2^-$	$33/2^-$
760.06(20)	4.2(8)	4264.2	1.0E-02	$41/2^-$	$37/2^-$
777.44(61)	1.3(8)	5041.7	9.7E-03	$45/2^-$	$41/2^-$
Band 2					
143.0(2)	8(2)	497.0	2.7E+00	$11/2^-$	$13/2^-$
318.93(4)	28(2)	815.9	8.6E-02	$15/2^-$	$11/2^-$
376.70(5)	42(12)	497.0	1.9E-01	$11/2^-$	$9/2^-$
416.79(5)	34(2)	1232.7	4.1E-02	$19/2^-$	$15/2^-$
462.01(4)	43(3)	815.9	1.1E-01	$15/2^-$	$13/2^-$
506.83(7)	23(2)	1739.7	2.5E-02	$23/2^-$	$19/2^-$
544.03(8)	16(1)	1232.7	7.1E-02	$19/2^-$	$17/2^-$
614.7(2)	8(2)	2354.4	1.6E-02	$27/2^-$	$23/2^-$
636.6(1)	15(1)	1739.7	4.7E-02	$23/2^-$	$21/2^-$
659.0(4)	2.6(9)	3013.4	1.4E-02	$31/2^-$	$27/2^-$
Band 3					
148.1(2)	5(1)	1380.7	1.6E-01	$17/2^+$	$19/2^-$
258.8(1)	13(1)	1380.7	1.6E-01	$17/2^+$	$13/2^+$
306.0(3)	5(1)	1121.9	2.6E-02	$13/2^+$	$15/2^-$
316.50(5)	38(2)	1697.7	8.8E-02	$21/2^+$	$17/2^+$
356.7(1)	12(1)	2097.3	1.8E-02	$25/2^+$	$23/2^-$
400.15(4)	37(2)	2097.3	4.6E-02	$25/2^+$	$21/2^+$
443.85(6)	21(1)	3482.7	3.5E-02	$37/2^+$	$33/2^+$
464.68(6)	24(2)	1697.7	1.0E-02	$21/2^+$	$19/2^-$
469.85(5)	34(2)	3038.9	3.0E-02	$33/2^+$	$29/2^+$
471.77(4)	46(2)	2659.0	3.0E-02	$29/2^+$	$25/2^+$
510.59(7)	17(1)	3993.3	2.5E-02	$41/2^+$	$37/2^+$
564.83(5)	46(3)	1380.7	6.7E-03	$17/2^+$	$15/2^-$

E_γ [keV]	I_γ [%]	E_i [keV]	α	I_i^π	I_f^π
Band 3	- continued				
599.51(8)	16(1)	4592.8	1.7E-02	$45/2^+$	$41/2^+$
625.0(2)	12(2)	1121.9	5.4E-03	$13/2^+$	$11/2^-$
687.9(2)	4.0(8)	5280.8	1.3E-02	$49/2^+$	$45/2^+$
768.0(3)	5(2)	1121.9	3.6E-03	$13/2^+$	$13/2^-$
773.4(3)	2.7(6)	6054.2	9.8E-03	$53/2^+$	$49/2^+$
Band 4					
163.26(8)	8.3(6)	3129.5	1.9E+00	$35/2^-$	$33/2^-$
280.04(7)	10.3(7)	3762.2	4.2E-01	$39/2^-$	$37/2^-$
281.8(1)	5.3(7)	4507.3	4.1E-01	$43/2^-$	$41/2^-$
296.45(6)	12.3(9)	2966.3	3.6E-01	$33/2^-$	$31/2^-$
352.70(6)	13.3(9)	3482.2	2.2E-01	$37/2^-$	$35/2^-$
459.9(1)	7.9(8)	3129.5	3.2E-02	$35/2^-$	$31/2^-$
463.04(8)	11.3(9)	4225.4	1.1E-01	$41/2^-$	$39/2^-$
508.81(4)	26(1)	2669.8	8.4E-02	$31/2^-$	$29/2^-$
515.9(2)	3.7(7)	3482.2	2.4E-02	$37/2^-$	$33/2^-$
633.1(1)	7.4(8)	3762.2	1.5E-02	$39/2^-$	$35/2^-$
743.2(1)	5.8(7)	4225.4	1.1E-02	$41/2^-$	$37/2^-$
745.4(1)	6.4(7)	4507.3	1.1E-02	$43/2^-$	$39/2^-$
Band 5					
499.84(6)	9.5(7)	2792.3	2.6E-02	$31/2^-$	$27/2^-$
552.43(6)	13.9(8)	2292.5	2.1E-02	$27/2^-$	$23/2^-$
554.32(8)	6.7(5)	3346.6	2.0E-02	$35/2^-$	$31/2^-$
631.4(1)	5.4(5)	3978.0	1.5E-02	$39/2^-$	$35/2^-$
698.80(6)	10.4(7)	2292.5	3.7E-02	$27/2^-$	$25/2^-$
Band 6					
103.6(1)	4.7(5)	223.9	6.8E+00	$11/2^-$	$9/2^-$
149.6(1)	7(1)	2581.0	1.5E-01	$27/2^-$	$25/2^+$
384.8(3)	3(1)	2581.0	5.1E-02	$27/2^-$	$23/2^-$
449.43(5)	119(23)	673.4	3.4E-02	$15/2^-$	$11/2^-$
526(1)	26(3)	749.7	7.7E-02	$13/2^-$	$11/2^-$
642.9(1)	18(3)	1316.3	4.6E-02	$17/2^-$	$15/2^-$
732.35(5)	47(3)	1405.7	1.1E-02	$19/2^-$	$15/2^-$
736.0(2)	8(1)	2052.2	1.1E-02	$21/2^-$	$17/2^-$

E_γ [keV]	I_γ [%]	E_i [keV]	α	I_i^π	I_f^π
Band 6	- continued				
790.8(1)	11(2)	2196.4	9.3E-03	$23/2^-$	$19/2^-$
Band 7					
133.61(7)	14(1)	3811.5	3.3E+00	$35/2^+$	$33/2^+$
136.9(1)	6.7(8)	4789.0	1.5E+00	$43/2^+$	$39/2^+$
149.5(1)	9(1)	2431.4	2.4E+00	$25/2^+$	$23/2^+$
166.47(7)	16(1)	2281.9	7.6E-01	$23/2^+$	$21/2^+$
211.57(8)	7.0(6)	4789.0	3.1E-01	$43/2^+$	$39/2^+$
406.9(2)	2.9(7)	5783.0	1.5E-01	$49/2^+$	$47/2^+$
492.44(7)	18(2)	2923.8	2.7E-02	$29/2^+$	$25/2^+$
587.1(2)	5.6(8)	5376.1	1.8E-02	$47/2^+$	$43/2^+$
617.7(4)	1.9(8)	6400.7	5.1E-02	$51/2^+$	$49/2^+$
709.68(5)	31(2)	2115.4	4.2E-03	$21/2^+$	$19/2^-$
754.05(6)	17(1)	3677.9	1.0E-02	$33/2^+$	$29/2^+$
766.39(9)	9.6(9)	4577.7	1.0E-02	$39/2^+$	$35/2^+$
840.1(1)	9.4(9)	4651.9	8.2E-03	$39/2^+$	$35/2^+$
Band 8					
271.6(2)	2.5(6)	443.4	1.4E-01	$9/2^-$	$5/2^-$
298.59(9)	13(2)	742.2	1.1E-01	$13/2^-$	$9/2^-$
322.9(1)	3.5(3)	443.4	2.8E-01	$9/2^-$	$9/2^-$
388.6(1)	8(1)	742.2	1.7E-01	$13/2^-$	$13/2^-$
424.91(7)	15(2)	1167.1	3.9E-02	$17/2^-$	$13/2^-$
517.76(7)	15(1)	1684.9	2.4E-02	$21/2^-$	$17/2^-$
Band 9					
220.28(9)	3.0(1)	240.5	8.1E-01	$5/2^+$	$3/2^+$
381.9(4)	2.1(8)	1150.6	5.2E-02	$13/2^+$	$9/2^+$
439.54(8)	12(1)	1150.6	3.6E-02	$13/2^+$	$9/2^+$
455.8(1)	7.9(9)	1606.4	3.3E-02	$17/2^+$	$13/2^+$
470.67(7)	22(3)	711.1	3.0E-02	$9/2^+$	$5/2^+$
Other					
193.73(6)	5.6(4)	4851.1	4.2E-01	$47/2^-$	$43/2^-$
343.84(9)	3.4(3)	4851.1	7.0E-02	$47/2^-$	$43/2^-$
386.9(1)	3.3(4)	3353.3	1.7E-01	$35/2^-$	$33/2^-$

E_γ [keV]	I_γ [%]	E_i [keV]	α	I_i^π	I_f^π
Other	- continued				
431.8(1)	3.9(4)	4657.4	1.3E-01	$43/2^-$	$41/2^-$
532.9(1)	4.1(5)	4015.5	7.5E-02	$39/2^-$	$37/2^-$
608.9(1)	4.6(5)	6127.9	1.6E-02	$55/2^-$	$51/2^-$
641.58(8)	5.3(5)	4657.4	1.5E-02	$43/2^-$	$39/2^-$
662.0(1)	3.3(4)	4015.5	1.4E-02	$39/2^-$	$35/2^-$
667.91(7)	6.1(4)	5519.0	1.3E-02	$51/2^-$	$47/2^-$
732(1)	3.7(4)	2061.2	1.1E-02	$21/2^-$	$17/2^-$
895.66(9)	3.5(3)	4657.4	7.3E-03	$43/2^-$	$39/2^-$

Table 3.1: Gamma-ray transitions in our experimental data assigned to the level scheme of ^{187}Au.

3.1.1 *Band 1* and *4*

Band 1 in our level scheme contains the highest intensity transitions and can be described as the main band in ^{187}Au. The band-head has a spin of $9/2^-$ and is located at 120 keV. It has a half-life of 2.3 seconds and decays by isomeric transition (100%) to the $3/2^+$ state by a 101 keV E3 transition [56]. The $3/2^+$ state has a half-life of 6.5 nanoseconds [6] and decays to the $1/2^+$ ground state at 0 keV, which has an oblate shape [7, 57]. The $9/2^-$ state corresponds to a proton, located at the $1h_{9/2}$ orbital, coupled with an even-even $_{78}$Pt core. The proton crosses the closed shell at 82 (see Fig. 1.2) and therefore the $9/2^-$ state is categorized as an *intruder state*. The band structure was previously observed in [6, 7]. No new transitions were assigned in the present study beyond the $45/2^+$ state. The lower states up to spin $29/2^-$ have side-feeding from other bands. No conclusive transitions from *Band 1* to another band have been identified, similar to the previous in-beam gamma-ray measurements. Fig. 3.3 shows the spectrum gated at the 567.0 keV transition that depopulates the *Band 1* $29/2^-$ state. We can see the lower transitions of the band structure plus transitions from *Band 4*, which populates the $29/2^-$ state with a 508.8 keV (M1+E2) transition. Fig. 3.4 shows the spectrum gated at the 638.6 keV transition that feeds the $29/2^-$ state of *Band 1*, where no transitions from *Band 4* are present. Therefore, we can confirm that the side-feeding occurs at the $29/2^-$ state. This fact can be better observed in Fig. 3.7, that shows the γ-γ-γ cube spectrum gated at both 567.0 keV and 638.6 keV. The isomeric band-head of *Band 4* lies at 2670

keV with a spin of $31/2^-$ and a half-life of 90 nanoseconds [6] (100 ns in [7]). The transitions in *Band 4* are shown in Fig. 3.5, gated at 508.8 keV. A high-spin structure with lower intensity transitions that side-feeds *Band 4* has been observed (see Fig. 3.1). Part of the structure appeared in [7] and part in [6], where it was labelled as a separate band (Band 5 in Fig. 2.8). Because of the lower intensities, the transitions are listed in the "Other" section of Tab. 3.1 and not as part of the band.

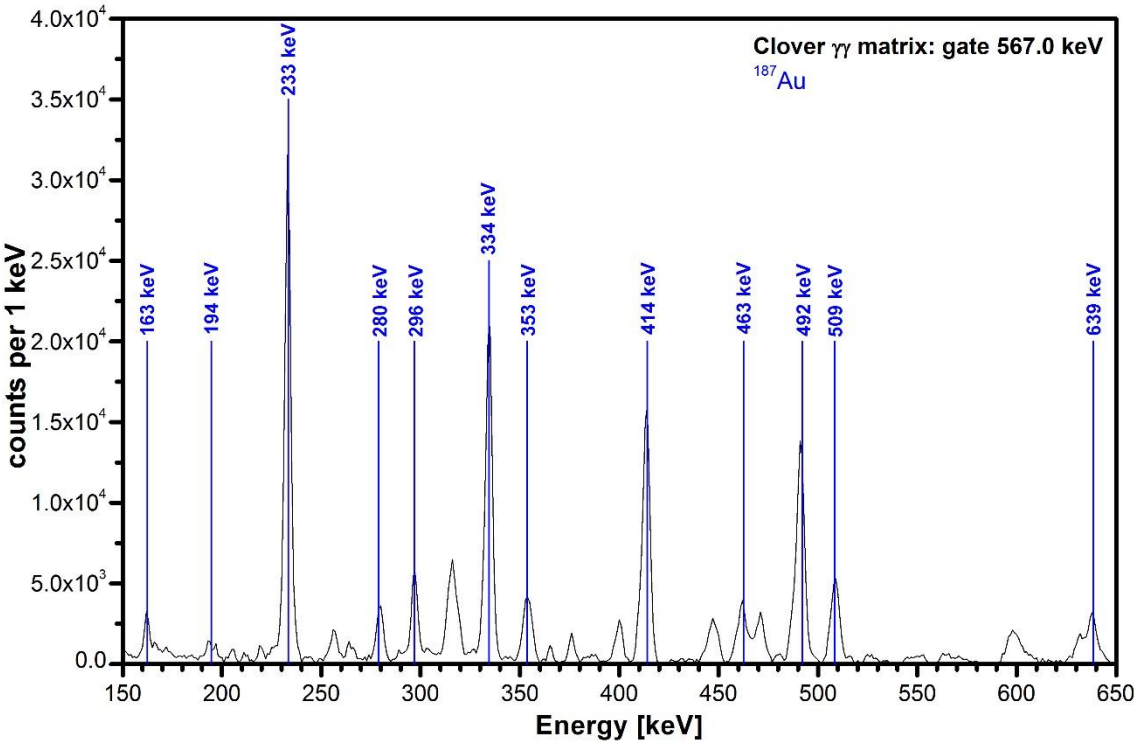

Figure 3.3: Energy spectrum gated at 567.0 keV.

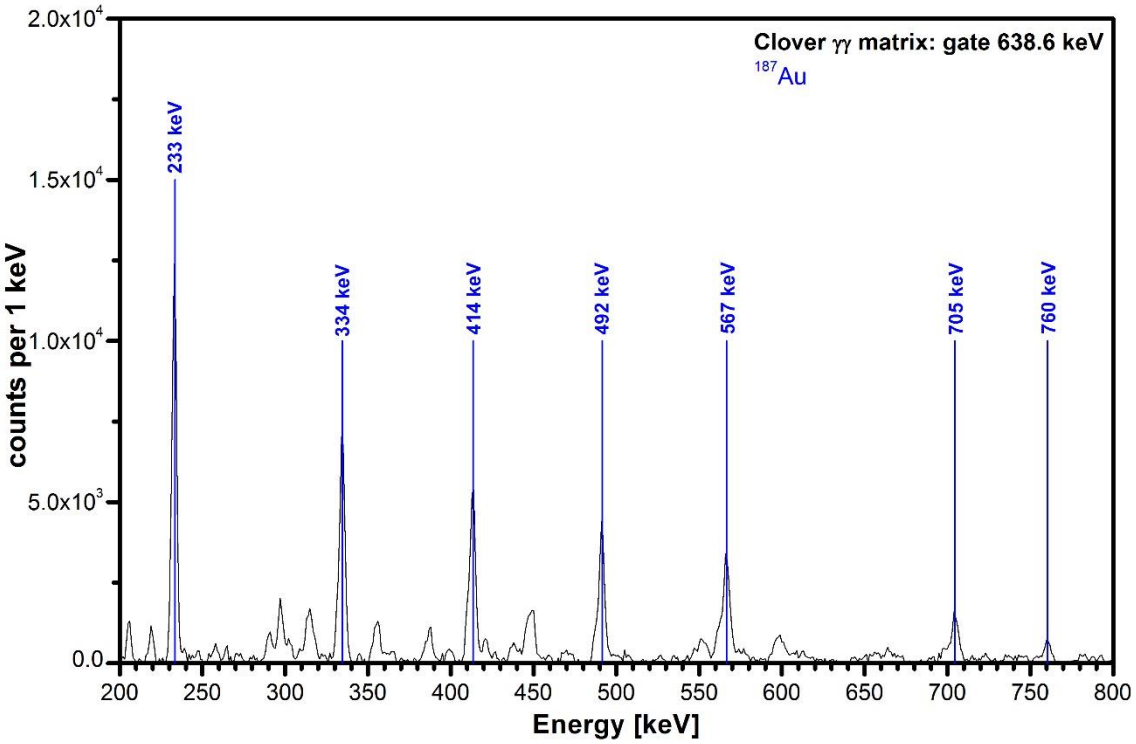

Figure 3.4: Energy spectrum gated at 638.6 keV.

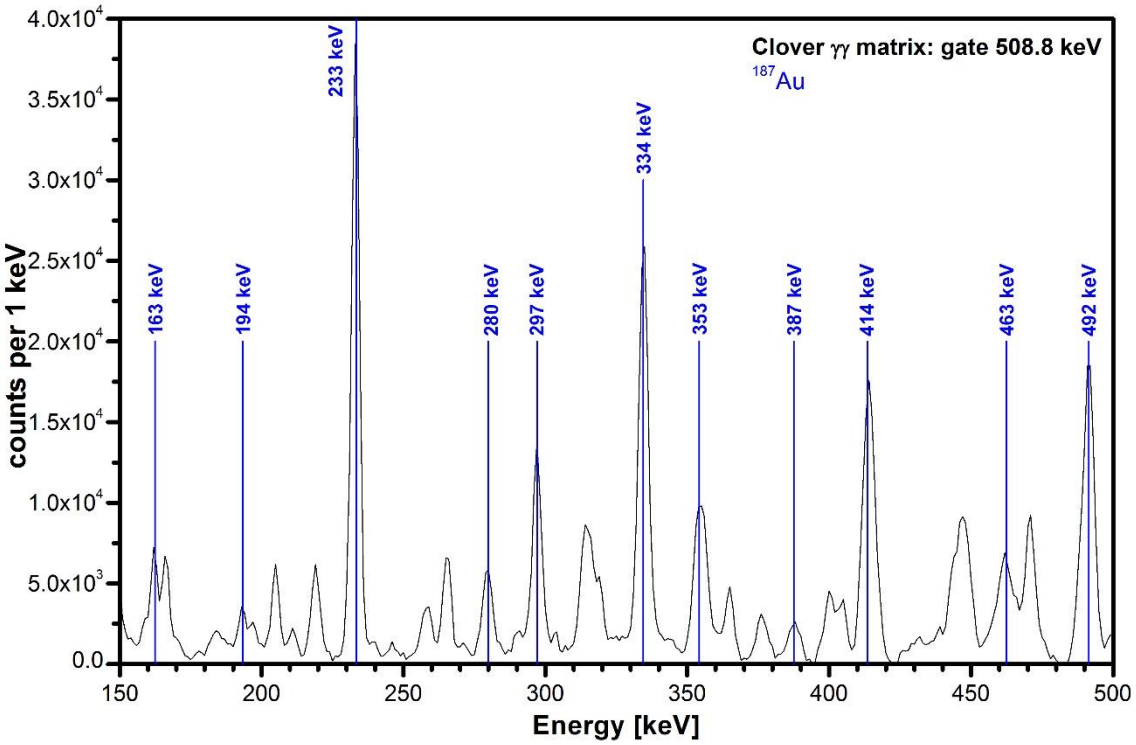

Figure 3.5: Energy spectrum gated at 508.8 keV.

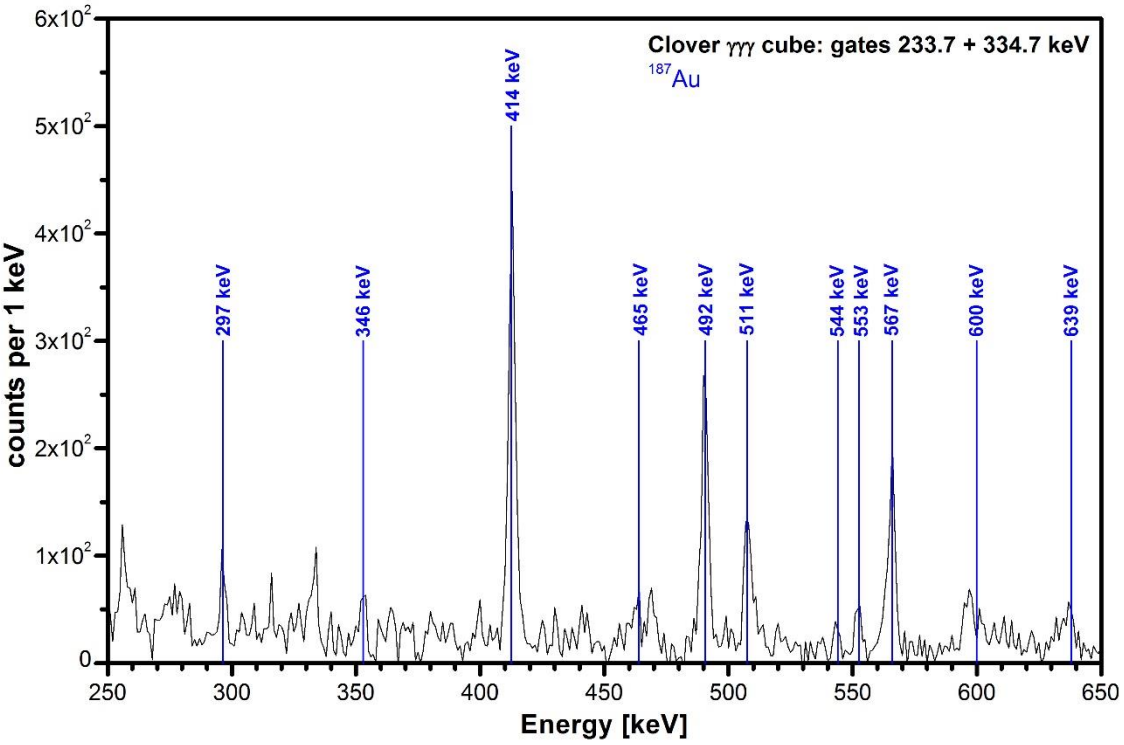

Figure 3.6: Energy spectrum gated at both 233.7 keV and 334.7 keV.

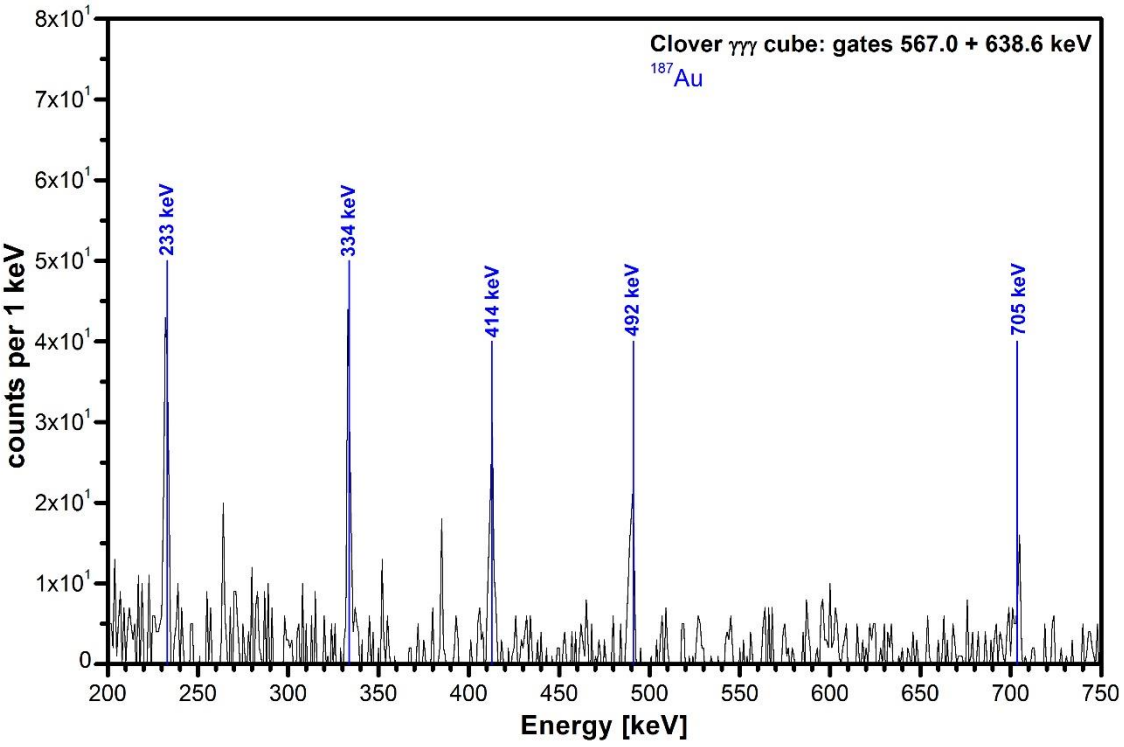

Figure 3.7: Energy spectrum gated at both 567.0 keV and 638.6 keV.

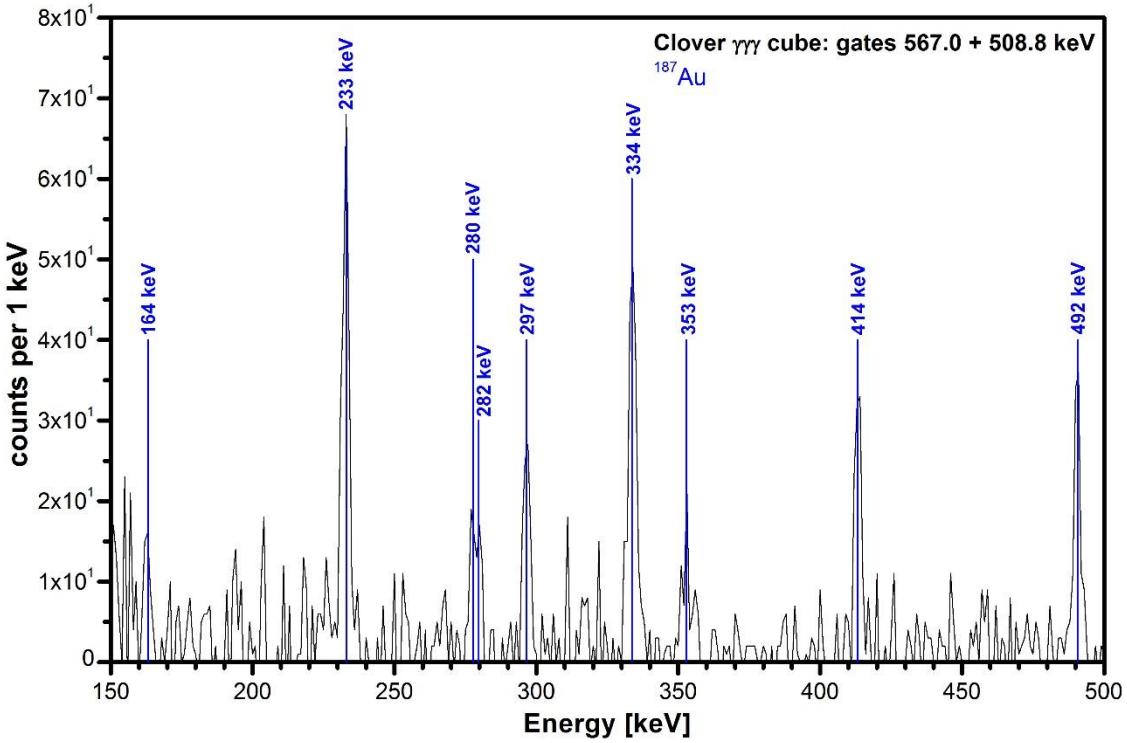

Figure 3.8: Energy spectrum gated at both 567.0 keV and 508.8 keV.

3.1.2 *Band 2*, *3* and *5*

Other bands that side-feed the main band are *Band 2*, *3* and *5*. Spectra containing transitions from *Band 2* can be seen in Fig. 3.9 and 3.10. In the latter, it can be observed that the 462.0 keV transition has a higher intensity than the 318.9 keV (intensity is proportional to the peak height). Both transitions depopulate the $15/2^-$ state, which means that the 462.0 keV transition feeds the major part of the *Band 2* intensity into *Band 1*. This can be clearly seen in the level scheme (see Fig. 3.1). The same situation occurs in *Band 3* with 564.3 keV and 258.8 keV at the $17/2^-$ state (See Fig. 3.11). The 334.7 keV transition from *Band 1* is observed in Fig. 3.10, which suggests a transition from the $15/2^-$ state in *Band 1* to the $17/2^-$ state in *Band* 2. The transition, with an expected energy of around 127 keV, was not observed in γ-γ or γ-γ-γ data. Fig. 3.14 shows the spectrum gated at both 376.7 keV and 318.9 keV transitions from *Band 2*. The band-head of *Band 3* has a spin of $13/2^+$ and is located at 1122 keV. The $13/2^+$ state corresponds to a $1i_{13/2}$ orbital proton coupled with an even-even $_{78}$Pt core (see Fig. 1.2). Like the $9/2^-$ state in *Band 1*, the $13/2^+$ is also an intruder state. *Band 3* contains a doublet consisting of 469.9 keV and 471.8 keV transitions. Both transitions can be seen in Fig. 3.11 together with another doublet from transitions that cross bands, 462.0 keV

and 464.7 keV. Fig. 3.12, spectrum gated at 471.8 keV, confirms that the transitions are in coincidence. As does Fig. 3.16, where the spectrum is gated at both transitions. *Band 5* has a high-spin band head and side-feeds bands 1 and 2. It also contains a doublet with 552.4 keV and 554.3 keV. Fig. 3.13 shows the transitions in coincidence with the former transition.

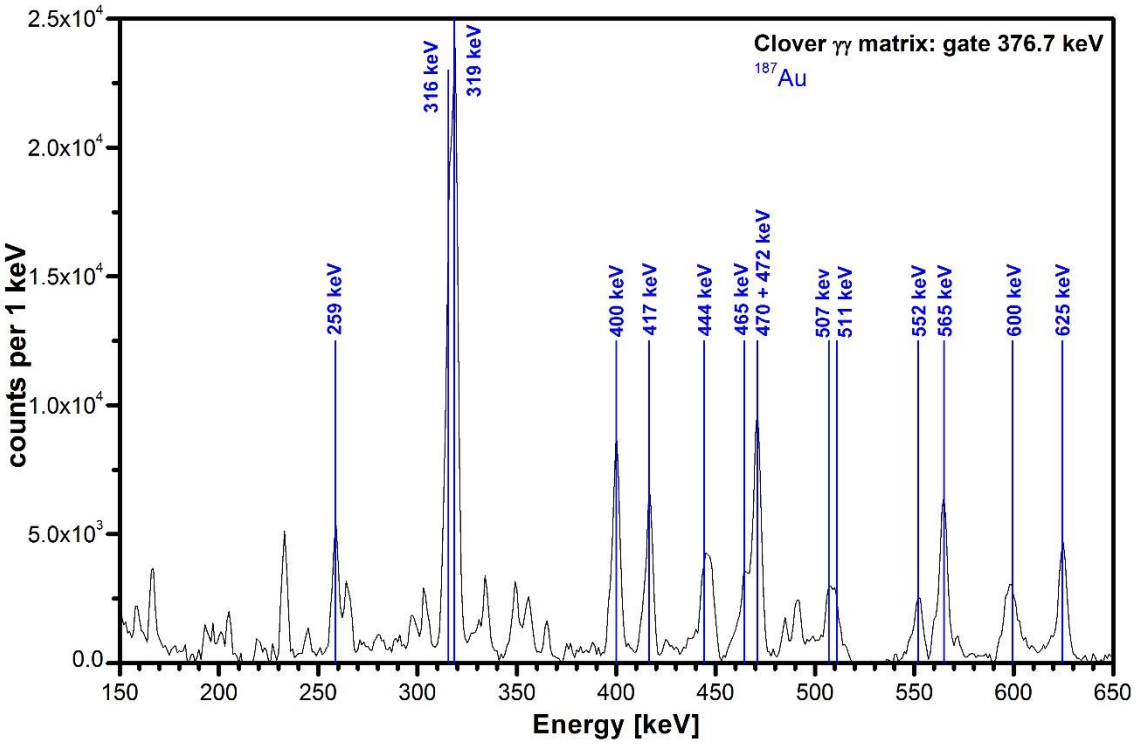

Figure 3.9: Energy spectrum gated at 376.7 keV.

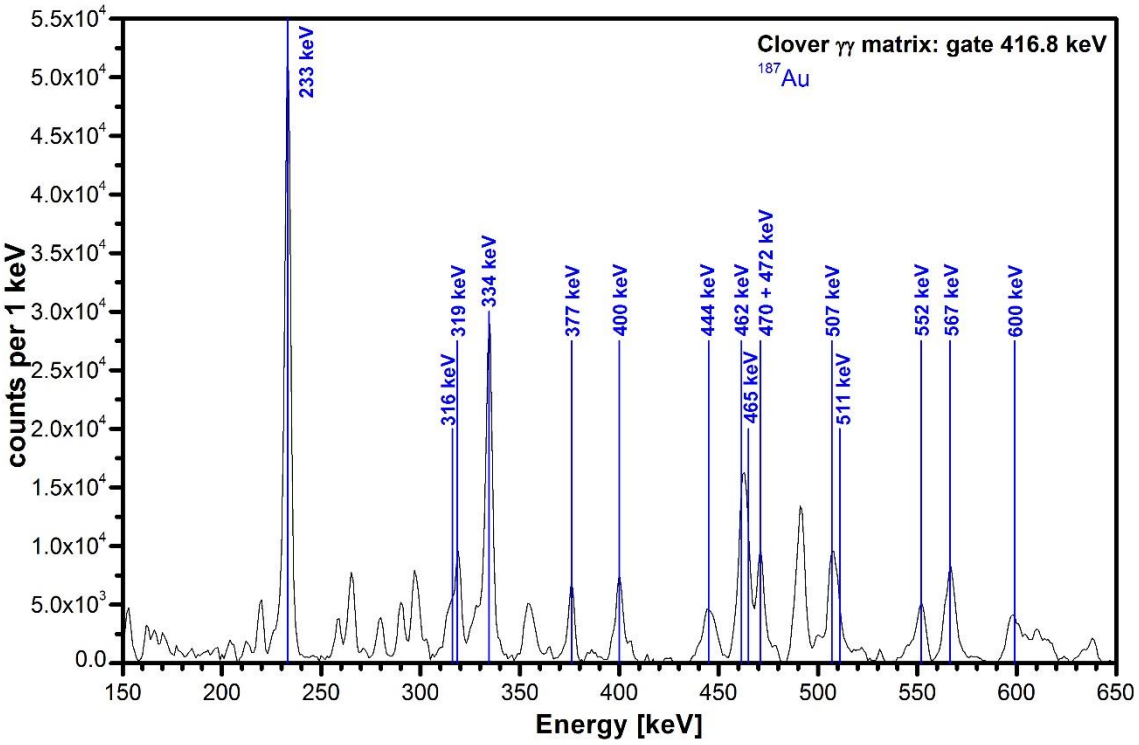

Figure 3.10: Energy spectrum gated at 416.8 keV.

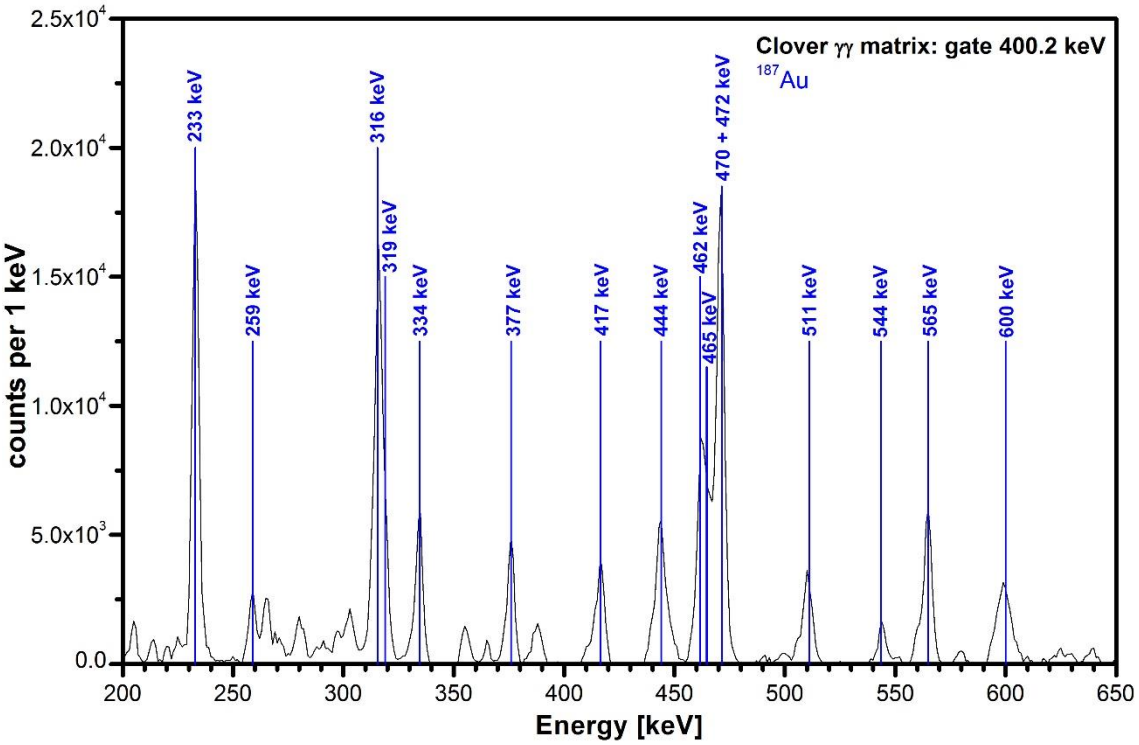

Figure 3.11: Energy spectrum gated at 400.2 keV.

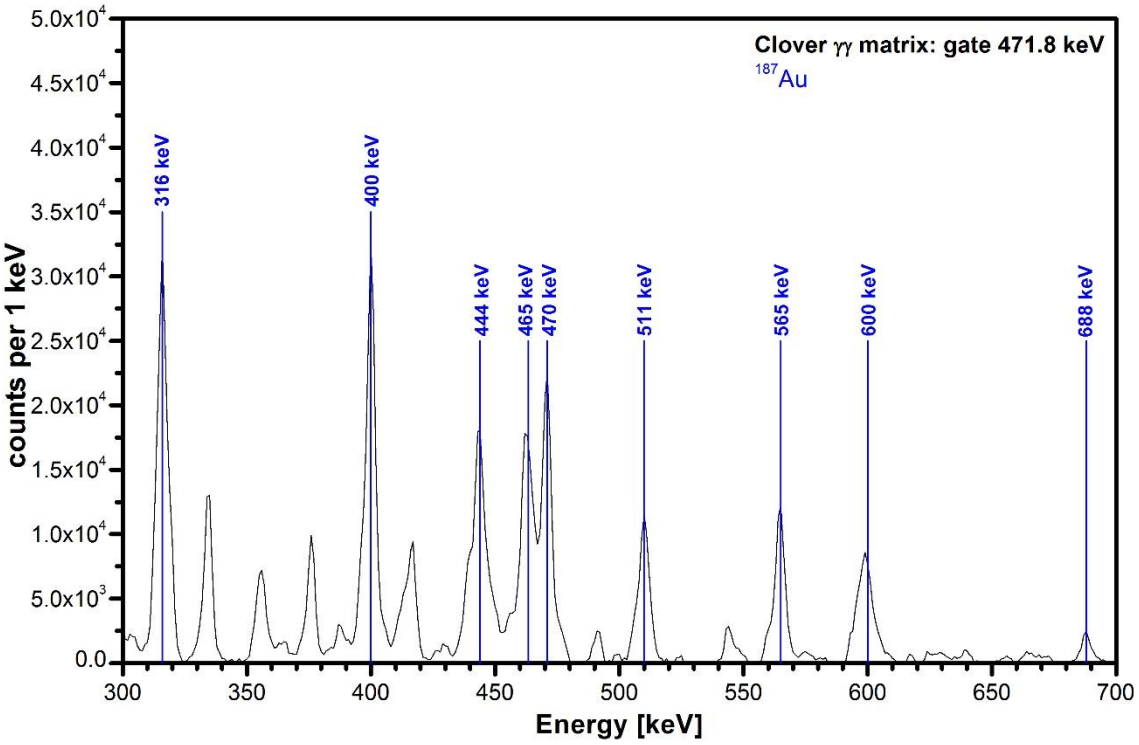

Figure 3.12: Energy spectrum gated at 471.8 keV.

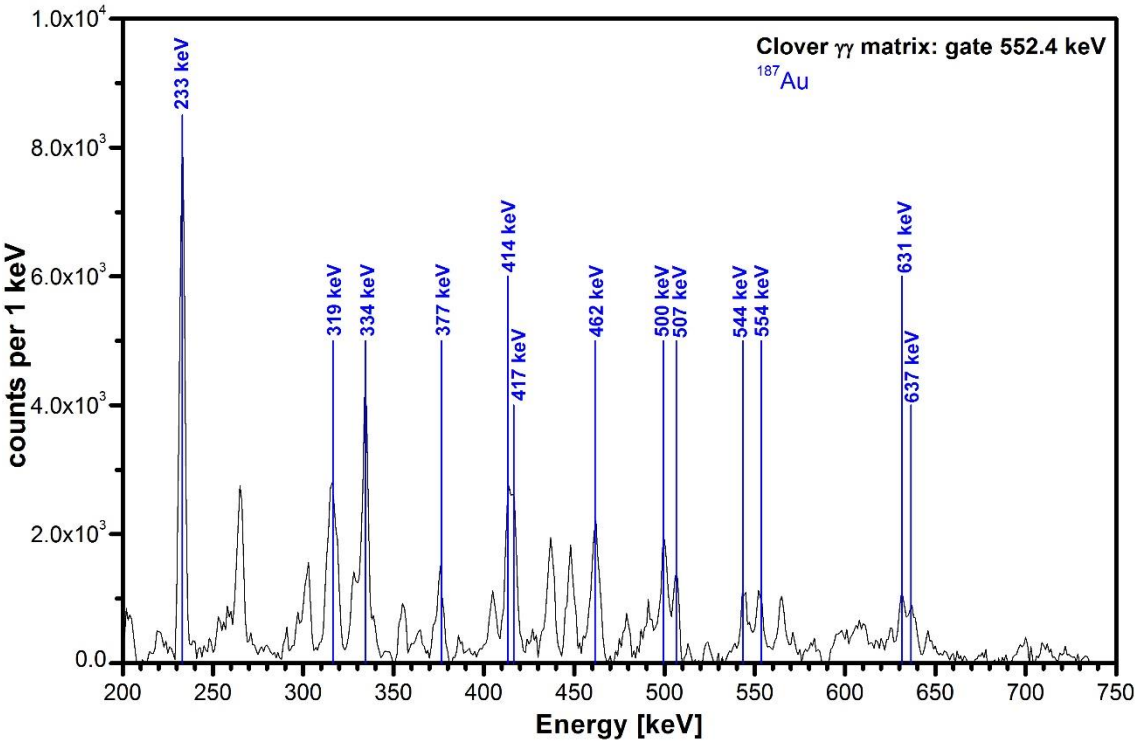

Figure 3.13: Energy spectrum gated at 552.4 keV.

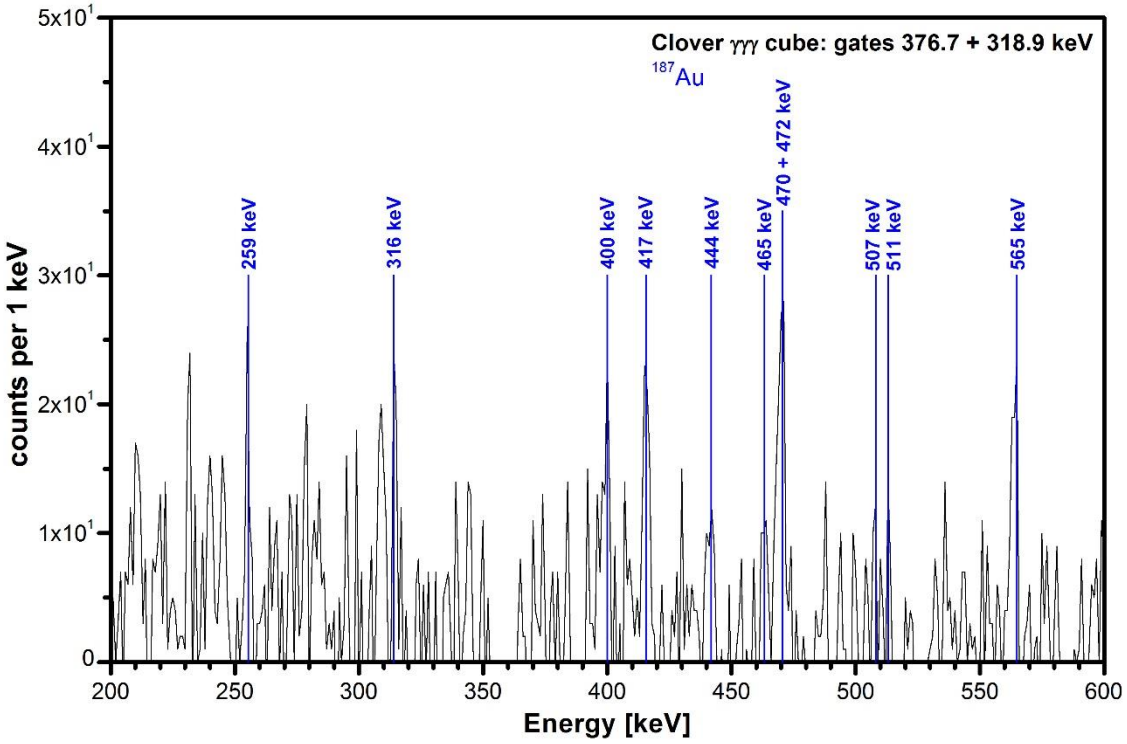

Figure 3.14: Energy spectrum gated at both 376.7 keV and 318.9 keV.

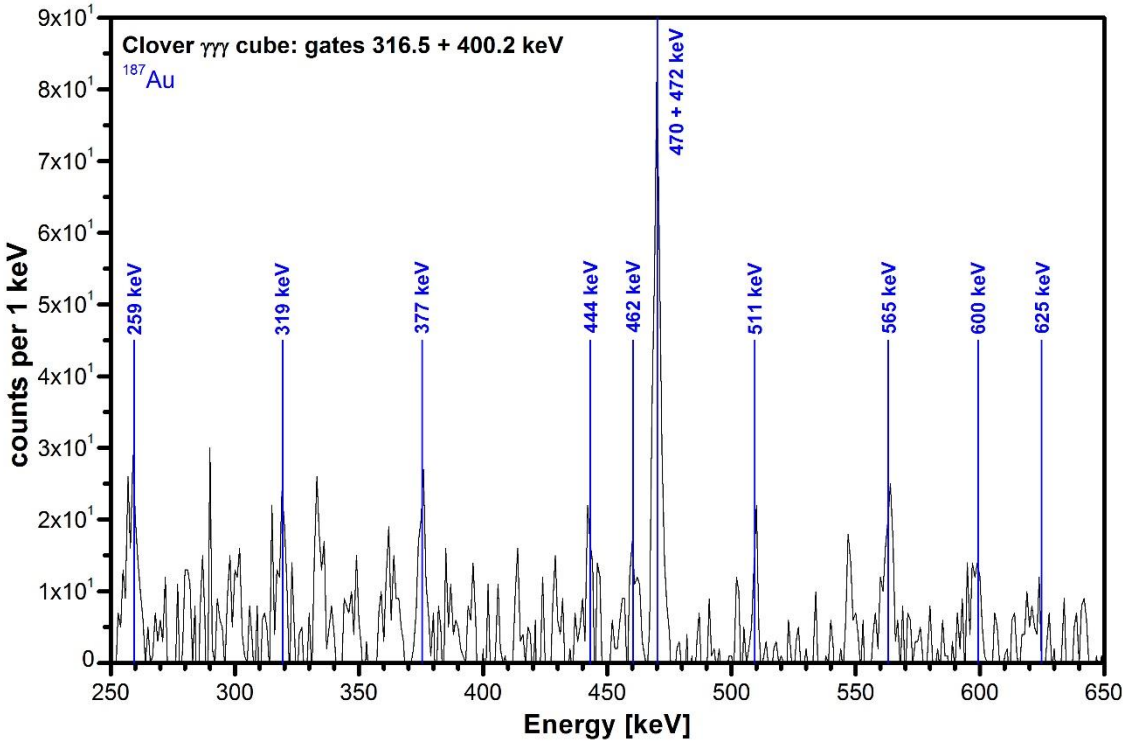

Figure 3.15: Energy spectrum gated at both 316.5 keV and 400.2 keV.

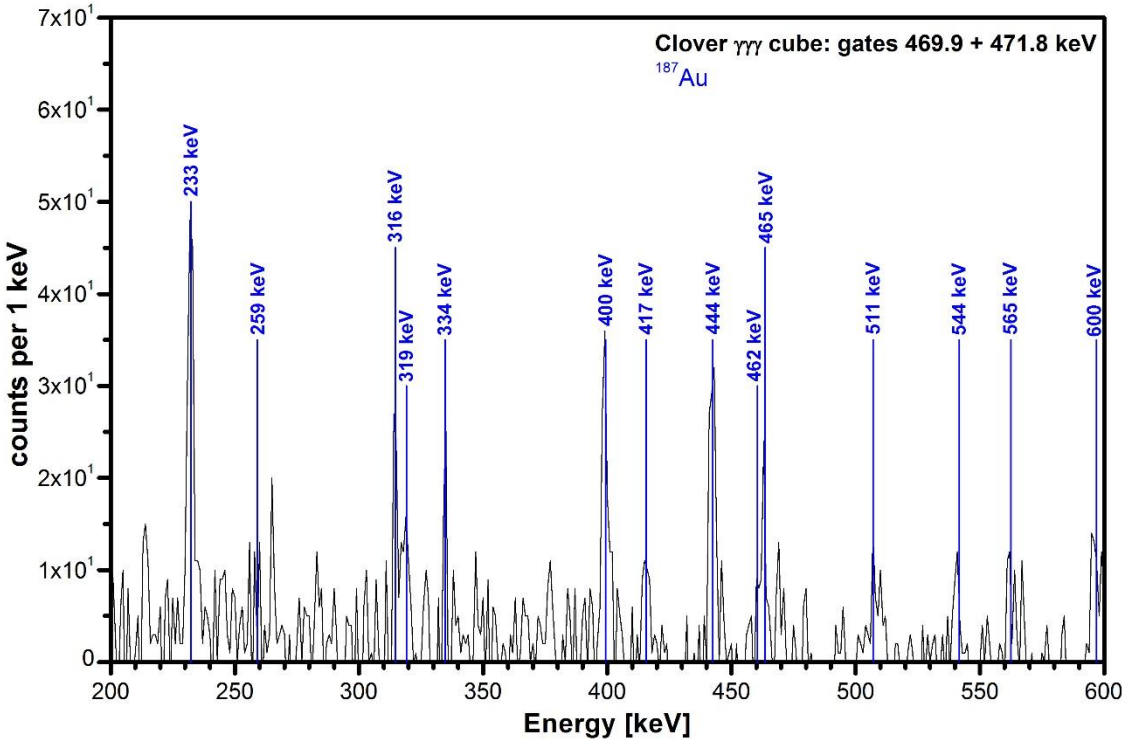

Figure 3.16: Energy spectrum gated at both 469.9 keV and 471.8 keV.

3.1.3 *Bands 6 - 9*

The band-head of *Band 6* has a spin of $11/2^-$ and lies at 224 keV. The state is isomeric, with a half-live of 48 nanoseconds [58], and decays via a 103.6 keV M1 + E2 transition to the $9/2^-$ state of *Band 1*. The $11//2^-$ state corresponds to a $1h_{11/2}$ orbital hole coupled with an even-even $_{80}$Hg core. The 449.4 keV transition is one of the most intensive in the level scheme. *Band 7* side-feeds *Band 6* by populating the $19//2^-$ state with a 709.7 keV E1 transition. Fig. 3.17 – 3.19 show the transitions of the two bands. The last two bands have been previously observed in the in-beam measurements in [7], but not in [6]. This is strange, since the production reaction of ^{187}Au was the same. In the present study, we can see these transitions, albeit with lower intensities than in other observed bands.

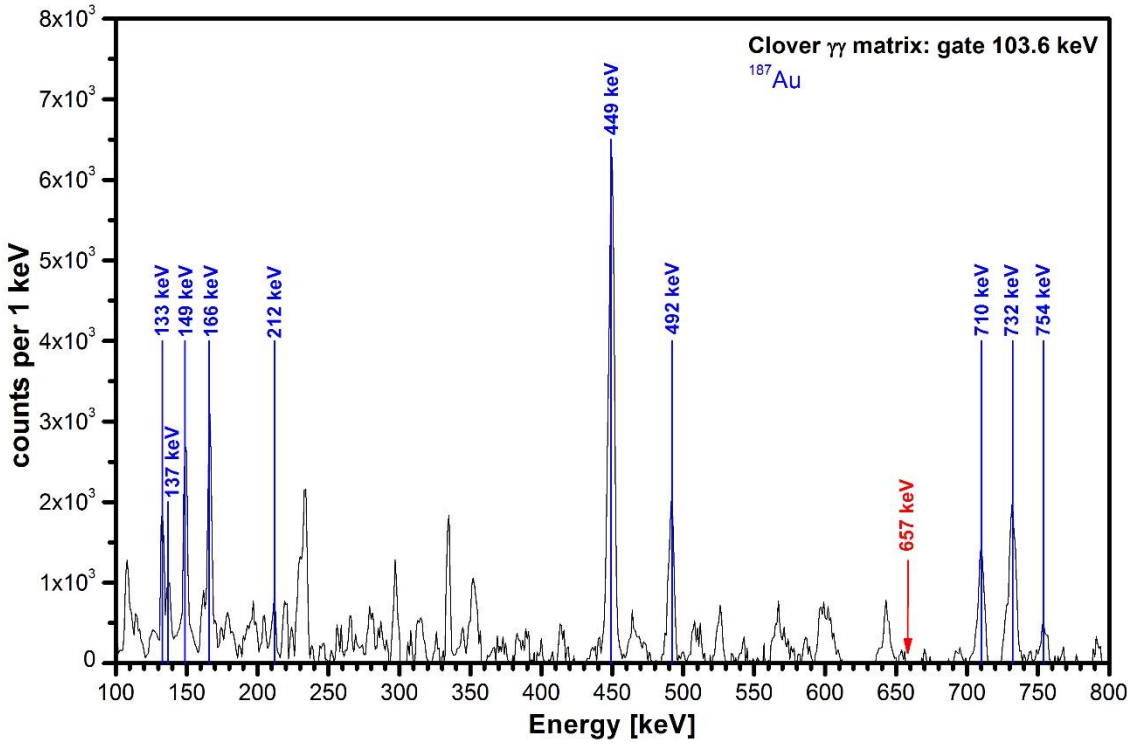

Figure 3.17: Energy spectrum gated at 103.6 keV.

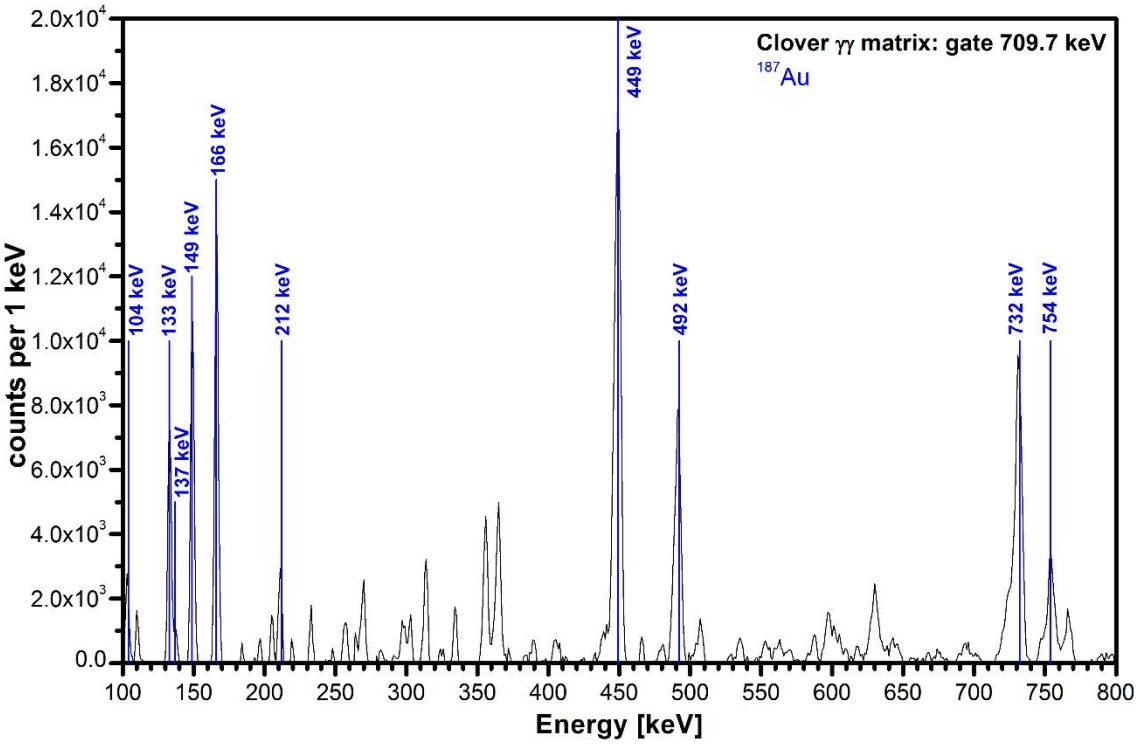

Figure 3.18: Energy spectrum gated at 709.7 keV.

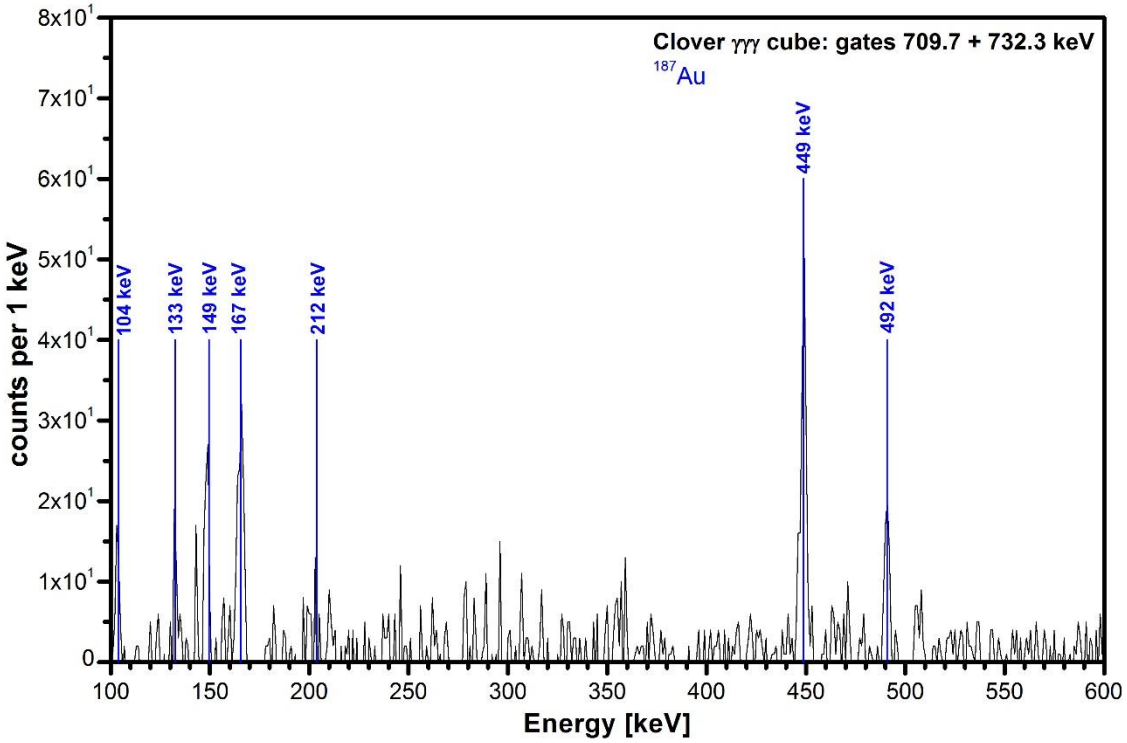

Figure 3.19: Energy spectrum gated at both 709.7 keV and 732.3 keV.

The placement and order of the individual transitions in the bands was based on intensity calculations from RadWare. The scheme itself is constructed from the Clover γ-γ matrix data in *ESCL8R*, but correction have also been made based on γ-γ-γ cube data. As can be seen, the double gated spectra have lower count rates, but are much more accurate since a lot of contaminations and statistical coincidences have been eliminated. The decrease in the count rate from γ-γ to γ-γ-γ spectrum is approximately 10^3. Therefore, some low-intensity transitions might have been lost in the γ-γ-γ data. Another, before mentioned, problem was the constant presence of transitions from contaminations. These transitions have in many cases very similar energies to the ones in ^{187}Au (some examples will be mentioned in chapter 3.2), which complicates the intensity calculations and subsequently the order and placement of the transitions. This was the case in almost all ^{187}Au bands, but more notably in *Bands 7-9*, because their transitions have mostly lower intensities. The other problem with the placement of new transitions was the fact that the most intensive transitions were often visible in gated spectra, where we knew they do not belong. An example is in the Fig. 3.17, where transitions 233.7 keV and 334.7 keV can be seen. The gate in this spectrum is set at

103.6 keV, which is not in coincidence with the listed transitions (see level scheme in Fig. 3.1 and 3.2). These occurrences led in quite a few cases to an unsuccessful search for other transitions in coincidence.

To solve some difficulties in transition assignments, we used the γ-γ matrix data from LEPS detectors. Since LEPS detectors have a high efficiency for lower energies, their spectra were used to resolve low lying transitions. Fig. 3.20 shows such a LEPS spectrum, gated at 103.6 keV. We can see that transitions above 300 keV have lower intensities than the same spectrum for Clover detectors in Fig. 3.17. We used the LEPS data also to observe the characteristic X-rays, which proved valuable in determining the contaminating isotopes in the data. Fig. 3.21 shows the characteristic X-rays of gold (Kα1, Kα2 and Kβ1), that were observed in coincidence with the 449.4 keV transition from *Band 6*.

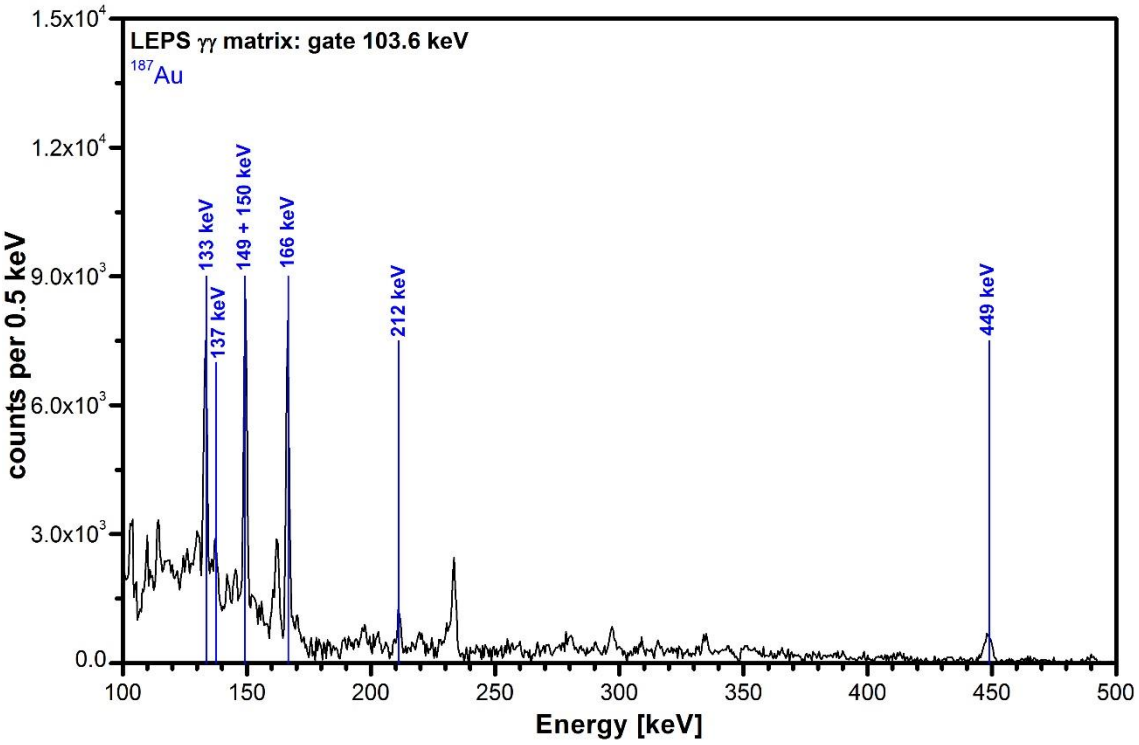

Figure 3.20: LEPS energy spectrum gated at 103.6 keV.

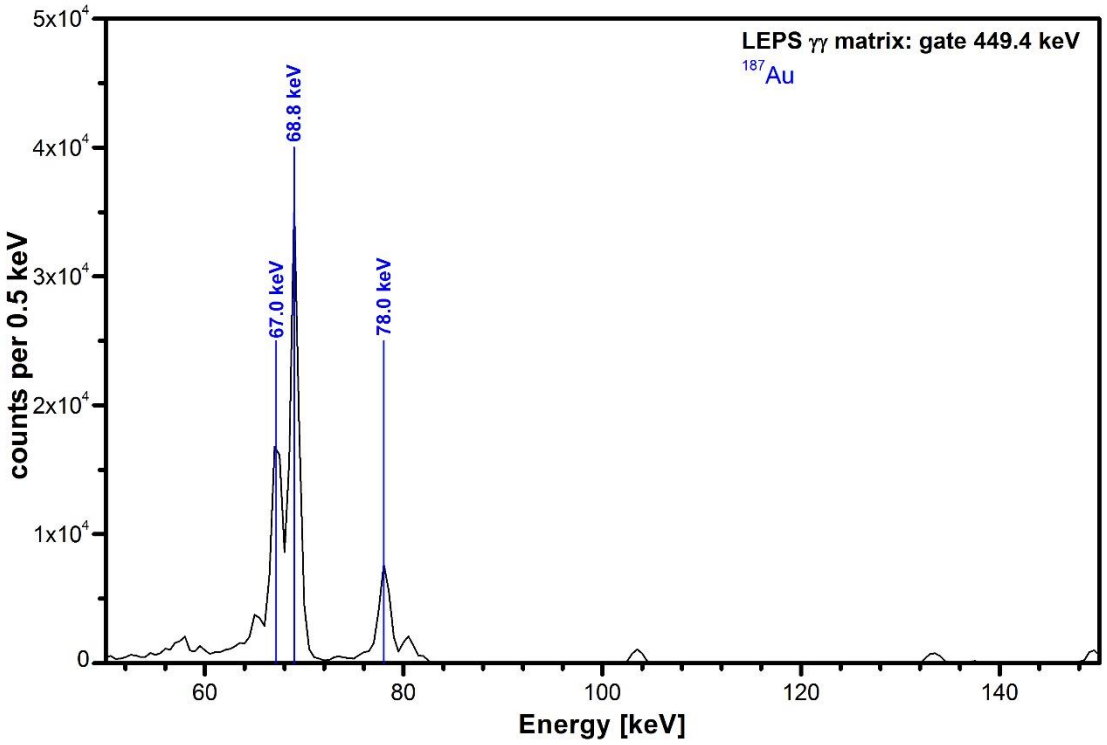

Figure 3.21: LEPS energy spectrum gated at 449.4 keV.

3.1.4 Rotational bands and Intruder states

The purpose and the main goal of the experiment PR235, mentioned in chapter 2.4., was the identification of rotational band structures built upon *intruder states*. No such transitions were observed in our data. These expected (or predicted) transitions could have been obscured by the contaminants present in our data or simply they are not present. One example is the $11/2^-$ intruder state identified in the beta-decay study [4], seen in Fig. 2.6 and 3.22 [59]. The transition was not visible in the singles data and when gated (see Fig. 3.23), there are no new transitions present, only the most intensive transitions from our data, that are at some level visible all the time because of accidental coincidences. From the coincidences seen in Fig. 3.23, the 657 keV transitions would more likely be a part of ^{188}Au. Looking at Fig. 3.2 and 3.22, the 657 keV transition would have to be in coincidence with a 104 keV and a 306 keV transition, which are not seen in Fig. 3.23. Furthermore, the 657 keV transition is very clearly not present in Fig. 3.17, a spectrum gated on 104 keV. The conclusion is that we observed no evidence of this transition and it is not present in our data. Furthermore, looking at the systematics

in odd-mass Au isotopes in Fig 3.22, we can see that there are differences in how the pair of $11/2^-$ states behave in ^{177}Au and ^{187}Au. In ^{177}Au, they are not directly connected by an E0 transition, but the decay proceeds through other states [59]. Taking this into account, the structure of the band in ^{187}Au has to be very different from the one in ^{177}Au seen in Fig. 3.22, e.g. a band with very high spin and energy that we could not populate in our experiment.

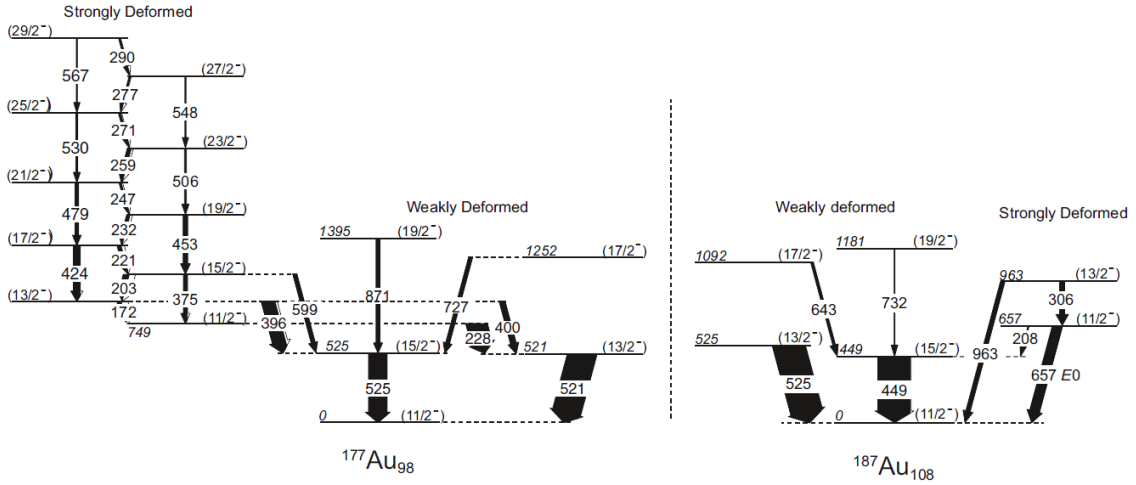

Figure 3.22: $11/2^-$ intruder state configurations in ^{177}Au and ^{187}Au, taken from [59].

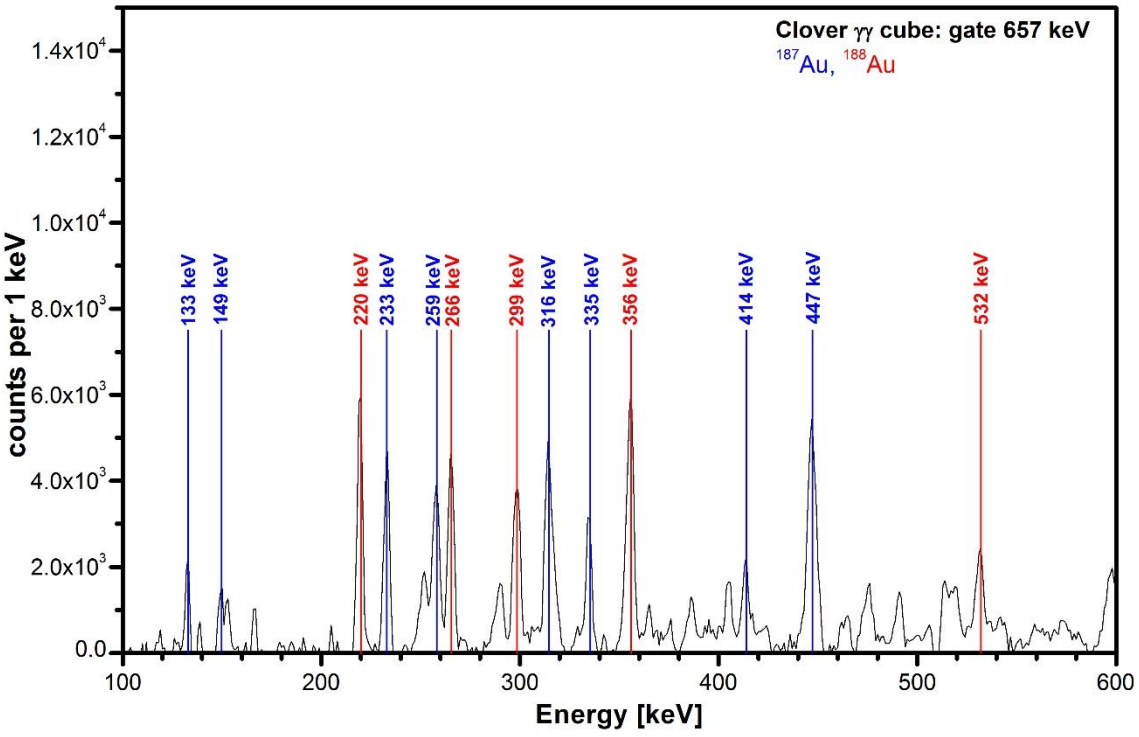

Figure 3.23: Energy spectrum gated at 657 keV.

3.1.5 Polarization measurements and R_{DCO}

By calculating the R_{DCO} for ^{187}Au in our data, we aimed to confirm, or expand, the knowledge on the multipolarities of the transitions that were assigned in the previous studies, especially the in the in-beam gamma-ray spectroscopy experiments [6, 7]. For R_{DCO} calculation, using equation 2.7, the detector efficiencies at different angles had to be defined. The AFRODITE array has three different angles at which the detectors can be positioned, see chapter 2.3.1. For Clover detectors, we marked the positions as Ring 1 and Ring 2, corresponding to 135° and 90°. Detector efficiencies were obtained by EFFIT (see chapter 2.5.2). Fig. 3.24 shows the fit of the efficiency calibration curve for Ring 2.

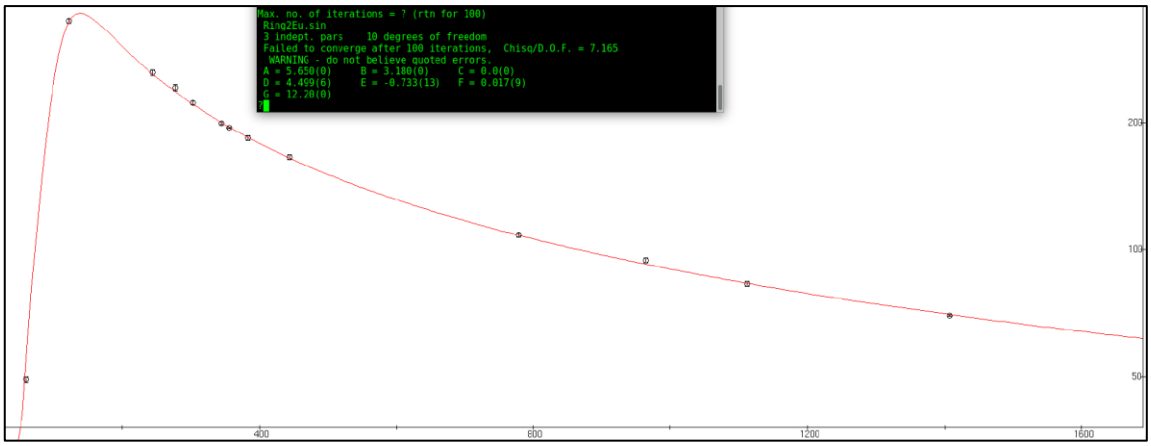

Figure 3.24: Efficiency fit of Ring 2 of AFRODITE.

	A	B	C	D	E	F	G
Ring 1	6	2.9	0	4.709	-0.757	0.014	15
Ring 2	5.65	3.18	0	4.501	-0.725	0.022	12.2

Table 3.2: Efficiency equation parameters obtained by EFFIT for the AFRODITE Clover detectors.

Data from ^{152}Eu and ^{133}Ba calibration sources were used for calibrating the efficiency curve, Tab. 3.2 lists the final parameters for equation 3.1. The final calculations of R_{DCO} for *Band 1* is listed in Tab. 3.3. Since the intensity of the same transition measured in

different angles depends only on the peak area and the detector efficiency, equation 2.7 can be written as:

$$R_{DCO} = \frac{Ring\ 2\ eff}{Ring\ 1\ eff} * \frac{Ring\ 1\ area}{Ring\ 2\ area} \tag{3.2}$$

transition [keV]	Ring 1 area	Ring 2 area	Ring 1 eff	Ring 2 eff	R_{DCO}
233.7	1.43E+05	1.21E+05	342.96	269.88	0.93
334.7	4.39E+04	4.36E+04	258.34	204.50	0.80
413.8	3.36E+04	2.99E+04	218.73	173.78	0.89
491.7	5.02E+04	4.08E+04	191.23	152.44	0.98
567.0	3.47E+04	2.98E+04	171.24	136.93	0.93
638.6	2.09E+04	1.52E+04	156.22	125.27	1.10
704.5	5.19E+04	3.82E+04	147.37	120.75	1.11
760.1	1.31E+04	6.60E+03	139.17	114.19	1.63
777.4	1.73E+05	7.07E+04	134.35	108.30	1.98

Table 3.3: R_{DCO} calculations for *Band 1*.

Calculating R_{DCO} for transitions with known multipolarities gives us the value that is associated with this particular multipolarity in the experimental data. In our case, for *Band 1*, all the transitions are E2 [6]. Looking at the most intensive transitions for this band in Tab. 3.3, the R_{DCO} value for E2 transitions should be approximately 0.9 ± 0.1. We can see that the last four transitions do not fit this number. These transitions from *Band 1* are all above the state, where side-feeding from *Band 4* occurs. This could influence the values, but it would not explain the large differences between them. From the used equation, it is certain, that the peak areas have the biggest effect on the outcoming values. This is where the presence of the contaminations can have an effect once again, by affecting the fit of the peak area. Because of this, higher transitions had to be gated at different transitions, for us to be able to fit the area cleanly. Since the contaminants are more present at lower energies, it is possible that the higher value for R_{DCO} is actually more precise. We tried to calculate some other values for known E2 transitions form *Band 2* and *3*, but there was a similar dispersion present.

3.2 Contaminations

As mentioned several times in the experimental results of ^{187}Au, the biggest problem encountered in our data were contaminating transitions from other isotopes that were also created in the fusion-evaporation reaction and the subsequent de-excitation and decay. Several of these contaminants have been identified, some with a very high count rate and intensity of transitions. To calculate the intensities of the ^{187}Au transitions with RadWare, all the transitions from these contaminants had to be identified and appropriately placed in their respective level schemes. This chapter will list the identified contaminants in our data.

The most abundant contaminant is the ^{188}Au isotope. The level scheme of the isotope is shown in Fig. 3.25 and Tab. 3.4 contains information on the transitions in the scheme (relative intensities I_γ are normalized with the 447.3 keV transition). The transitions in this level scheme were not so thoroughly evaluated as in the studied ^{187}Au. We did not necessarily try to find new transitions, the scheme was built on previous in-beam data of ^{188}Au [60]. The energy of the 11^- state is not known [60], the energy of the state has been set to 20 keV in our level scheme. Looking at the level scheme, we notice that many transitions have high intensities that match those of ^{187}Au. The two most intensive transitions from ^{187}Au in the spectrum had intensities only few percent higher than the two most intensive transitions in ^{188}Au. Fig. 3.26 and 3.27 show the spectrum gated at 447.3 keV, the most intensive transition of ^{188}Au. The observed transitions in coincidence are very clear. Even in γ-γ-γ data, ^{188}Au is still observed in high intensities (see Fig. 3.28). The conclusion on the presence on ^{188}Au is, that its intensity and abundance is very nearly on the same level as the studied ^{187}Au, which makes it extremely difficult to make a new observation in the data and declare that it is part of ^{187}Au. Another problem is the fact, that the contaminant is an isotope of the same chemical element, gold. To get rid of the contaminations, we tried to sort the data in our program by gating the characteristic X-ray of gold, 68.8 keV. This attempt was unsuccessful because of the presence of ^{188}Au. Furthermore, some transitions in ^{188}Au have very similar energies to the ones in ^{187}Au. Some examples (listed for ^{187}Au first) are 133.6 keV and 132.9 keV, 508.8 keV and 509.0 keV, 732.3 keV and 731.8 keV. Fig. 3.29 shows the spectrum gated at 731.8 keV, where transitions from both gold isotopes are clearly observed.

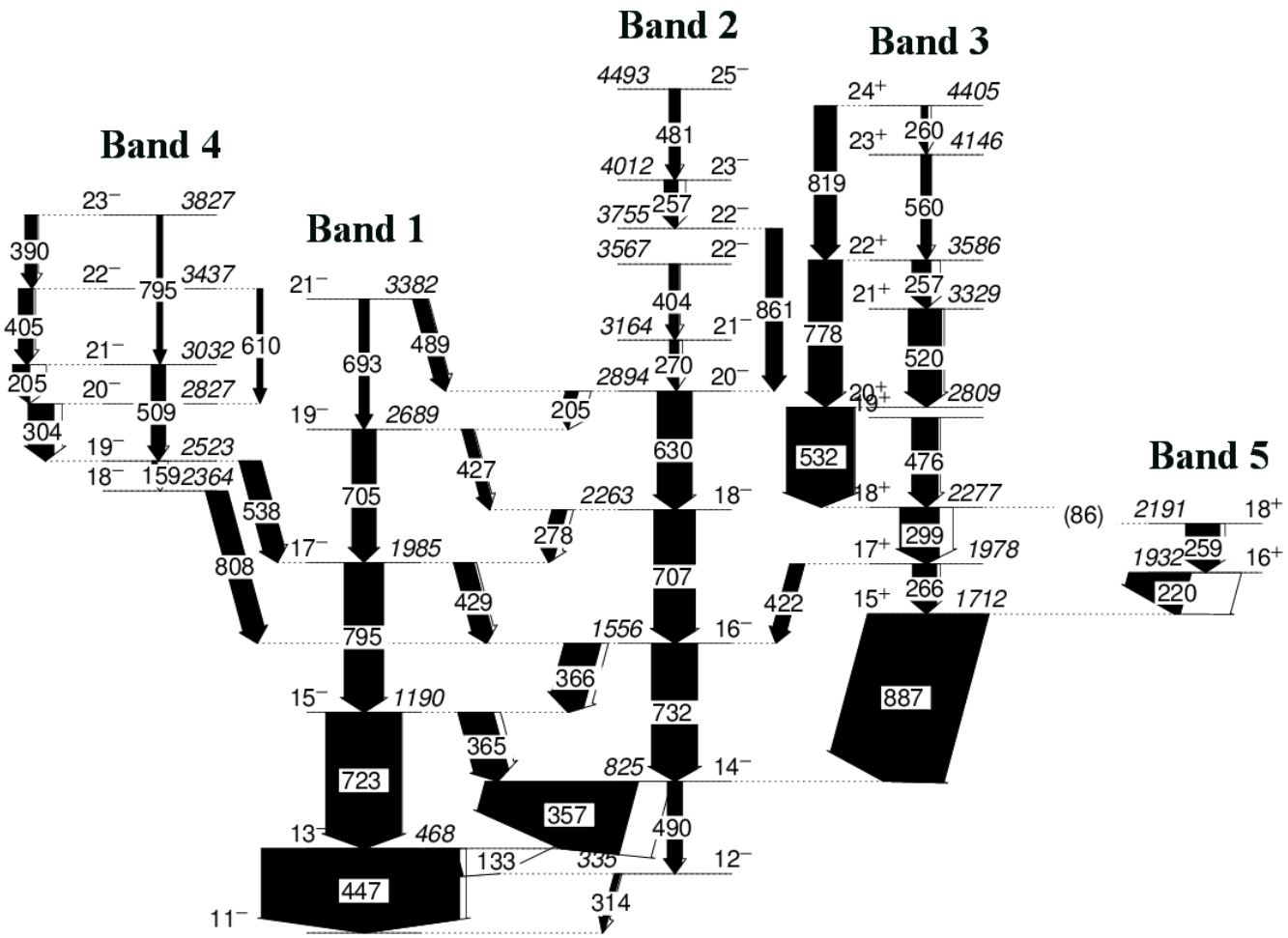

Figure 3.25: Level scheme of ^{188}Au, constructed from our experimental data.

E_γ [keV]	I_γ [%]	E_i [keV]	α	I_i^π	I_f^π
Band 1					
132.89(6)	22(2)	447.3	3.34E+00	13^-	12^-
365.39(7)	17(1)	1169.8	2.02E-01	15^-	14^-
426.7(1)	5.4(8)	2668.7	1.34E-01	19^-	18^-
429.10(9)	9.9(9)	1964.4	1.32E-01	17^-	16^-
477.30(1)	100(11)	447.3	3.44E-02	13^-	11^-
488.6(1)	7.1(9)	3361.7	9.33E-02	21^-	20^-
693.2(2)	4.9(8)	3361.7	1.23E-02	21^-	19^-
704.79(8)	12(1)	2668.7	1.19E-02	19^-	17^-
722.57(5)	38(3)	1169.8	1.13E-02	15^-	13^-
794.50(5)	20(1)	1964.4	9.24E-03	17^-	15^-
Band 2					
205.1(1)	6.3(7)	2872.9	9.83E-01	20^-	19^-
257.0(1)	6.9(6)	3990.9	5.26E-01	23^-	22^-
270.0(1)	4.6(7)	3142.9	4.59E-01	21^-	20^-
277.8(1)	7.4(7)	2242.6	4.25E-01	18^-	17^-
314.30(4)	1.7(1)	314.3	3.02E-01	12^-	11^-
356.69(3)	77(4)	804	2.16E-01	14^-	13^-
365.74(6)	18(1)	1535.6	2.02E-01	16^-	15^-
403.8(1)	4.8(7)	3546.7	1.55E-01	22^-	21^-
481.1(1)	5.6(6)	4471.9	2.87E-01	25^-	23^-
489.7(1)	9(1)	804	2.74E-02	14^-	12^-
629.97(7)	18(1)	2872.9	1.52E-02	20^-	18^-
707.01(6)	21(1)	2242.6	1.18E-02	18^-	16^-
731.83(6)	23(2)	1535.6	1.10E-02	16^-	14^-
860.9(1)	8.3(7)	3733.9	7.84E-03	22^-	20^-
Band 3					
86.4(6)	2.0(2)	2256.5	1.15E+01	18^+	18^+
257.29(8)	9.6(7)	3565.7	5.20E-01	22^+	21^+
259.8(1)	3.6(6)	4384.4	5.15E-01	24^+	23^+
265.69(6)	12(1)	1957.1	1.49E-01	17^+	15^+
299.40 (1)	20(1)	2256.5	3.45E-01	18^+	17^+
422.0(1)	7.3(9)	1957.1	1.24E-02	17^+	16^-
519.66(6)	17(1)	3308.1	7.95E-02	21^+	20^+

E_γ [keV]	I_γ [%]	E_i [keV]	α	I_i^π	I_f^π
Band 3	- continued				
531.85(4)	35(2)	2788.3	2.25E-02	20^+	18^+
559.8(1)	5.3(8)	4125.1	6.55E-02	23^+	22^+
777.5(1)	17(1)	3565.7	9.66E-03	22^+	20^+
818.55(7)	11.3(7)	4384.4	8.68E-03	24^+	22^+
887.29(4)	59(3)	1691.3	2.76E-03	15^+	14^+
Band 4					
158.9(1)	2.7(3)	2502.3	2.01E+00	19^-	18^-
205.11(6)	8.7(5)	3011.2	9.83E-01	21^-	20^-
303.83(5)	13.0(7)	2806.1	3.33E-01	20^-	19^-
390.07(9)	5.9(5)	3806	1.70E-01	23^-	22^-
404.72(7)	7.4(6)	3416	1.54E-01	22^-	21^-
509.0(1)	6.9(8)	3011.2	2.50E-02	21^-	19^-
537.88(5)	10.7(8)	2502.3	2.19E-02	19^-	17^-
609.8(2)	2.9(6)	3416	1.64E-02	22^-	20^-
794.8(2)	2.9(5)	3806	9.23E-03	23^-	21^-
807.97(6)	10.9(8)	2343.5	8.93E-03	18^-	16^-
Band 5					
219.99(5)	30(2)	1911.4	8.08E-01	16^+	15^+
258.80(5)	17(1)	2170.2	1.63E-01	18^+	16^+

Table 3.4: Gamma-ray transitions assigned to ^{188}Au.

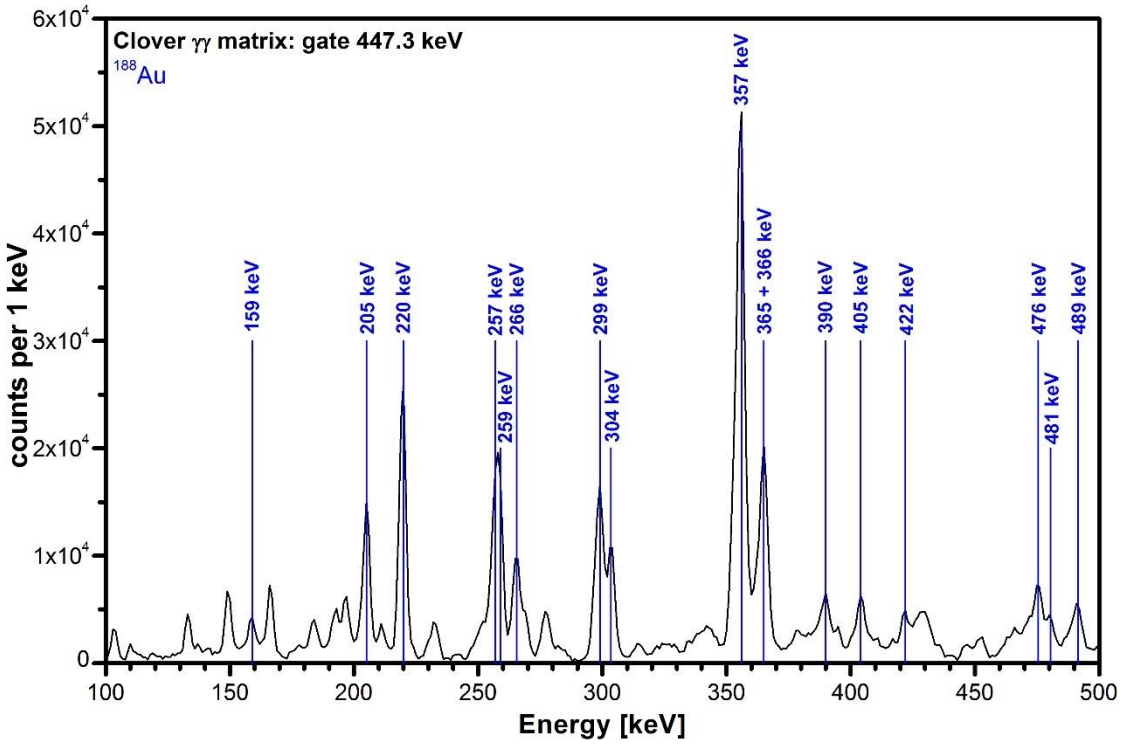

Figure 3.26: Energy spectrum gated at 447.3 keV.

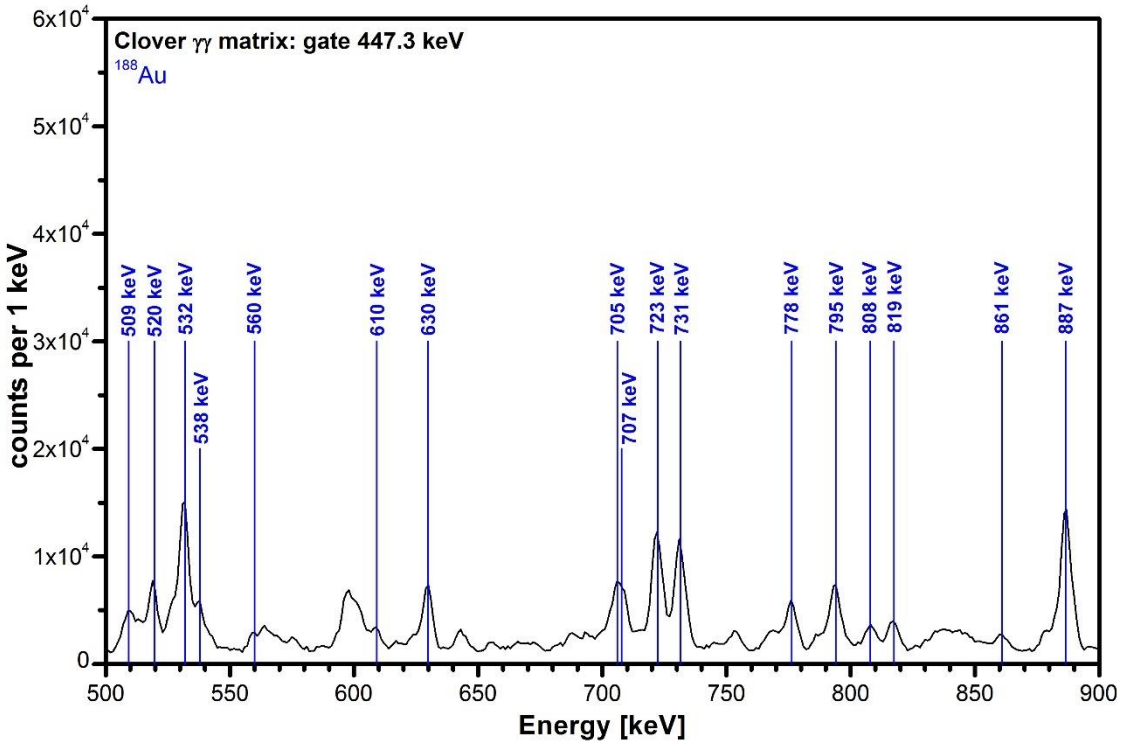

Figure 3.27: Energy spectrum gated at 447.3 keV - continued.

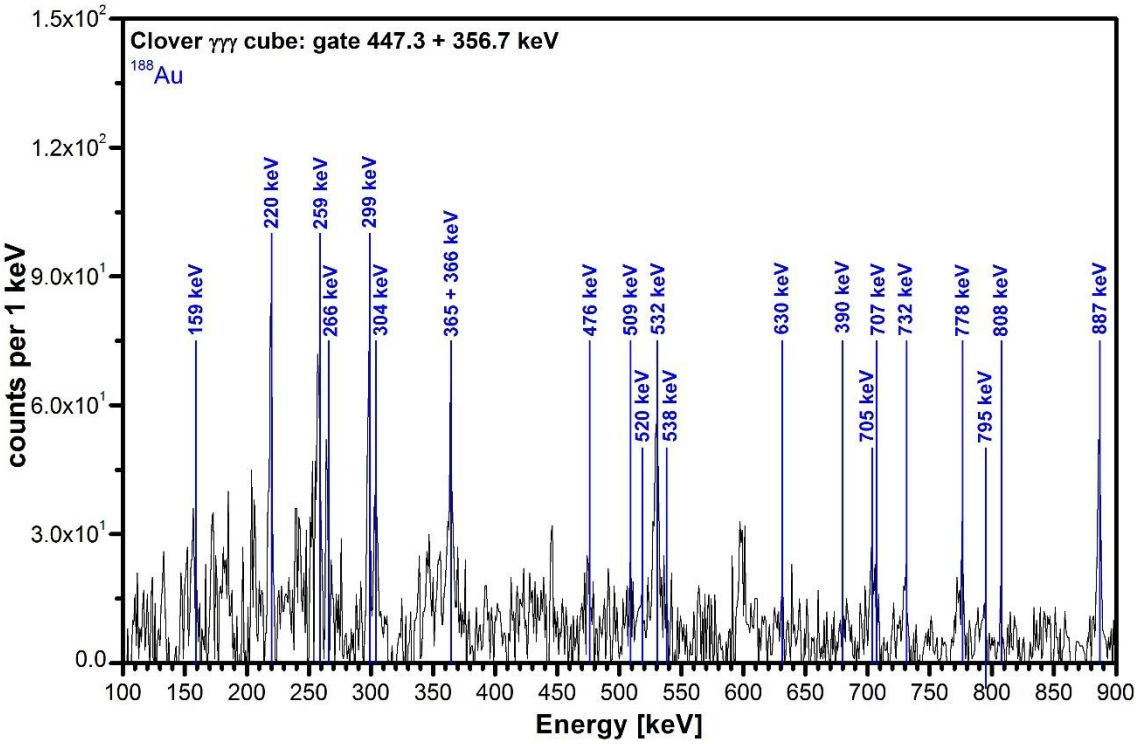

Figure 3.28: Energy spectrum gated at both 447.3 keV and 356.7 keV.

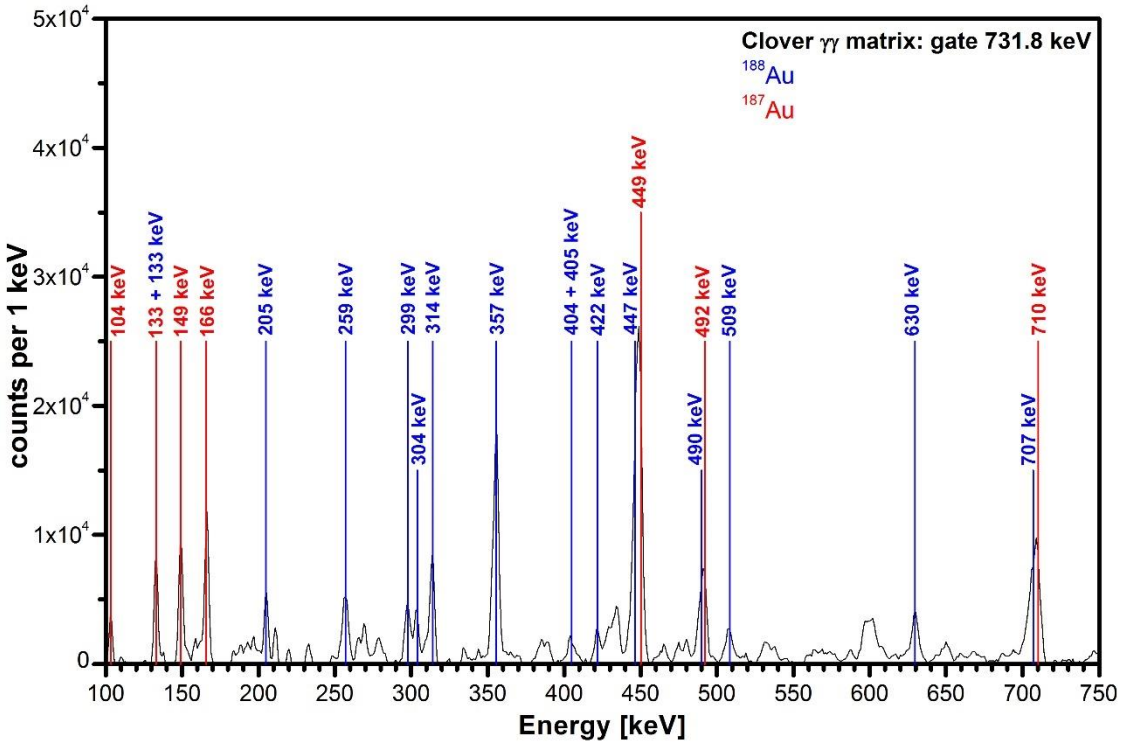

Figure 3.29: Energy spectrum gated at 731.8 keV.

There are two types of contaminants that should be expected in this (and similar) types of data, the chemical elements of the used target and decay products of the studied isotope(s). In our case, that means ^{181}Ta (the target), ^{187}Pt (^{187}Au decay) and ^{188}Pt (^{188}Au decay). All of these contaminations were found in our data. Fig. 3.30 shows the level scheme of ^{181}Ta, where only a few low spin states have been observed. Fig. 3.31 shows that the two lowest transitions (136.4 keV and 165.4 keV) have a very high intensity. Similar transitions are also found in coincidence in *Band 7* in ^{187}Au. Fig. 3.32 shows the X-ray part of the spectrum in LEPS data, where we can clearly see that these transitions are from ^{181}Ta, since the tantalum X-rays are present.

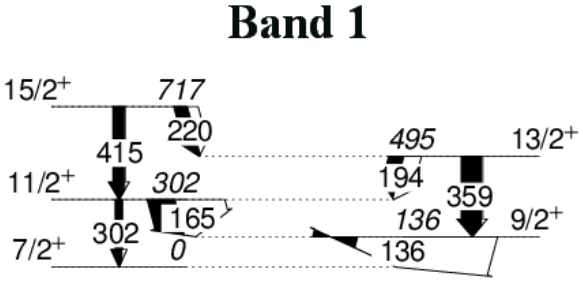

Figure 3.30: Level scheme of ^{181}Ta, constructed from our experimental data.

E_γ [keV]	I_γ [%]	E_i [keV]	α	I_i^π	I_f^π
Band 1					
136.4(6)	100(8)	136.4	3.11E+00	$9/2^+$	$7/2^+$
165.4(2)	62(6)	301.5	1.80E+00	$11/2^+$	$9/2^+$
193.6(2)	34(9)	495.2	1.15E+00	$13/2^+$	$11/2^+$
220.3(5)	30(7)	716.5	7.93E-01	$15/2^+$	$13/2^+$
301.6(6)	15(2)	301.5	1.02E-01	$11/2^+$	$7/2^+$
358.8(3)	47(17)	495.2	6.17E-02	$13/2^+$	$9/2^+$
415(1)	27(14)	716.5	4.17E-02	$15/2^+$	$11/2^+$

Table 3.5: Gamma-ray transitions assigned to ^{181}Ta.

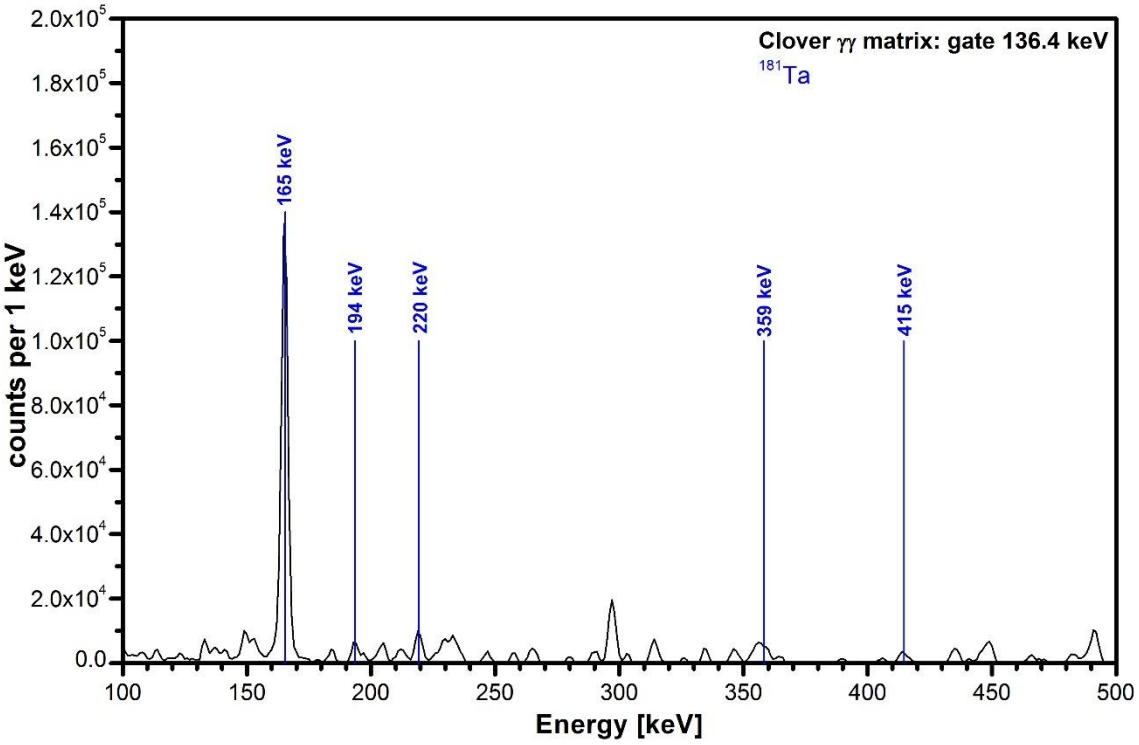

Figure 3.31: Energy spectrum gated at 136.4 keV.

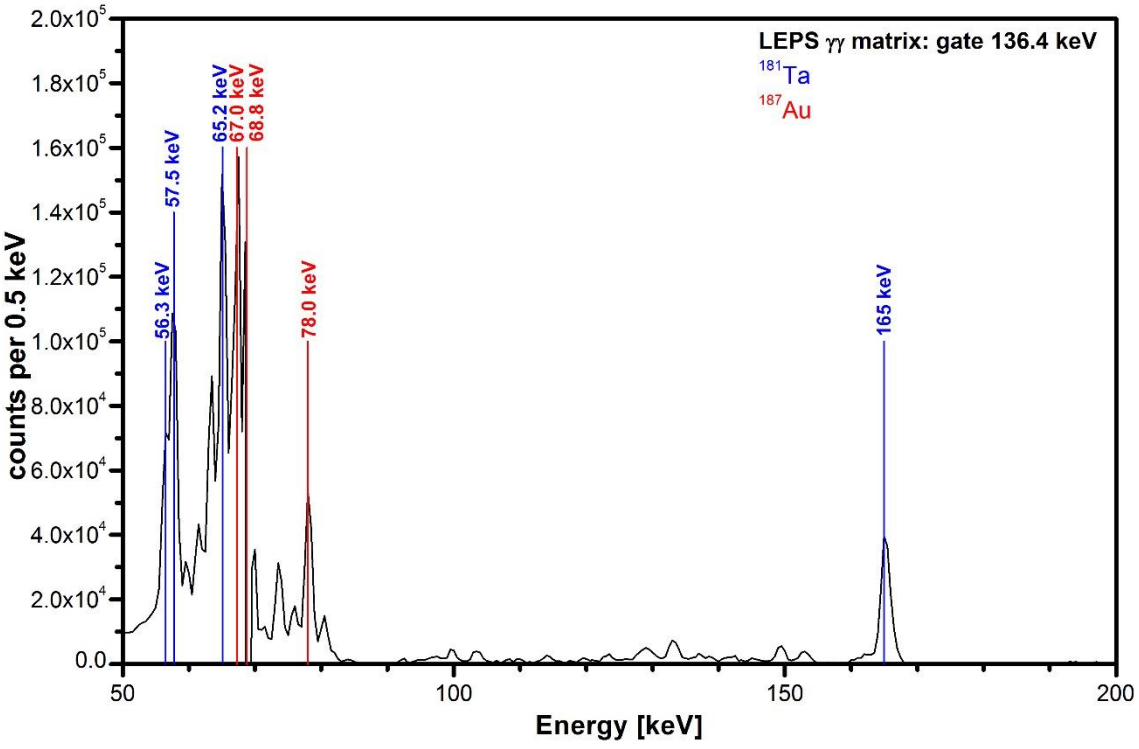

Figure 3.32: LEPS energy spectrum gated at 136.4 keV.

The most abundant contaminant from decay found in the data is ^{188}Pt, coming from the β^+ decay of ^{188}Au. The level scheme is shown in Fig. 3.33 and Tab. 3.6 shows information on the individual transitions (relative intensities I_γ are normalized with the 265.7 keV transition). There are some transitions, that are very similar to ^{187}Au (413.8 keV) and ^{188}Au (265.7 keV) transitions. Fig. 3.34 shows a LEPS spectrum gated at 265.7 keV, where the characteristic X-rays of platinum and gold can be observed together.

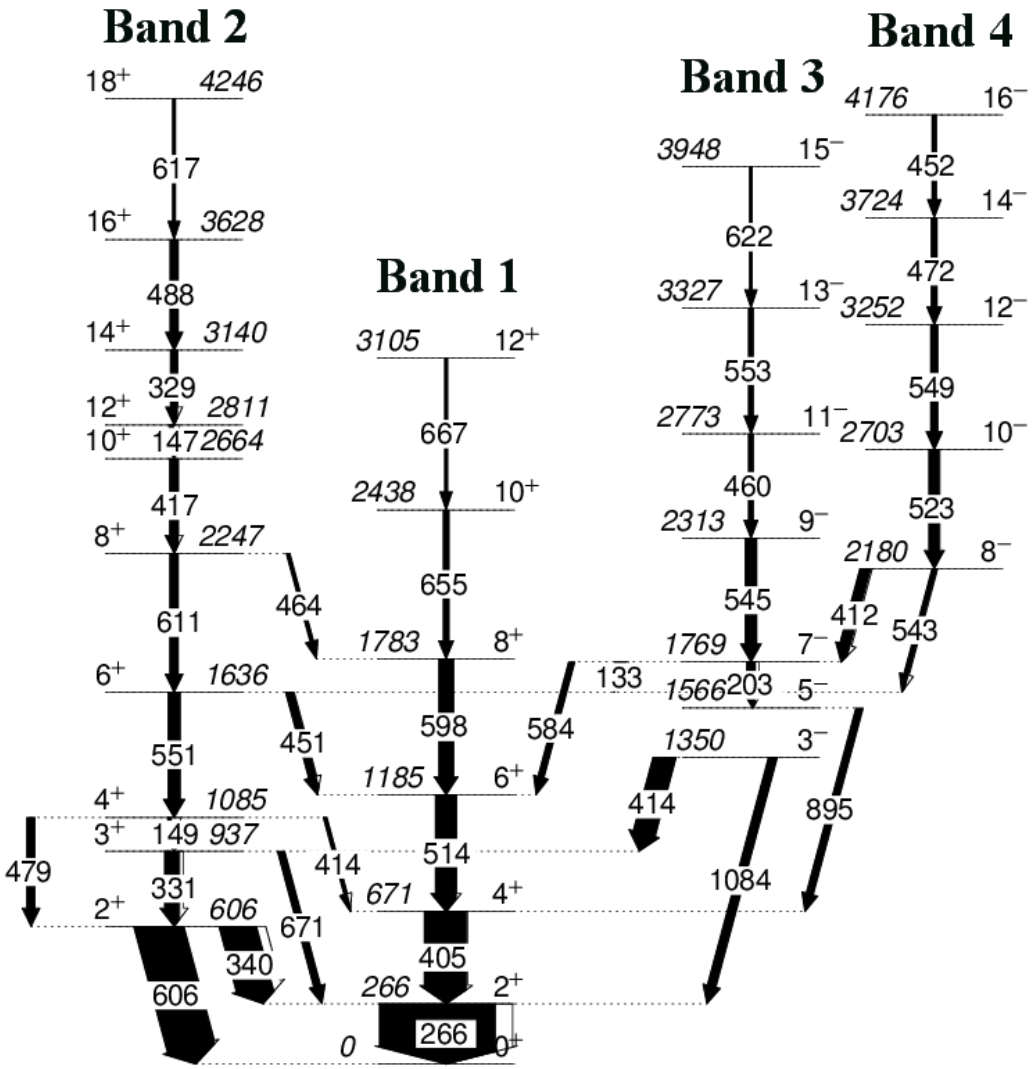

Figure 3.33: Level scheme of ^{188}Pt, constructed from our experimental data.

E_γ [keV]	I_γ [%]	E_i [keV]	α	I_i^π	I_f^π
Band 1					
265.70(4)	100(4)	265.7	1.50E-01	2^+	0^+
405.50(4)	36(2)	671.2	4.43E-02	4^+	2^+
513.62(6)	18(2)	1184.9	2.45E-02	6^+	4^+
598.0(1)	13(2)	1782.8	1.71E-02	8^+	6^+
655.4(1)	5(1)	2438.2	1.40E-02	10^+	8^+
666.9(2)	2.7(8)	3105.1	1.34E-02	12^+	10^+
Band 2					
146.7(1)	3.9(6)	2811.1	1.16E+00	12^+	10^+
148.6(2)	3.3(7)	1085.2	2.43E+00	4^+	3^+
328.89(8)	6.2(6)	3140	7.91E-02	14^+	12^+
330.74(7)	13(1)	936.5	2.65E-01	3^+	2^+
340.20(5)	31(1)	605.9	2.45E-01	2^+	2^+
413.8(4)	2.6(9)	1085.2	1.45E-01	4^+	4^+
417.19(9)	7.4(9)	2664.3	4.11E-02	10^+	8^+
451.2(1)	6.4(7)	1636.2	1.15E-01	6^+	6^+
464.3(2)	2.7(6)	2247.2	1.07E-01	8^+	8^+
479.3(2)	7(1)	1085.2	2.89E-02	4^+	2^+
488.4(1)	6.8(7)	3628.3	2.76E-02	16^+	14^+
550.95(8)	10(1)	1636.2	2.07E-02	6^+	4^+
605.9(1)	41(6)	605.9	1.66E-02	2^+	0^+
617.4(2)	2.5(6)	4245.8	1.59E-02	18^+	16^+
670.9(2)	5.9(9)	936.5	4.10E-02	3^+	2^+
Band 3					
132.55(7)	9.6(8)	1768.7	2.06E-01	7^-	6^+
202.83(6)	7.9(5)	1768.7	3.63E-01	7^-	5^-
413.61(7)	19(1)	1350.1	1.30E-02	3^-	3^+
459.9(1)	4.2(6)	2773.2	3.21E-02	11^-	9^-
544.55(7)	9.6(7)	2313.3	2.13E-02	9^-	7^-
553.4(1)	4.0(5)	3326.6	2.05E-02	13^-	11^-
583.8(1)	5.2(5)	1768.7	6.25E-03	7^-	6^+
621.9(2)	2.4(4)	3948.5	1.57E-02	15^-	13^-
894.88(7)	6.1(5)	1533	2.77E-03	5^-	4^+
1084.22(9)	7.5(6)	1350.1	1.91E-03	3^-	2^+

E_γ [keV]	I_γ [%]	E_i [keV]	α	I_i^π	I_f^π
Band 4					
411.612	8.94	2180	1.47E-01	8^-	7^-
452.014	3.77	4175.7	3.35E-02	16^-	14^-
471.6	4.82	3723.7	3.01E-02	14^-	12^-
523.458	9.36	2703.5	2.34E-02	10^-	8^-
542.687	3.82	2180	2.02E-01	8^-	6^+
548.636	6.16	3252.1	2.09E-02	12^-	10^-

Table 3.6: Gamma-ray transitions assigned to ^{188}Pt.

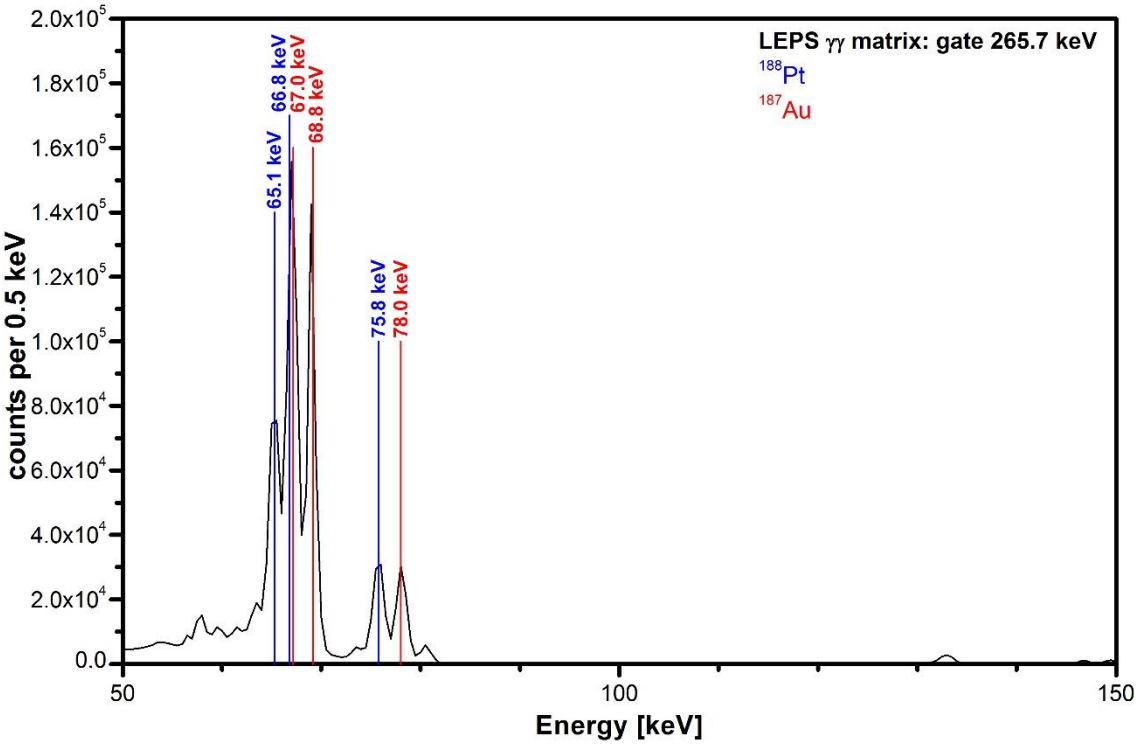

Figure 3.34: LEPS energy spectrum gated at 265.7 keV.

^{187}Pt is the main decay product of ^{187}Au. The transitions of this isotope are not surprisingly present in our data, but their intensities are lower than expected in terms of the contaminants, especially compared to ^{188}Pt. The intensities of ^{187}Pt are an order lower than in ^{188}Pt. Since they are the decay products of the most abundant isotopes in our data, we would expect them to have similarly strong presence and intensive transition. Fig. 3.35 shows the decay scheme of ^{187}Pt and Tab. 3.7 the information on the individual transitions (relative intensities I_γ are normalized with the 302.7 keV transition).

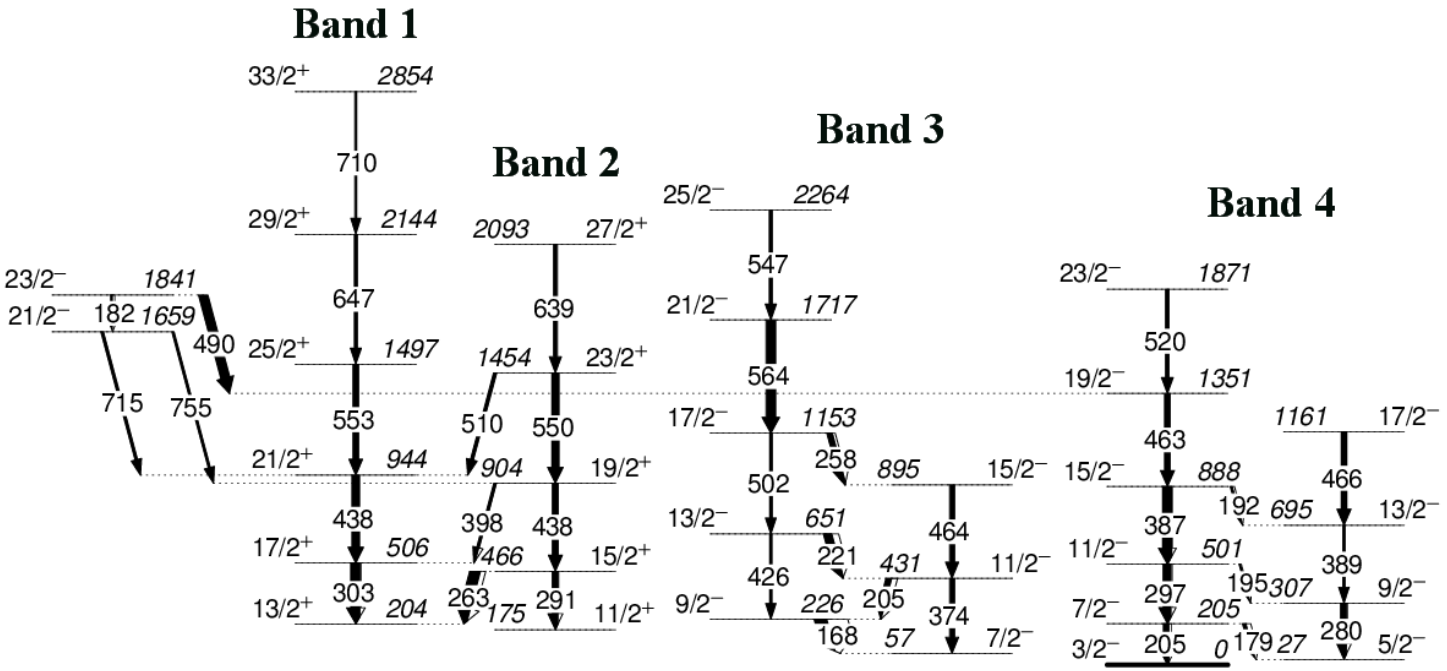

Figure 3.35: Level scheme of ^{187}Pt, constructed from our experimental data.

E_γ [keV]	I_γ [%]	E_i [keV]	α	I_i^π	I_f^π
Band 1					
302.67(8)	100(9)	506.2	1.02E-01	$17/2^+$	$13/2^+$
437.72(9)	75(10)	943.9	3.63E-02	$21/2^+$	$17/2^+$
553.5(1)	56(7)	1497.4	2.05E-02	$25/2^+$	$21/2^+$
646.7(2)	30(5)	2144.1	1.44E-02	$29/2^+$	$25/2^+$
709.6(3)	20(5)	2853.7	1.17E-02	$33/2^+$	$29/2^+$
Band 2					
262.8(2)	108(39)	466.3	4.99E-01	$15/2^+$	$13/2^+$
290.8(3)	63(6)	466.3	1.14E-01	$15/2^+$	$11/2^+$
397.8(2)	23(5)	904	1.61E-01	$19/2^+$	$17/2^+$
437.7(1)	61(12)	904	3.63E-02	$19/2^+$	$15/2^+$
510.1(3)	29(8)	1454.4	8.36E-02	$23/2^+$	$21/2^+$
550.5(1)	77(9)	1454.4	2.08E-02	$23/2^+$	$19/2^+$
638.6(2)	40(7)	2093	1.48E-02	$27/2^+$	$23/2^+$
Band 3					
168.5(2)	125(13)	225.7	1.70E+00	$9/2^-$	$7/2^-$
204.9(1)	59(18)	430.7	9.83E-01	$11/2^-$	$9/2^-$
220.6(1)	85(14)	651.3	8.03E-01	$13/2^-$	$11/2^-$
258.5(1)	55(8)	1153.1	5.16E-01	$17/2^-$	$15/2^-$
373.8(2)	50(19)	430.7	5.53E-02	$11/2^-$	$7/2^-$
425.8(7)	23(17)	651.3	3.91E-02	$13/2^-$	$9/2^-$
463.9(1)	50(18)	894.6	3.14E-02	$15/2^-$	$11/2^-$
502.0(3)	28(8)	26.Feb	2.59E-02	$17/2^-$	$13/2^-$
546.6(2)	33(6)	2263.5	2.11E-02	$25/2^-$	$21/2^-$
563.8(1)	98(11)	1716.9	1.96E-02	$21/2^-$	$17/2^-$
Band 4					
178.8(2)	34(12)	204.8	1.44E+00	$7/2^-$	$5/2^-$
192.2(2)	20(4)	888.2	1.17E+00	$15/2^-$	$13/2^-$
194.7(4)	10(4)	501.5	1.14E+00	$11/2^-$	$9/2^-$
204.8(1)	63(6)	204.8	3.53E-01	$7/2^-$	$3/2^-$
279.8(1)	63(6)	306.5	1.27E-01	$9/2^-$	$5/2^-$
296.72(9)	87(22)	501.5	1.08E-01	$11/2^-$	$7/2^-$

E_γ [keV]	I_γ [%]	E_i [keV]	α	I_i^π	I_f^π
Band 4	- continued				
386.81(8)	98(13)	888.2	5.04E-02	$15/2^-$	$11/2^-$
388.7(1)	26(9)	695.3	4.97E-01	$13/2^-$	$9/2^-$
463.0(1)	61(12)	1351.2	3.15E-02	$19/2^-$	$15/2^-$
465.5(1)	60(8)	1160.8	3.09E-02	$17/2^-$	$13/2^-$
519.7(2)	39(9)	1870.9	2.38E-02	$23/2^-$	$19/2^-$
Other					
182.162	18.23	1840.9	1.37E+00	$23/2^-$	$21/2^-$
489.738	92.09	1840.9	2.74E-02	$23/2^-$	$19/2^-$
715.038	26.09	1658.8	4.18E-03	$21/2^-$	$21/2^+$
754.523	22.70	1658.8	3.76E-03	$21/2^-$	$19/2^+$

Table 3.7: Gamma-ray transitions assigned to ^{187}Pt.

Another of the identified contaminants is ^{185}Ir. While ^{183}Ir is the decay product (with a probability of 0.003%) of ^{187}Au, it is not present in our data. ^{185}Ir is a product of the β^+ decay (99.99%) of ^{185}Pt. Whereas ^{185}Ir has a very strong presence in our data, ^{185}Pt transitions were not observed. Fig. 3.36 shows the level scheme of ^{185}Ir, which similarly to the previous contaminants was based on the existing level scheme from in-beam data [61]. Information on the individual transitions are listed in Tab. 3.8 (relative intensities I_γ are normalized with the 152.9 keV transition). The transitions in Band 1 of ^{185}Ir have the highest intensities for contaminants in our data besides ^{188}Au. This can be seen in Fig. 3.37, where the peak at 290.4 keV had to be cut to observe the lower intensity transitions. The band also contains a 413.0 keV transition, which has a similar energy than the 413.8 keV transition in ^{187}Au. The isotope also contains the identified (or assigned) transition with the highest energy, 1451.8 keV (see Fig. 3.37). Fig. 3.38 shows the LEPS spectrum gated at 152.9 keV, where characteristic X-rays of Iridium can be observed.

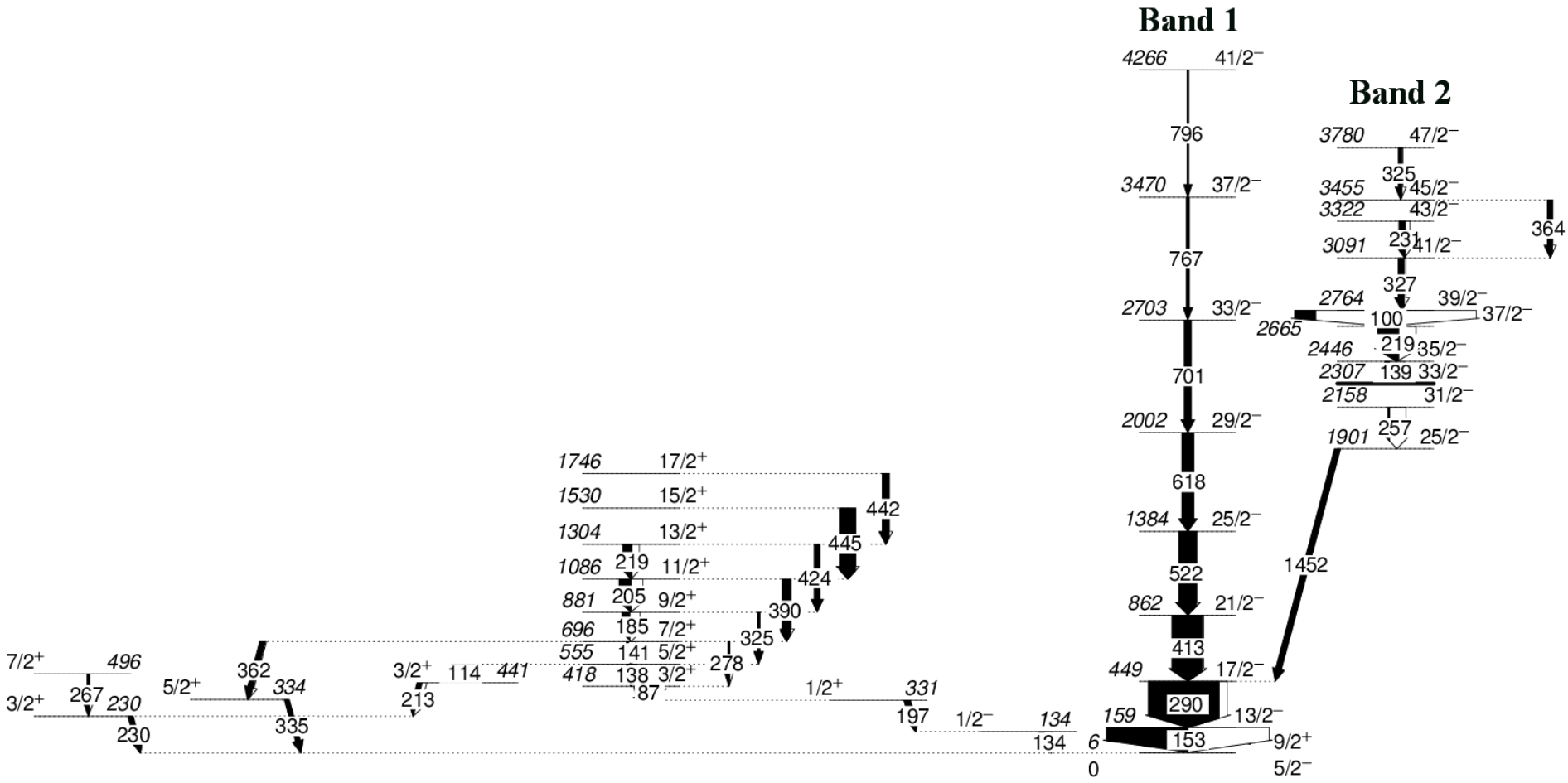

Figure 3.36: Level scheme of ^{185}Ir.

E_γ [keV]	I_γ [%]	E_i [keV]	α	I_i^π	I_f^π
Band 1					
152.91(4)	100(5)	158.7	9.93E-01	13/2-	9/2-
290.35(4)	87(4)	449.1	1.14E-01	17/2-	13/2-
412.98(6)	37(3)	862	4.22E-02	21/2-	17/2-
521.83(6)	22(2)	1383.9	2.36E-02	25/2-	21/2-
617.90(9)	15(2)	2001.8	1.59E-02	29/2-	25/2-
701.1(1)	9(1)	2702.9	1.20E-02	33/2-	29/2-
766.9(2)	3.6(9)	3469.7	9.95E-03	37/2-	33/2-
795.8(3)	2.2(8)	4265.5	9.21E-03	41/2-	37/2-
Band 2					
99.84(9)	26(3)	2764.5	7.60E+00	39/2-	37/2-
138.7(1)	5.9(6)	2445.9	2.97E+00	35/2-	33/2-
218.73(8)	26(5)	2664.6	8.24E-01	39/2-	37/2-
231.3(2)	8(1)	3322.4	7.04E-01	43/2-	41/2-
256.9(2)	2.5(5)	2157.7	8.12E+00	31/2-	25/2-
325.3(2)	4.5(8)	3780.2	2.75E-01	47/2-	45/2-
326.7(1)	8(2)	3091.1	2.74E-01	41/2-	39/2-
363.8(1)	7(1)	3454.9	5.95E-02	45/2-	41/2-
1451.8(1)	7.1(6)	1900.8	1.10E-02	25/2-	17/2-
Other					
86.8(4)	3(1)	417.8	1.17E+01	3/2+	1/2+
114.1(1)	4.4(7)	555.2	5.22E+00	5/2+	3/2+
133.9(2)	5.9(6)	134	1.57E+00	1/2-	5/2-
137.5(4)	2.9(5)	555.2	3.05E+00	5/2+	3/2+
141.0(2)	3.1(5)	696	2.84E+00	7/2+	5/2+
184.5(1)	10(1)	880.6	1.32E+00	9/2+	7/2+
196.9(1)	7(2)	330.9	7.50E-02	1/2+	1/2-
204.93(6)	15(1)	1085.6	9.77E-01	11/2+	9/2+
213(1)	6.1(8)	441.1	8.88E-01	3/2+	3/2+
218.76(8)	11(1)	1304.3	8.26E-01	13/2+	11/2+
229.66(7)	5.9(6)	229.7	5.16E-02	3/2+	5/2-
266.8(3)	3(1)	496.4	1.47E-01	7/2+	3/2+
277.9(2)	2.3(4)	696	1.30E-01	7/2+	3/2+
325.0(2)	3.5(7)	880.6	8.18E-02	9/2+	5/2+

E_γ [keV]	I_γ [%]	E_i [keV]	α	I_i^π	I_f^π
Other	- continued				
335(1)	5.9(6)	334.3	2.09E-02	5/2+	5/2-
361.79(9)	7(1)	696	2.08E-01	7/2+	5/2+
389.8(1)	11(1)	1085.6	4.92E-02	11/2+	7/2+
424.0(2)	7(1)	1304.3	3.95E-02	13/2+	9/2+
441.7(1)	9(1)	1745.8	3.57E-02	17/2+	13/2+
444.85(8)	20(2)	1530.3	3.49E-02	15/2+	11/2+

Table 3.8: Gamma-ray transitions assigned to ^{185}Ir.

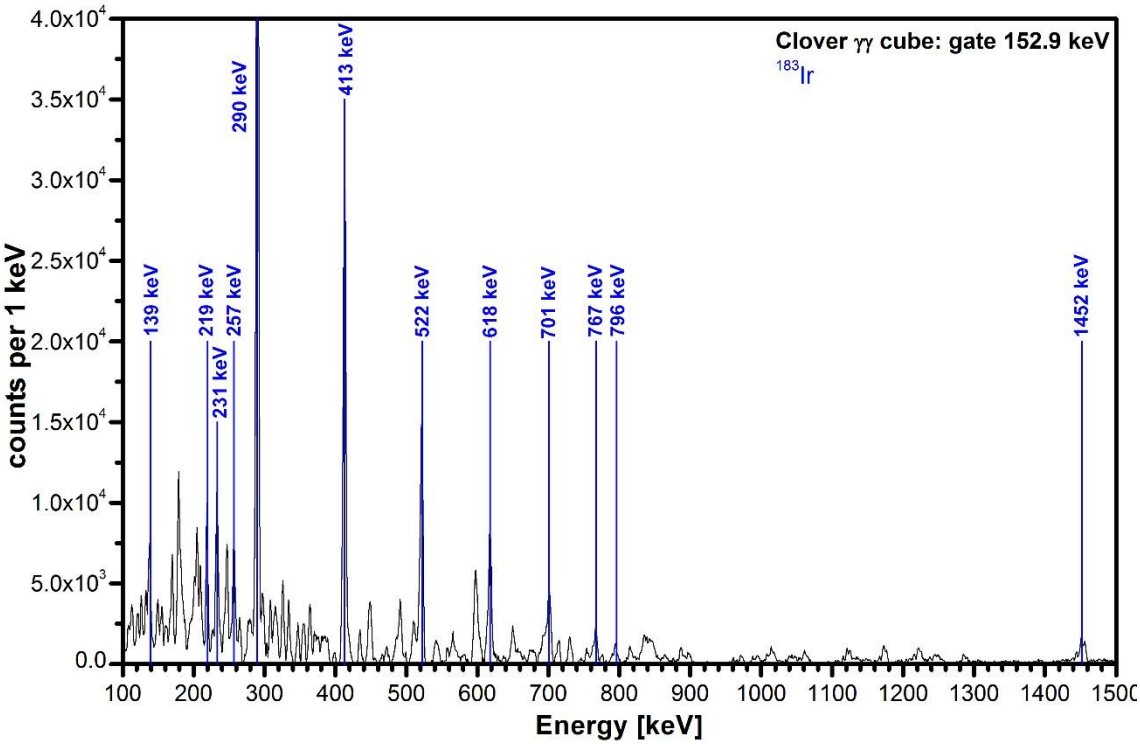

Figure 3.37: Energy spectrum gated at 152.9 keV.

In total, three major (^{188}Au, ^{185}Ir and $_{188}$Pt) and two minor (^{181}Ta and ^{187}Pt) contaminants have been observed in our data. We count the target element as a minor contaminant, since only few transitions are present. Fig. 3.39 shows the single spectrum of all the Clover detectors, where the most intensive peaks are labelled with different colours, representing the isotopes from which they originate. Transitions with similar energies are highlighted at one position. The colour of the line represents the isotope that has the most intensive transition in this case of conjoined labels. As we can see from this figure, the spectrum is very complicated, with many transitions from different isotopes having same energies.

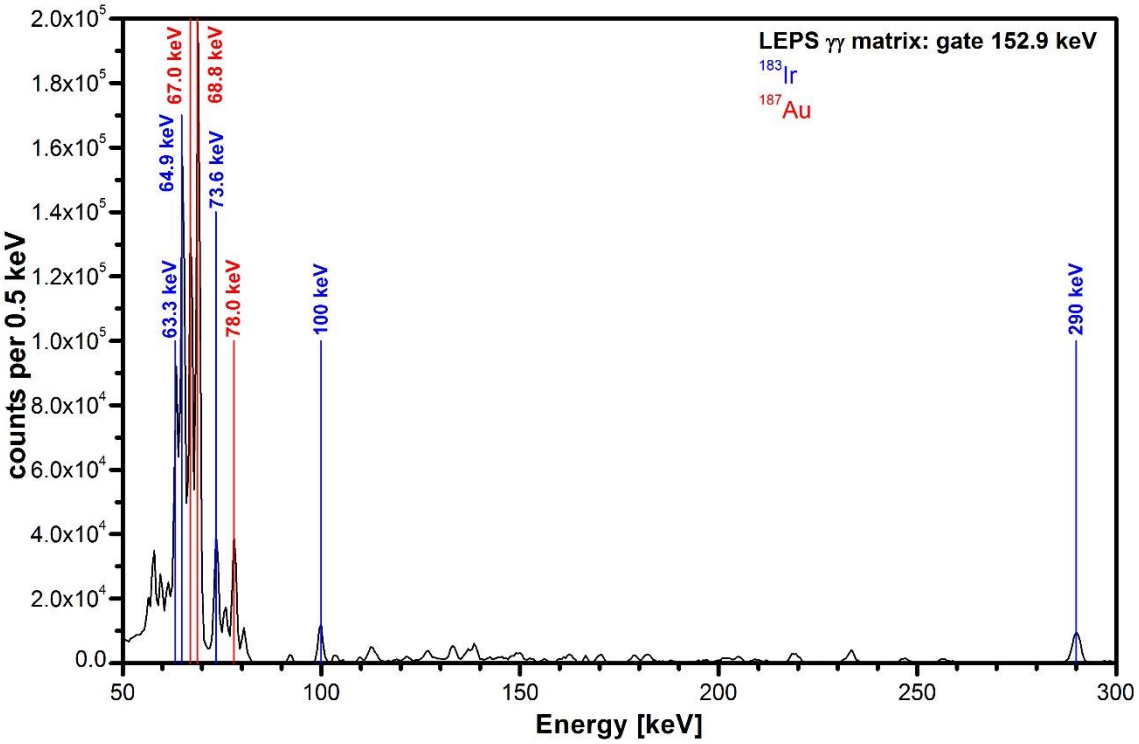

Figure 3.38: LEPS energy spectrum gated at 152.9 keV.

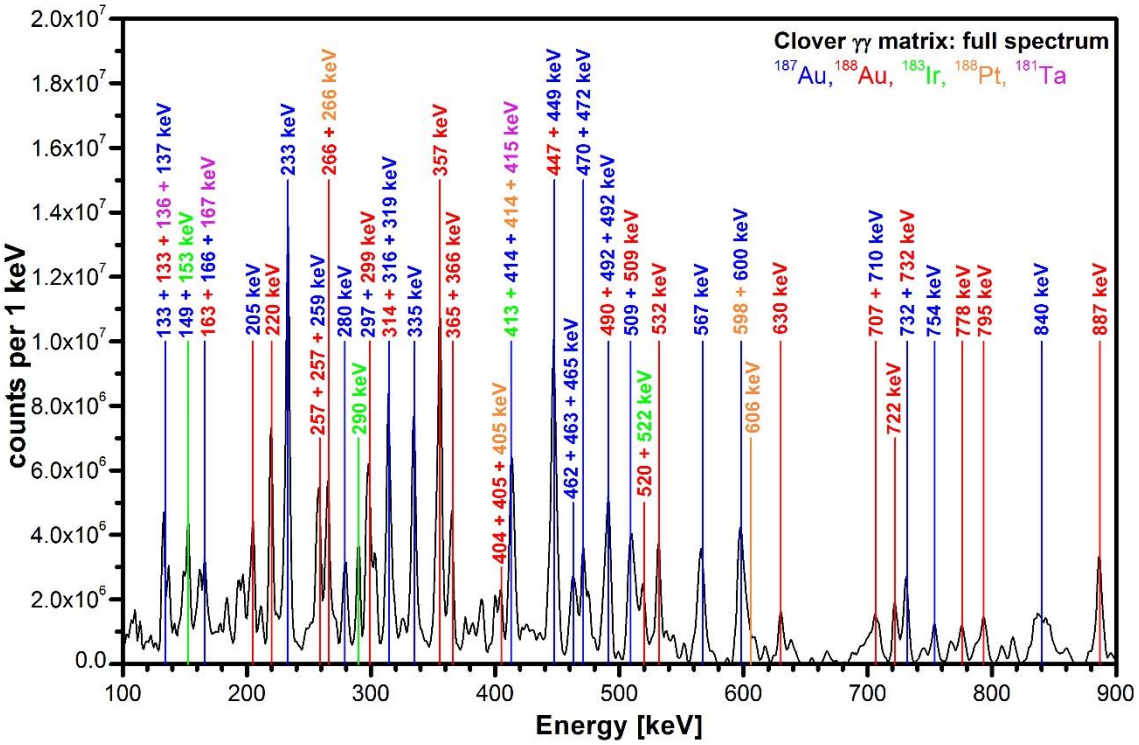

Figure 3.39: Full Clover spectrum of our experimental data.

3.3 New band and transitions in ^{187}Au

During the data analysis and the writing of the present work, a new publication about ^{187}Au came out [62]. In this article, new transitions and even a new band structure, which is supposedly from ^{187}Au, has been identified in the data from an in-beam gamma-ray spectroscopy experiment. ^{187}Au was produced at the Argonne National Laboratory in the reaction ^{19}F + ^{174}Yb, very similar to the one used in [7, 34]. The Gammasphere array was used to collect the data and only three and higher coincidences have been written. The data was analysed using RadWare. Fig. 3.40 shows the level scheme from the article, where new transitions are marked by an asterisk. Bands 1 and 2 (Yrast and LW) correspond to the same two bands in our data, band 3 (SP) is the new band.

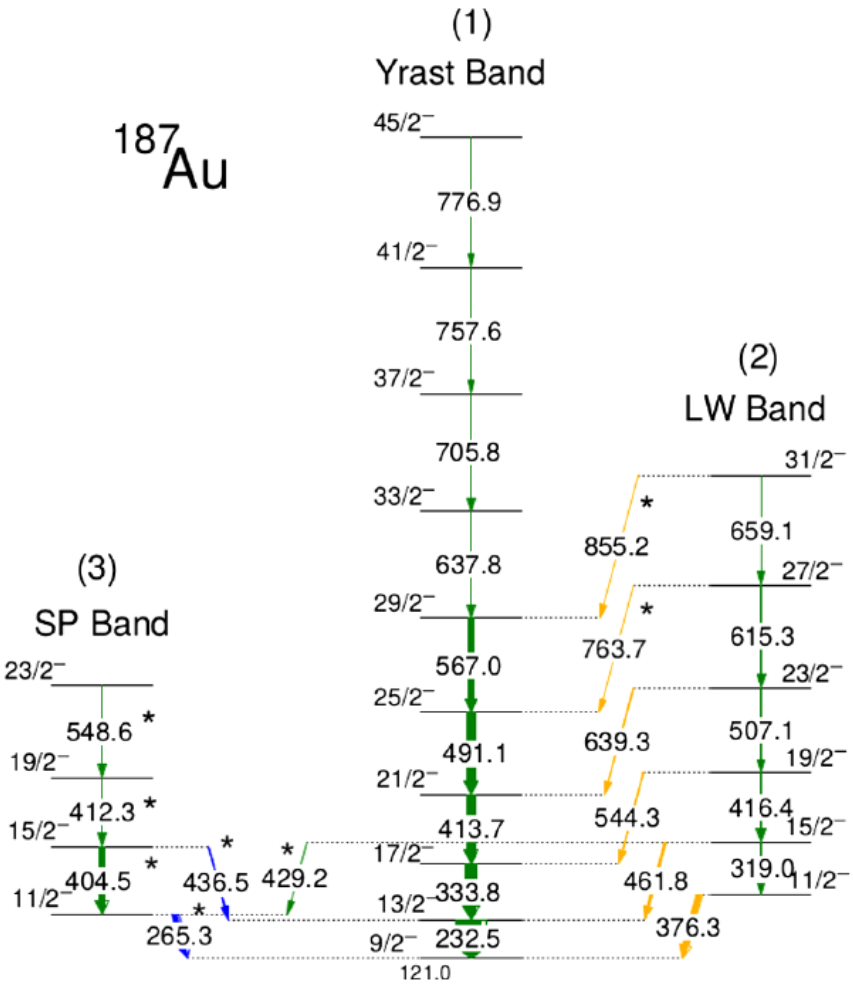

Figure 3.40: Partial level scheme of ^{187}Au, taken from [62].

None of these transitions have been observed in the previous in-beam data [6, 7]. The employed Gammasphere array has better efficiency than the previously used detecting systems and a very large amount of coincidence data was measured. This could explain the absence of the higher energy transitions, 763.7 keV and 855.2 keV, in the previous in-beam studies. The described article of interest does not contain any quantified intensity values of the transitions. As explained in chapter 3.1, the thickness of the arrow in a RadWare constructed level scheme depends on the intensity of the transition. Based on this, we can observe in Fig. 3.40, that the two new consecutive transitions, 265.3 keV and 404.5 keV, have intensities on the same level as the 567.0 keV transition. As a member of the main band, this transition has certainly high intensity, even in γ-γ-γ data. We would expect that transitions with the same level of intensity would by clearly visible in the data, even with lower detecting efficiency.

Similar transitions have been identified in the extensive beta-decay study of ^{187}Au [4], but they were assigned at different positions in the conclusive level scheme. Even more than with in-beam data, it seems strange that no trace of this band was observed. The newly observed band has a transition crossing to band 1, where it populates the $13/2^-$ state. This transition with an energy of 436.5 keV is therefore in coincidence with the 233 keV, the strongest transition in ^{187}Au. If present, this transition should have been visible in the data. The PTRM calculations performed for ^{187}Au do not predict an $11/2^-$ band-head at this energy. Fig. 3.41 shows the PTRM calculations, compared with the experimental data [4]. There are three $11/2^-$ states predicted in these calculations and all three were observed at energies similar to the expected energies from the model. Furthermore, the experimental data in [4] have very high sensitivity. Peaks with relative intensities as low as 0.3 % of the most intensive transition have been identified and placed in the level scheme. Therefore, we can presume that these new transitions are not present in the beta-decay study of ^{187}Au [4].

We looked at our data, if we can see these new transitions or some traces of them. Giving the nature of our data, with several contaminants present, it would be hard to confirm the existence of these transitions unless very clearly visible in all the possible coincidences. Like in the article, we used Clover γ-γ-γ data to investigate the presence of these transitions. When gating at new transitions, we used the exact energy as listed in Fig. 3.40, otherwise we used the energies from our data and level scheme, since there are small differences.

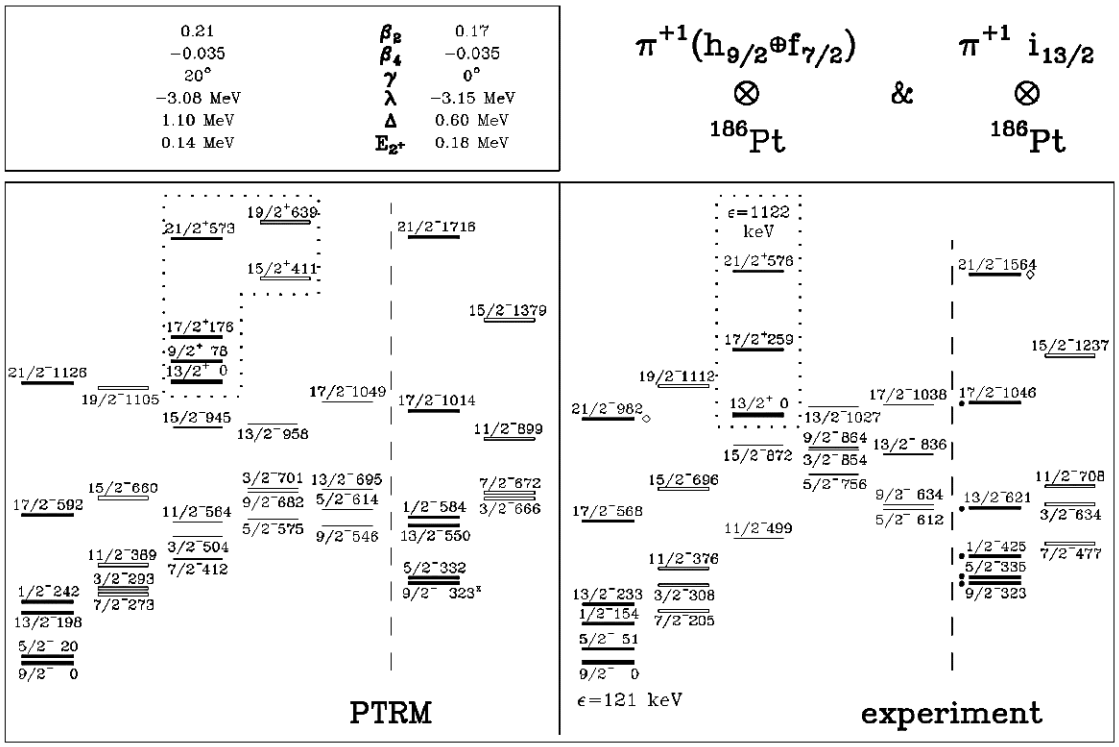

x the calculated band head energy is adjusted to the value of 323 keV

Figure 3.41: PTRM calculations and experimental data for ^{187}Au states, taken from [4].

Fig. 3.42 and 3.43 show spectra gated at *Band 1* transitions to observe the 763.7 keV and 855.2 keV transitions, respectively. The presence of these two transitions in our data can be ruled out, based on the shown spectra. As was the case in previous in-beam data, this can be attributed to the lower efficiency of the AFRODITE array compared to the Gammasphere array. The new 429.2 keV transition crosses from *Band 2* to the new band and should not be in coincidence with a *Band 1* transition. A spectrum gated at 506.8 keV and 416.8 keV, shown in Fig. 3.44, shows that this transition is also not present in our data. To observe the presence or absence of the 436.5 keV crossing transition, a spectrum gated at 233 keV and 412.3 keV is shown in Fig. 3.45. Once again, there is no evidence in our data to confirm this transition and the 548.6 keV transition. Ultimately, we tried to look at spectra gated solely at the newly observed transitions, Fig. 3.46 at 548.6 keV and 412.3 keV, and Fig. 3.47 at 404.5 keV and 265.3 keV. We see some of the new transitions in both cases, but this is the part where contaminations from our experiment interfere. Transitions similar to 404.5 keV and 265.3 keV are present in ^{188}Au, although not in coincidence with each other (see Fig. 3.25). Besides *Band* 1 in ^{187}Au, 413.0 keV is also a very strong transition in ^{185}Ir. However, the most significant contaminant in this case is ^{188}Pt. When we look at the

level scheme of ^{188}Pt (see Fig. 3.33 and Tab. 3.6), we see that the most intensive transitions in band 1 are 265.7 keV and 405.5 keV. This is clearly visible in Fig. 3.47, where other transitions from ^{188}Pt are highlighted. In fact, ^{188}Pt contains similar transitions to all of the transitions from the new band and they are even in coincidence.

New band in ^{187}Au: 265.3 - 404.5 - 412.3 - 548.6

Transitions in ^{188}Pt: 265.7 - 405.5 - (513.6) - (583.8) - 411.6 - (523.5) - 548.6

265.7 - 405.5 - 413.8 - 551.0

All the listed transitions from ^{188}Pt are shown in Fig. 3.47. Based on this, we cannot confirm the presence of the new band in our experimental data. Considering the fact, that no previous study of ^{187}Au has observed these new transitions, it is far more likely that they are not present in our data. Furthermore, it creates some scepticism as to whether the new transitions and band in [62] were assigned correctly or if they originate from ^{187}Au. Granting them the benefit of doubt, if these new transitions and band are indeed part of the ^{187}Au structure, it would be something that has not been observed previously. Not only in ^{187}Au, but in all of the studied odd-mass Au isotopes.

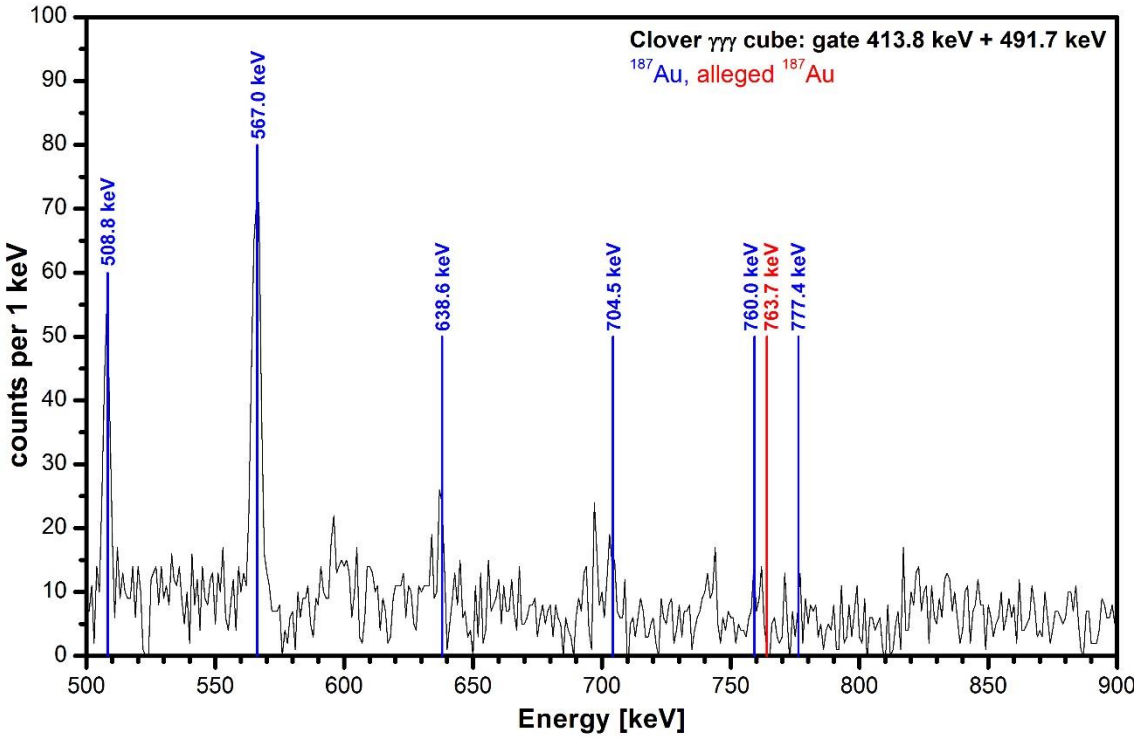

Figure 3.42: Energy spectrum gated at 413.8 keV and 491.7 keV.

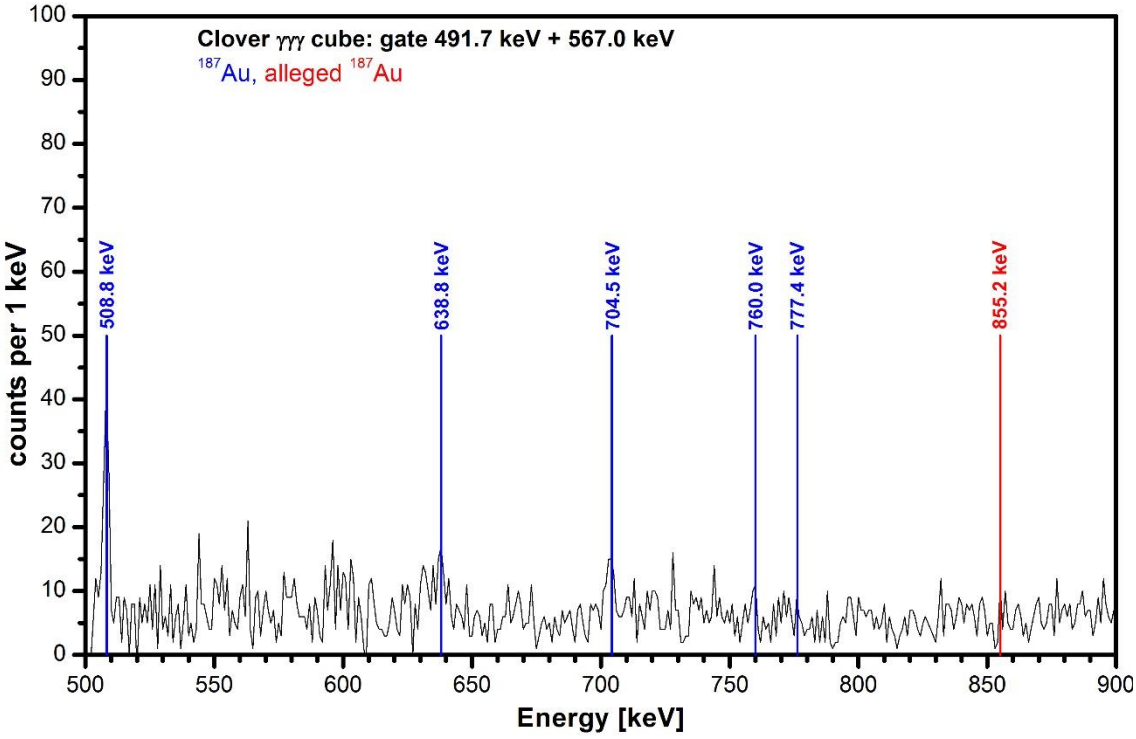

Figure 3.43: Energy spectrum gated at 491.7 keV and 567.0 keV.

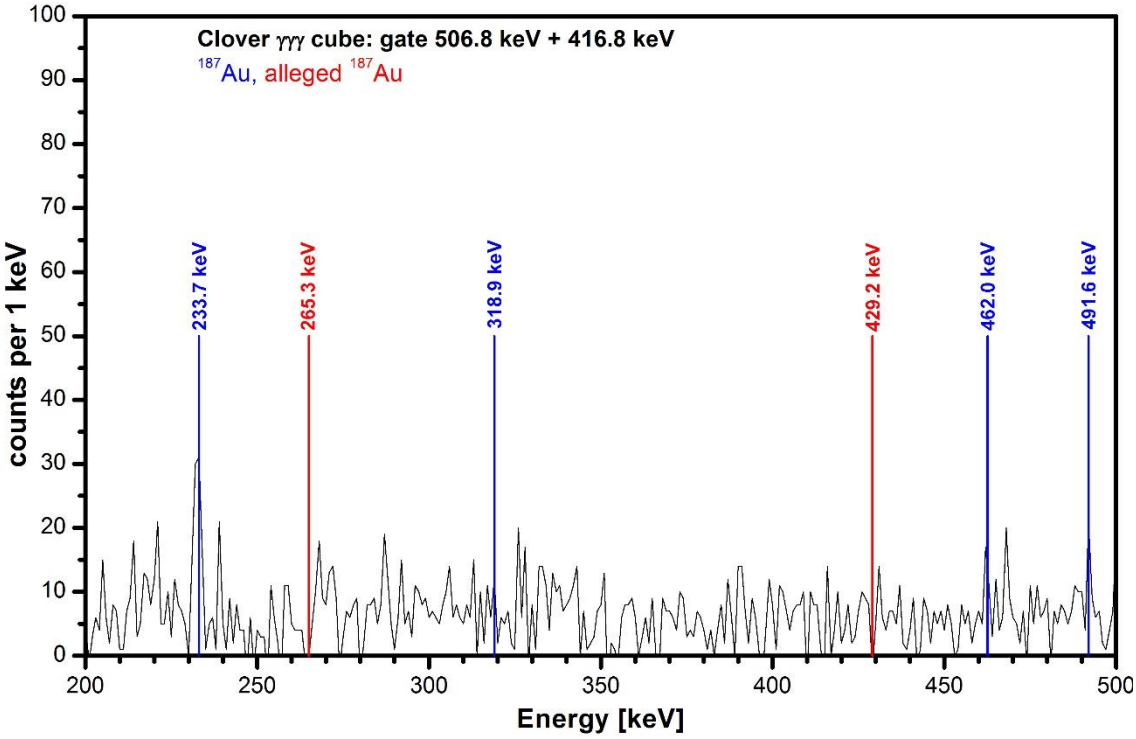

Figure 3.44: Energy spectrum gated at 506.8 keV and 416.8 keV.

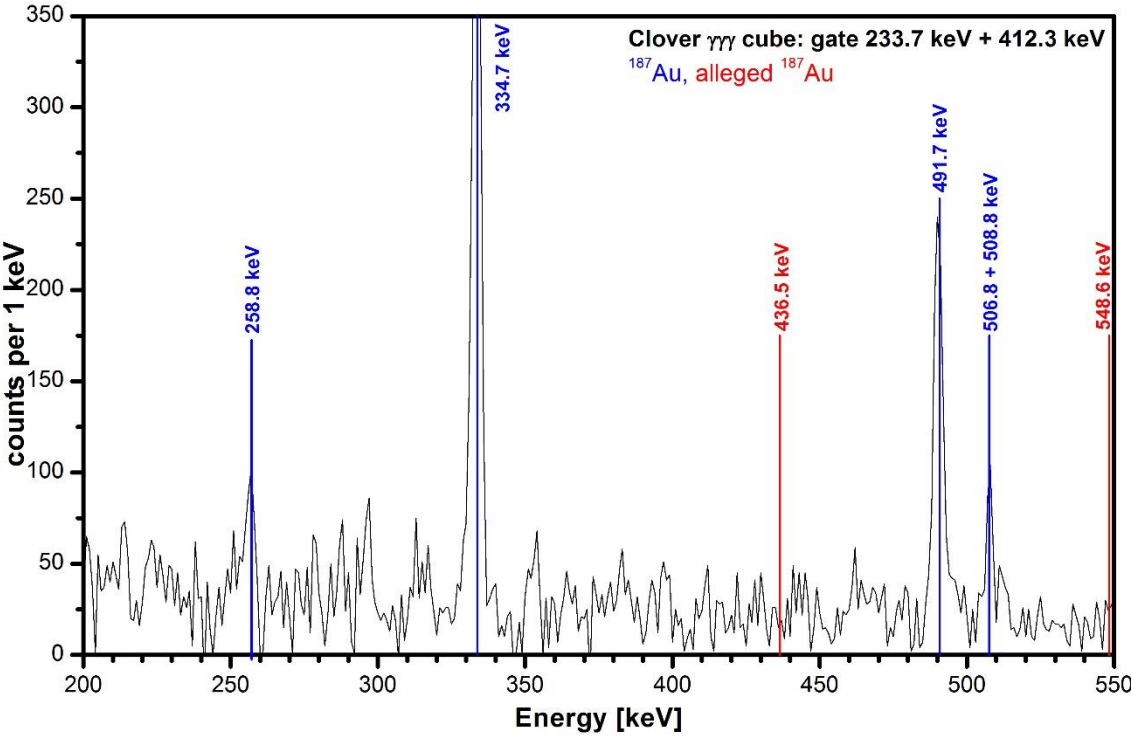

Figure 3.45: Energy spectrum gated at 233.7 keV and 412.3 keV

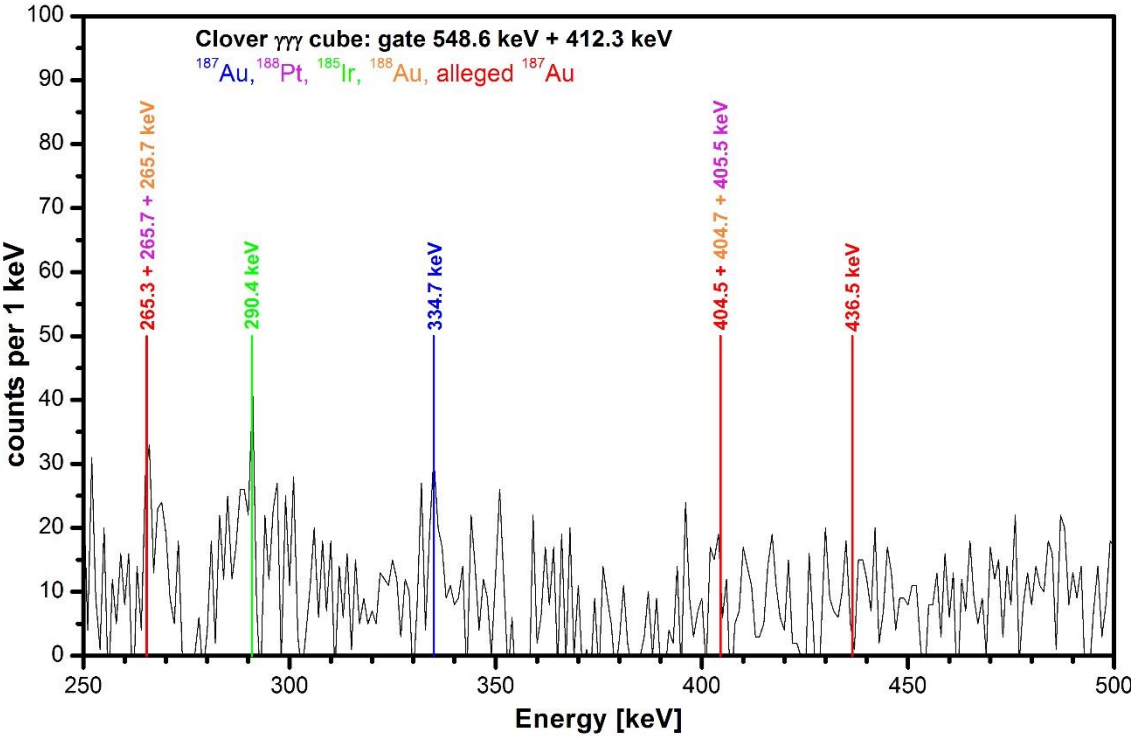

Figure 3.46: Energy spectrum gated at 548.6 keV and 412.3 keV.

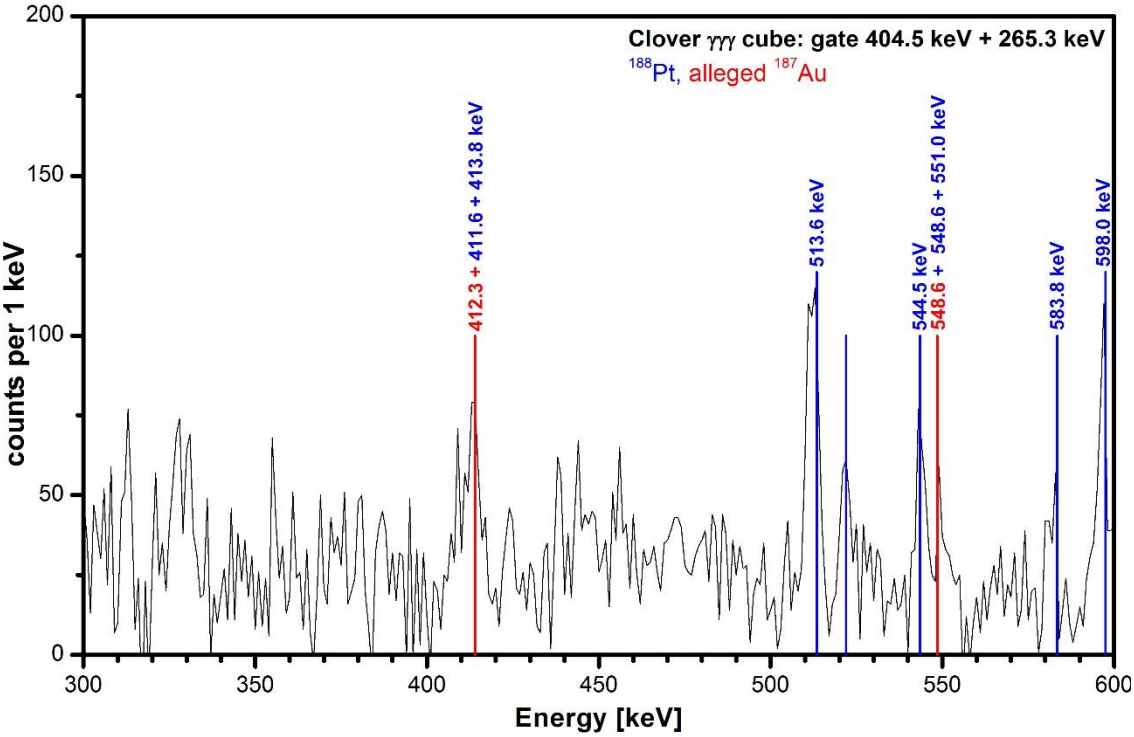

Figure 3.47: Energy spectrum gated at 404.5 keV and 265.3 keV.

Conclusion

Shape coexistence is a phenomenon in which nuclei of the same isotope exhibit different deformed and spherical shapes at low excitation energies. This coexistence occurs in many nuclei and it is possible that in principle every nucleus contains differently shaped excited states. Studying them can give us information on deformation, which as an underlying mechanism is still not understood. One of the regions where *shape coexistence* is abundantly found is in the vicinity of the Z = 82 proton closed shell and the N = 104 mid-shell point.

The present work contains results of a spectroscopic study of ^{187}Au. For this purpose, the experiment PR235 was performed to study the isotope with the in-beam gamma-ray spectroscopy method at the iThemba LABS facility. It is a complementary experiment to previous studies at the University of Jyväskylä and CERN-ISOLDE, conducted by our collaboration with the intention to systematically study the nuclear structure of odd mass Au isotopes. Nuclei of ^{187}Au were produced in a ^{181}Ta(^{12}C,6n)^{187}Au reaction. AFRODITE, an array consisting of HPGe Clover and LEPS detectors, was employed measurement of the gamma-rays in the target position. Offline data analysis was performed with a software, which was developed in C++, and in RadWare, where the subsequent level scheme of ^{187}Au was constructed. The aim was to expand on the existing level scheme and observe band structures that were predicted in PTRM calculations and from the systematics of the odd mass Au isotopes. During analysis, contaminations were observed in our data, which made it very difficult for us to recognize and assign new transitions to the studied ^{187}Au isotope. These contaminations originated from the fusion-evaporation reaction that produced ^{187}Au and were not identified and removed in the measurement, because they were supposed to be insignificant. Level schemes of contaminating isotopes were also constructed based on observed transitions in our data.

The constructed level scheme of ^{187}Au contains all the band structures observed in the two previously undertaken in-beam studies. We did not observe new band structures that were predicted on top of *intruder states* identified in beta-decay studies. Even with contaminations, we found no trace of new transitions and can declare that they are not present in our data. This, the main conclusion from our study, suggests that the structure in ^{187}Au differs from the one predicted by the systematics of odd mass Au

isotopes. The rotational bands must have a structure that requires a different a different type of experimental approach.

During the development of the present work, another study of ^{187}Au was published. This study claims to have observed new transitions and a new band structure that was not predicted nor seen in these types of isotopes before, although without a single spectrum as a proof. Our data analysis did not confirm the existence of these transitions. Furthermore, these new transitions are all part of ^{188}Pt, which is one of the contaminating isotopes in our data that was a by-product of the reaction. This isotope is unquestionably present in our data, identified by its characteristic X-rays. Therefore, we cannot disprove the existence of these transitions in 187Au, but there is some scepticism as to whether the new transitions and band were assigned correctly.

Záver

Tvarová koexistencia je fenomén, pri ktorom nadobúdajú jadrá jedného izotopu rôzne deformované a sférické tvary pri nízkych excitačných energiách. Koexistencia sa vyskytuje vo viacerých jadrách a je dosť možné že v princípe každé jadro obsahuje rôzne deformované stavy. Ich študovanie nám môže dodať informácie o deformácii, ktorá ako jeden zo zásadných procesov stále nie je úplne pochopená. Jedna z oblastí, kde sa *tvarová koexistencia* bežne vyskytuje, je v blízkosti Z = 82 uzavretej protónovej vrstvy a v blízkosti N = 104 mid-vrstvy.

Prezentovaná práca obsahuje výsledky spektroskpickej štúdie ^{187}Au. Za týmto účelom bol vykonaný experiment PR235, kde bol tento izotop študovaný metódou in-beam gama spektroskopie v zariadení iThemba LABS. Ide o doplňujúci experiment k predošlým štúdiám na Univerzite v Jyväskyle a v CERN-ISOLDE, vykonaných našou kolaboráciou so zámerom systematicky študovať jadrovú štruktúru nepárnych izotopov zlata. Jadrá ^{187}Au boli produkované v reakcii ^{181}Ta(^{12}C,6n)^{187}Au. AFRODITA, sféra pozostávajúca z HPGe Clover a LEPS detektorov, bolo použitá na meranie gama žiarenia v terčovej pozícii. Off-line analýza dát bola vykonaná pomocou softvéru, ktorý bol vyvinutý v C++, a pomocou balíčka RadWare, kde bola následne zostrojená rozpadová schéma ^{187}Au. Cieľom bolo rozšírenie známej rozpadovej schémy a spozorovať pásové štruktúry predpovedané v PTRM kalkuláciách a so systematiky nepárnych izotopov zlata. Počas analýzy bola zistená prítomnosť kontaminácii v našich dátach, ktoré značne sťažovali identifikáciu a priradenie nových prechodov k študovanému izotopu ^{187}Au. Tieto kontaminácie vznikli počas reakcie úplnej fúzie, ktorá produkovala ^{187}Au, pričom neboli v tomto procese identifikované a odstránené, pretože bol predpoklad, že budú bezvýznamné. Rozpadové schémy kontaminujúcich izotopov boli taktiež zostavené na základe prechodov pozorovaných v našich dátach.

Zostavená rozpadová schéma ^{187}Au obsahuje všetky pásové štruktúry pozorované v dvoch predošlých in-beam štúdiách. Intenzity a energie priradené k prechodom boli získané pomocou balíčka RadWare. Nepozorovali sme nové pásy, ktoré boli predpovedané nad *intruder stavmi* identifikovanými v beta rozpadových štúdiách. Aj s prítomnosťou kontaminácií sme nenašli žiadnu stopu nových prechodov a môžeme prehlásiť, že nie sú prítomné v našich dátach. Tento, hlavný záver z našej štúdie, naznačuje, že štruktúra ^{187}Au sa líši s tou, ktorá bola

predpokladaná na základe systematiky nepárnych izotopov zlata. Rotačné pásy musia mať štruktúru, ktorá vyžaduje inú experimentálnu metódu na jej pozorovanie.

Počas písania prezentovanej práce bola publikovaná nová štúdia ^{187}Au. Táto štúdia tvrdí, bez jediného spektra ako dôkazu, že boli pozorované nové prechody a nový pás, ktorý nebol nikdy predtým predpokladaný ani pozorovaný v týchto typoch experimentov. Analýza našich dát nepotvrdila existenciu týchto prechodov. Okrem toho, tieto nové prechody sú všetky súčasťou ^{188}Pt, ktorá je ako jedna z kontaminácii prítomná v našich dátach. Tento izotop je nesporne prítomný v našich dátach, identifikovaný pomocou jeho charakteristického röntgenového žiarenia. Z toho dôvodu nemôžeme vyvrátiť existenciu týchto prechodov v ^{187}Au, ale je tam istá pochybnosť, či boli tieto nové prechody a pás priradené správne.

Bibliography

[1] BOHR, A. and B. R. MOTTELSON, *Collective and Individual-particle aspects of Nuclear Structure*, In Mat. Fys. Medd. K. Dan. Vidensk. Selsk., **Vol. 27**, No. 16, p. 1-174 (1953).

[2] HEYDE, K. and J. L. WOOD, *Shape Coexistence in atomic nuclei*, In Rev. Mod. Phys., **Vol. 83**, Is. 4, p. 1467-1521 (2011). DOI: 10.1103/RevModPhys.83.1467.

[3] WOOD, J. L. *et al*., *Symmetry between particle and hole level systems in ^{189}Au*, In Phys. Rev. C, **Vol. 14**, Is. 2, p. 682-4 (1976). DOI: 10.1103/PhysRevC.14.682.

[4] RUPNIK, D. *et al*., *Levels of ^{187}Au: A detailed study of shape coexistence in an odd-mass nucleus*, In Phys. Rev. C, **Vol. 58**, Is. 2, p. 771-95 (1998). DOI: 10.1103/PhysRevC.58.771.

[5] PAPANICOLOPOULOS, C. D. *et al.*, *Very Converted Transitions and Particle-Core Coupling in Neutron-Deficient Odd-Mass Au Isotopes*, In Z. Phys. A, **Vol. 330**, Is. 4, p. 371-6 (1988). DOI: 10.1007/BF01290122.

[6] JOHANSSON, J. K. *et al.*, *Shape coexistence in ^{187}Au*, In Phys. Rev. C, **Vol. 40**, Is. 1, p. 132-44 (1989). DOI: 10.1103/physrevc.40.132.

[7] BOURGEOIS, C. *et al*, *Shape coexistence at high spin in ^{187}Au*, In Z. Phys. A, **Vol. 333**, Is. 1, p. 5-14 (1989). DOI: 10.1007/BF01290104.

[8] RADFORD, D. C., *ESCL8R and LEVIT8R: Software for interactive graphical analysis of HPGe coincidence data sets*, In Nucl. Instr. and Meth. A, **Vol. 361**, Is. 1-2, p. 297-306 (1995). DOI: 10.1016/0168-9002(95)00183-2.

[9] RADFORD, D. C., *Background subtraction from in-beam HPGe coincidence data sets*, In Nucl. Instr. and Meth. A, **Vol. 361**, Is. 1-2, p. 306-16 (1995). DOI: 10.1016/0168-9002(95)00184-0.

[10] HEYDE K., *Basic Ideas and Concepts in Nuclear Physics, 3rd Edition*, Institute of Physics, London (2004). ISBN 0-7503-0980-6.

[11] FEWELL, M. P., *The atomic nuclide with the highest mean binding energy*, In Am. J. Phys., **Vol. 63**, No. 7, p. 653-8 (1995). DOI: 10.1119/1.17828.

[12] WEIZSÄCKER, C. F. v., *Zur Theorie der Kernmassen*, In Zeit. für Phys., **Vol. 96**, Is. 7-8, p. 431-58 (1935). DOI: 10.1007/BF01337700.

[13] KRANE, K. S., *Introductory Nuclear Physics, 3rd Edition*, Oregon State University (1987). ISBN 978-0-471-80553-3.

[14] MAYER, M. G., *On Closed Shells in Nuclei. II*, In Phys. Rev., **Vol. 75**, Is. 12, p. 1969-70 (1949). DOI: 10.1103/PhysRev.75.1969.

[15] HAXEL, O. and J. HANS D. JENSEN and HANS E. SUESS, *On the "Magic Numbers" in Nuclear Structure*, In Phys. Rev. **Vol. 75**, Is. 11, p. 1766(1) (1949). DOI: 10.1103/PhysRev.75.1766.2.

[16] NILSSON, S. G., *Binding States of Individual Nucleons in Strongly Deformed Nuclei*, In Mat. Fys. Medd. K. Dan. Vidensk. Selsk., **Vol. 29**, No. 16, p. 1-69 (1955).

[17] THUMMERER, S. *et al.*, *The Population of Deformed Bands in ^{48}Cr by emission of ^{8}Be from the ^{32}S + ^{24}Mg reaction*, In J Phys. G: Nucl. Part. Phys., **Vol. 27**, No. 7, p. 1405-20 (2001).

[18] VENHART, M., *Gamma-spectroscopy of K-isomers and Non-yrast States in ^{254}No - Influence of Deformed Shell Gaps Z = 100 and N = 152*, PhD thesis, Comenius University in Bratislava (2008).

[19] https://www.technologyuk.net/mathematics/geometry/ellipsoids.shtml, accessed on April 2018.

[20] HEISS, W. D. and R. A. LYNCH and R. G. NAZMITDINOV, *Nonaxial octupole deformations and shell phenomena*, In Phys. Rev. C, **Vol. 60**, Is. 3, p. 034303(8) (1999). DOI: 10.1103/PhysRevC.60.034303.

[21] LARSSON, S. E. and LEANDER, G. and RAGNARSSON, I., *Nuclear core-quasiparticle coupling*, In Nucl. Phys. A, **Vol. 307**, Is. 2, p. 189-223 (1978). DOI: 10.1016/0375-9474(78)90613-9.

[22] MORINAGA, H., *Interpretation of Some of the Excited States of 4n Self-Conjugate Nuclei*, In Phys. Rev., **Vol. 101**, Is. 1, p. 254-58 (1956). DOI: 10.1103/PhysRev.101.254.

[23] FOSSION, R. *et al., Intruder bands and configuration mixing in lead isotopes*, In Phys. Rev. C, **Vol. 67**, Is. 2, p. 024306(7) (2003). DOI: 10.1103/PhysRevC.67.024306.

[24] VENHART, M. *et al., New systematic features in the neutron-deficient Au isotopes*, In J Phys. G: Nucl. Part. Phys., **Vol. 44**, No. 7, p. 074003(20) (2017). DOI: 10.1088/1361-6471/aa7297.

[25] XU, Y. *et al., Shape coexistence and electric monopole transitions in ^{184}Pt*, In Phys Rev. Lett. **Vol. 68**, Is. 26, p. 3853-56 (1992). DOI: 10.1103/PhysRevLett.68.3853.

[26] WOOD, J. L. *et al., Electric monopole transitions from low energy excitations in nuclei*, In Nuc. Phys. A, **Vol. 651**, Is. 4, p. 323-68 (1999). DOI: 10.1016/S0375-9474(99)00143-8.

[27] SCHIECK, H. P. gen., *Nuclear Reactions: An Introduction*, Institut für Kernphysik, University of Cologne (2014). ISBN 978-3-624-53985-5.

[28] PAUL, E. S. *et al., In-beam γ-ray spectroscopy above ^{100}Sn using the new technique of recoil decay tagging*, In Phys. Rev. C, **Vol. 51**, Is. 1, p. 77-87 (1995). DOI: 10.1103/physrevc.51.78.

[29] NEWTON, J. O. *et al., Angular distributions of gamma rays produced in reactions with heavy ions*, In Nucl. Phys. A, **Vol. 95**, Is. 2, p. 357-76 (1967). DOI: 10.1016/0375-9474(67)90507-6.

[30] KRANE, K. S. and STEFFEN, R. M. and WHEELER, R. M., *Directional correlations of gamma radiations emitted from nuclear states oriented by nuclear reactions or cryogenic methods*, In Atomic Data and Nuclear Data Tables, **Vol. 11**, Is. 5, p. 351-406 (1973). DOI: 10.1016/S0092-640X(73)80016-6.

[31] KRÄMER-FLECKEN, A. *et al., Use of DCO ratios for spin determination in γ-γ coincidence measurements*, In Nucl. Instr. and Meth. A, **Vol. 275**, Is. 2, p. 333-9 (1989). DOI: 10.1016/0168-9002(89)90706-7.

[32] FAGG, L. W. and S. S. HANNA, *Polarization Measurements on Nuclear Gamma Rays*, In Rev. Mod. Phys., **Vol. 31**, Is. 3, p. 711-58 (1959). DOI: 10.1103/RevModPhys.31.711.

[33] SCHMID, G. J. *et al.*, *Gamma-ray polarization sensitivity of the Gammasphere segmented germanium detectors*, In Nucl. Instr. and Meth. A, **Vol. 417**, Is. 1, p. 95-110 (1998). DOI: 10.1016/S0168-9002(98)00624-X.

[34] LEE, J. H. *et al.*, *Linear polarization measurements of gamma rays in 155Gd by using a segmented Compton polarimeter*, In J. Kor. Phys. Soc., **Vol. 40**, Is. 5, p. 793-801 (2002).

[35] YAMAZAKI, T., *Tables of coefficients for angular distribution of gamma rays from aligned nuclei*, In Nucl. Data Sheets. Sec. A, **Vol. 3**, Is. 1, p. 1-23 (1967). DOI: 10.1016/S0550-306X(67)80002-8.

[36] CONRADIE, J. L. *et al.*, *Cyclotrons at iThemba LABS*, In 17th International Conference on Cyclotrons and Their Applications, Tokyo, Japan, 18 - 22 Oct 2004, p. 105 (2004).

[37] KHESWA N. Y. and E. Z. BUTHELEZI and J. J. LAWRIE, *Making of targets for physics experiments at iThemba LABS*, In Nucl. Instr. and Meth. Phys. Res. A, **Vol. 590**, Is. 1, p. 114-7 (2008). DOI: 10.1016/j.nima.2008.02.066.

[38] RAMASHIDZHA, T. M., *Gamma spectroscopy of the doubly-odd ^{194}Tl nucleus*, Master thesis, University of Western Cape (2006).

[39] http://healthdocbox.com/Brain_Tumor/73154319-Review-of-neutron-and-proton-therapy.html. Accessed on February 2018.

[40] LIPOGLAVŠEK, M. *et al.*, *Measuring high-energy γ-rays with Ge Clover detectors*, In Nucl. Instr. and Meth. Phys. Res. A, **Vol. 557**, Is. 2, p. 523-27 (2006). DOI: 10.1016/j.nima.2005.11.067.

[41] http://tlabs.ac.za/?page_id=218, accessed on January 2015.

[42] JONES, P. M *et al.*, *Calibration of the new composite "Clover" detector as a Compton polarimeter for the EUROGAM array*, In Nucl. Instr. and Meth. Phys. Res. A, **Vol. 362**, Is 2-3, p. 556-60 (1995). DOI: 10.1016/0168-9002(95)00246-4.

[43] JOSHI, P. K. *et al.*, *Study of the characteristics of a Clover detector*, In Nucl. Instr. and Meth. Phys. Res. A, **Vol. 399**, Is. 1, p. 51-6 (1997). DOI: 10.1016/S0168-9002(97)00871-1.

[44] DUCHÊNE, G. *et al.*, *The Clover: a new generation of composite Ge detectors*, In Nucl. Instr. and Meth. Phys. Res. A, **Vol. 432**, Is. 1, p. 90-110 (1999). DOI: 10.1016/S0168-9002(99)00277-6.

[45] *GLP series planar HPGe low-energy detector product configuration guide, https://www.ortec-online.com/-/media/ametekortec/brochures/glp.pdf?la=en* Accessed on January 2015.

[46] REISDORF, W., *Analysis of Fissionability Data at High Excitation Energies*, In Z. Phys. A, **Vol. 300**, Is. 2-3, p. 227-38 (1981). DOI: 10.1007/BF01412298.

[47] http://www.xia.com/DGF_Pixie-16.html, accessed on March 2018.

[48] PALIT, R. *et al.*, *A high speed digital data acquisition system for the Indian National Gamma Ray at Tata Institute of Fundamental Research*, In Nucl. Instr. and Meth. A, **Vol. 680**, p. 90-6 (2012). DOI: 10.1016/j.nima.2012.03.046.

[49] *Multi Instance Data Acquisition System*, http://npg.dl.ac.uk/MIDAS/, accessed on April 2018.

[50] http://ns.ph.liv.ac.uk/MTsort-manual/eventformat.html, accessed on February 2016.

[51] BRUN, R. and RADEMAKERS, F., *ROOT – An object orientated data analysis framework*, In Nucl. Instr. and Meth. A, **Vol. 389**, Is. 1-2, p. 81-6 (1997). DOI: 10.1016/S0168-9002(97)00048-X.

[52] ZIEGLER, J. F. and J. BIERSACK and U. LITTMARK, *The Stopping and Range of Ions in Matter*, Pergamon (1985). ISBN 9780080216034.

[53] ZIEGLER, J. F. and M. D. ZIEGLER and J. P. BIERSACK, *The Stopping and Range of Ions in Matter*, In Nucl. Instr. and Meth. B, **Vol. 268**, Is. 11-12, p. 1818-23 (2010). DOI: 10.1016/j.nimb.2010.02.091.

[54] EKSTRÖM, C. *et al.*, *Nuclear spins of* $^{186, 187, 188, 189, 189m}$ *Au*, In Phys. Lett. B, **Vol. 60**, Is. 2, p. 146-48 (1976). DOI: 10.1016/0370-2693(76)90409-3.

[56] BRAGA, R. A. *et al.*, *Half-life of the* $h_{9/2}$ *shell-model intruder-state isomer* ^{187m}*Au*, In Nucl. Phys. A, **Vol. 410**, Is. 3, p. 441-44 (1983).

[57] WALLMEROTH, K. *et al*., *Sudden Change in the Nuclear Charge Distribution of Very Light Gold Isotopes*, In Phys Rev. Lett. **Vol. 58**, Is. 15, p. 1516-19 (1987). DOI: 10.1103/PhysRevLett.58.1516.

[58] BERG, V. *et al., Transition rates between negative-parity states in odd-mass gold nuclei*, In Nucl. Phys. A, **Vol. 410**, Is. 3, p. 445-47 (1983). DOI: 10.1016/0375-9474(83)90637-1.

[59] VENHART, M. *et al., De-excitation of the strongly coupled band in ^{177}Au and implications for core intruder configurations in the light Hg isotopes*, In Phys. Rev. C, **Vol. 95**, Is. 6, p. 061302 – 1-5 (2017). DOI: 10.1103/PhysRevC. 95.061302.

[60] JANZEN, V. P. *et al., Prolate and oblate band structures in odd-odd 186,188Au*, In Phys. Rev. C, **Vol. 45**, Is. 2, p. 613-39 (1992). DOI: 10.1103/physrevc.45.613.

[61] ANDRÉ, S. *et al., Levels of ^{185}Ir excited in the (α, x n) reactions*, In Nucl. Phys. A, **Vol. 325**, Is. 2-3, p. 445-62 (1979). DOI: 10.1016/0375-9474(79)90026-5.

[62] SENSHARMA, N. *et al., Longit udinal Wobbling Motion in 187Au*, In Phys. Rev. Lett., **Vol. 124**, Is. 5, p. 052501 – 1-6 (2020). DOI: 10.1103/PhysRevLett. 124.052501.

Appendix A – Publications

Venhart, M., Wood, J. L., Sedlák, M., Balogh, M, Bírová, M., Boston, A. J., Cocolios, T. E., Harkness-Brennan, L. J., Herzberg, R.-D., Holub, L., Joss, D. T., Judson, D. S., Kliman, J., Klimo, J., Krupa, L., Lušnák, J., Makhathini, L., Matoušek, V., Motyčák, Š., Page, R.D., Patel, A., Petrík, K., Podshibyakin, A.V., Prajapati, P.M., Rodin, A.M., Špaček, A., Urban, R., Veselský, M. *New systematic features in the neutron-deficient Au isotopes*. Journal of Physics G: Nuclear and Particle Physics **44**, 074003 (2017).

Gillespie, S.A., Andreyev, A.N., Al Monthery, M., Barton, CH.J., Antalic, S., Auranen, K., Bardan, H., Cox, D.M., Cubiss, J.G., O'Donnell, D., Grahn, T., Greenlees, P.T., Herzáň, A., Higgins, E., Julin, R., Asztalos, S., Klimo, J., Konki, J., Leino, M., Mallaburn, M., Pakarinen, J., Papadakis, P., Partanen, J., Prajapati, P.M., Rahkila, P., Sandzelius, M., Scholey, C., Sorri, J., Stolze, S., Urban, R., Uusitalo, J., Venhart, M., Weaving, F. *Identification of a 6.6 microsecond isomeric state in ^{175}Ir*. Physical Review C - Nuclear Physics **99**, 064310 (2019).

Venhart, M., Balogh, M., Herzáň, A, Wood, J.L., Ali, F.A., Joss, D.T., Andreyev, A.N., Auranen, K., Carroll, R.J., Drummond, M.C., Easton, J.L., Greenlees, P.T., Grahn, T., Gredley, A., Henderson, J., Jakobsson, U., Julin, R., Asztalos, S., Konki, J., Lawrie, E., Leino, M., Matoušek, V., McPeake, CH.J., O'Donnell, D., Page, R.D., Pakarinen, J., Papadakis, P., Partanen, J., Peura, P., Rahkila, P., Ruotsalainen, P., Sandzelius, M. Sarén, J., Saygi, B., Sedlák, M., Scholey, C., Sorri, J., Stolze, S., Thornthwaite, A., Urban, R., Uusitalo, J., Veselský, M, Weaving, F. *Population of a low-spin positive-parity band from high-spin intruder states in ^{177}Au: The two-state mixing effect*. Physics Letters B **806**, 135488 (2020).